

**TREATING TRIPLE-NEGATIVE BREAST CANCER  
THROUGH NANOPARTICLE-MEDIATED  
PHOTOTHERMAL THERAPY AND GENE REGULATION**

by

Danielle M. Valcourt

A dissertation submitted to the Faculty of the University of Delaware in partial fulfillment of the requirements for the degree of Doctor of Philosophy in Biomedical Engineering

Spring 2020

© 2020 Danielle M. Valcourt  
All Rights Reserved

**TREATING TRIPLE-NEGATIVE BREAST CANCER  
THROUGH NANOPARTICLE-MEDIATED  
PHOTOTHERMAL THERAPY AND GENE REGULATION**

by

Danielle M. Valcourt

Approved: \_\_\_\_\_  
Dawn Elliott, Ph.D.  
Chair of the Department of Biomedical Engineering

Approved: \_\_\_\_\_  
Levi Thompson, Ph.D.  
Dean of the College of Engineering

Approved: \_\_\_\_\_  
Douglas J. Doren, Ph.D.  
Interim Vice Provost for Graduate and Professional Education and  
Dean of the Graduate College

I certify that I have read this dissertation and that in my opinion it meets the academic and professional standard required by the University as a dissertation for the degree of Doctor of Philosophy.

Signed:

---

Emily Day, Ph.D.  
Professor in charge of dissertation

I certify that I have read this dissertation and that in my opinion it meets the academic and professional standard required by the University as a dissertation for the degree of Doctor of Philosophy.

Signed:

---

Millicent Sullivan, Ph.D.  
Member of dissertation committee

I certify that I have read this dissertation and that in my opinion it meets the academic and professional standard required by the University as a dissertation for the degree of Doctor of Philosophy.

Signed:

---

Thomas Epps, III, Ph.D.  
Member of dissertation committee

I certify that I have read this dissertation and that in my opinion it meets the academic and professional standard required by the University as a dissertation for the degree of Doctor of Philosophy.

Signed:

---

John Slater, Ph.D.  
Member of dissertation committee

I certify that I have read this dissertation and that in my opinion it meets the academic and professional standard required by the University as a dissertation for the degree of Doctor of Philosophy.

Signed:

---

Jason Gleghorn, Ph.D.

Member of dissertation committee

## ACKNOWLEDGMENTS

First and foremost, thank you to my advisor, Dr. Emily Day. You have been the best mentor I could have asked for over the last four and a half years. I am lucky to have had your guidance, support, advice, and friendship; I would not be the same scientist I am today without you. Further, thanks to my committee members, Dr. Millicent Sullivan, Dr. Thomas Epps, III, Dr. John Slater, and Dr. Jason Gleghorn, for your support and insights throughout my PhD experience.

Next, thank you to the Day Lab members, both past and present, for making my time inside and outside of lab so enjoyable: Ritu Goyal, Chintan Kapadia, Jianxin Wang, Rachel Riley, Jilian Melamed, Jenna Harris, Megan Dang, Benjamin Luo, Mackenzie Scully, N'Dea Irvin-Choy, Elise Hoover, and Max Marek. You have all been wonderful to work with and I have grown as a researcher and a mentor from working with every one of you.

I would like to acknowledge several individuals for their help with equipment and experiments throughout my PhD. First, thank you to the Bioimaging Center at the Delaware Biotechnology Institute, especially Shannon Modla, for your extensive help with microscopy. Second, I am extremely grateful to Dr. Gwen Talham, Travis Cossette, and the rest of the staff at the animal facility for training me and assisting in all of my animal studies over the past few years.

Thanks to my UD BME friends, who have been an incredible support system throughout this process. To my cohort, whose friendships made the transition to graduate school infinitely easier: Rachel Hutzell, Ryan McDonough, Jasmine Shirazi,

Aditya Jagaparu, Wade Stewart, Nick Trompeter, and Saurabh Modi. Thank you to Peyton Delgorio for giving me an extra excuse to get Dunks and for making sure I always have brunch in my life. To Jamie Benson, for being my extra special convert to Bruins fandom. Thanks to Keely Keller for being a wonderful roommate and even better friend. To Margot Farnham for always being ready with wine and Criminal Minds and for being the best birthday twin. And special thanks to Kyle Meadows for seeing me through the good, the bad, and the ugly; I couldn't have done it without you.

Next, I'd like to thank my friends outside of BME for broadening my horizons and giving me an escape from grad school. To my friends in other UD departments, I am lucky to have had you as part of my PhD experience: Eric, Sam, Olivia, Bo, Sarah, Nicole, Alex, and Abhishek. Thank you to Olivia Valcarce and Janine Kopeski, who have been the best hometown friends a girl could ask for. To my Philly girls for all of your support: Sarah, Val, Nicole S, Kayla, Audrey, Nicole R, Alex, Katie, Megan, and Torey. Thanks to my Notre Dame family for never failing to put a smile on my face: Kat, Maggie, Nick, Matt, Michael, Jess, Kaleigh, and Maddie. And finally, to my soccer teams for the best stress relief possible (and for a few medals): Haley, Neal, Chris, Davey, Eric, Matt, Scott, Dakota, Kevin, Frank, Jess, Criztal, Luis, Bola, Brendan, Diego, and Joe.

Extra special thanks to my family for their unending love and support. Thanks to Greg and Paula for living within a reasonable driving distance and making me your stand-in daughter. To my extended family for surrounding me with love and joy every time I come home: Mimi, Poppa, Memere, Jon, Brad, Heidi, Nadine, John, Jessica, Melissa, Jesse, Kevin, and Kristin. And to Grampy, who is in all our hearts. Special

thanks to my big brother, Jim, who has been an inspiration and a role model to me from day 1. To my dog, Copper, for bringing me such happiness and unconditional love. And last, but certainly not least, to my wonderful parents, Deb and Scott. I would not be the woman I am today without your constant love and encouragement.

Finally, I am thankful to the Laird family and Fellows for allowing me to be a part of such a special fellowship.

## **DEDICATION**

To my family for their endless love and support.

And to my grandmother, Beverly Valcourt, who has courageously fought and beaten breast cancer.

## TABLE OF CONTENTS

LIST OF TABLES .....	xiii
LIST OF FIGURES .....	xiv
ABSTRACT .....	xxiv

### Chapter

1	INTRODUCTION .....	1
1.1	An Introduction to Triple-Negative Breast Cancer .....	2
1.2	The Evolution of Current Cancer Treatments and the Need for Novel Therapeutic Strategies .....	3
1.3	Biological Characteristics of Triple-Negative Breast Cancer .....	5
1.3.1	Notch Signaling in Triple-Negative Breast Cancer .....	6
1.3.2	The Role of p53 Apoptotic Signaling and Bcl-2 in Triple- Negative Breast Cancer .....	11
1.3.3	The Role of miR-34a in TNBC and its Interplay with p53 Apoptotic Signaling .....	13
1.3.4	The Need for Delivery Technologies to Manipulate TNBC Biology .....	17
1.4	Nanotechnology in Cancer Treatment .....	17
1.4.1	Photoresponsive Nanomedicines .....	19
1.4.2	Nanotechnology to Enable Drug and Antibody Delivery .....	22
1.4.3	Nanotechnology for Nucleic Acid Delivery .....	27
1.5	Poly(Lactic Co-Glycolic Acid) Nanoparticles in Cancer Therapy .....	31
2	MATERIALS AND METHODS FOR NANOPARTICLE SYNTHESIS AND CHARACTERIZATION .....	33
2.1	Single Emulsion Solvent Evaporation Method for the Encapsulation of Hydrophobic Cargo .....	33
2.2	Double Emulsion Solvent Evaporation Method for Encapsulation of Hydrophilic Cargo .....	34
2.3	Antibody Functionalization of Nanoparticles .....	35

2.4	Characterization Methods.....	36
2.4.1	UV-Visible Spectroscopy and Absorbance Readings .....	36
2.4.2	Dynamic Light Scattering and Zeta Potential .....	37
2.4.3	Electron Microscopy .....	37
2.4.4	Quantification of miRNA Loading in Nanoparticles .....	38
2.4.5	Quantification of Antibody Loading onto Nanoparticles.....	38
2.5	Conclusions .....	38
3	DELIVERY OF IR820 DYE FOR PHOTOTHERMAL THERAPY .....	40
3.1	Introduction .....	40
3.2	Materials and Methods .....	45
3.2.1	Synthesis of IR820-NPs .....	45
3.2.2	Stability and Heating Capacity .....	45
3.2.3	Cell Culture .....	47
3.2.4	Cellular Binding and Uptake .....	47
3.2.5	Viability Assay and Mechanism of Cell Death .....	48
3.2.6	Tumor Model.....	50
3.2.7	Biodistribution Study.....	51
3.2.8	Tumor Temperature and Growth.....	52
3.2.9	Biocompatibility .....	52
3.3	Results and Discussion .....	53
3.3.1	IR820 Dye Maintains its Optical Properties when Encapsulated in Stable, Monodisperse Nanoparticles.....	53
3.3.2	IR820-NPs Demonstrate Time- and Dose-Dependent Cellular Binding and Uptake .....	58
3.3.3	IR820 Encapsulated in PLGA Nanoparticles Reduces Effect on Cell Viability in the Absence of Light Activation Compared to Free IR820.....	59
3.3.4	IR820-NPs Enable Proapoptotic Photothermal Therapy <i>In Vitro</i> .....	60
3.3.5	IR820-NPs Maximally Accumulate in Tumors Within 24 Hours .....	63
3.3.6	Photothermal Therapy Mediated by IR820-NPs Provides Sufficient Heating of Tumors.....	64
3.3.7	Photothermal Therapy with IR820-NPs Significantly Reduces Tumor Growth.....	65
3.3.8	Discussion.....	68

3.4	Conclusions .....	73
4	CO-DELIVERY OF NOTCH-1 ANTIBODIES AND ABT-737 FOR TARGETED DRUG DELIVERY .....	75
4.1	Introduction .....	75
4.2	Materials and Methods .....	79
4.2.1	Synthesis of N1-ABT-NPs .....	79
4.2.2	Characterization of N1-ABT-NPs and ABT-737 Release.....	80
4.2.3	Cell Culture .....	81
4.2.4	Notch-1 Receptor Expression.....	82
4.2.5	Cellular Binding and Uptake .....	82
4.2.6	Cell Viability .....	83
4.2.7	Cell Proliferation .....	84
4.2.8	Quantitative Real-Time Polymerase Chain Reaction.....	85
4.2.9	Western Blotting.....	85
4.2.10	Tumor Model.....	86
4.2.11	Biodistribution Study.....	87
4.2.12	Tumor Growth and Survival.....	87
4.2.13	Biocompatibility .....	88
4.3	Results and Discussion .....	89
4.3.1	Characterization of Antibody and Drug Loading in N1-ABT-NPs .....	89
4.3.2	Notch-1 Antibody Functionalization Enables Preferential Nanoparticle Interaction with TNBC Cells .....	92
4.3.3	N1-ABT-NPs Induce TNBC Cell Death and Reduce Proliferation <i>In Vitro</i> .....	94
4.3.4	N1-ABT-NPs Regulate Bcl-2 and Notch Signaling in TNBC Cells.....	97
4.3.5	Notch-1 Functionalization Enhances Nanoparticle Tumor Accumulation and Retention <i>In Vivo</i> .....	99
4.3.6	N1-ABT-NPs Reduce Tumor Burden and Extend Survival <i>In Vivo</i> .....	100
4.3.7	Discussion.....	104
4.4	Conclusions .....	106
5	CO-DELIVERY OF NOTCH-1 ANTIBODIES AND MIR-34A FOR GENE REGULATION.....	107
5.1	Introduction .....	107

5.2	Materials and Methods .....	110
5.2.1	Synthesis of N1-34a-NPs .....	110
5.2.2	Characterization of N1-34a-NPs .....	111
5.2.3	Cell Culture .....	112
5.2.4	Cellular Binding and Uptake .....	112
5.2.5	Quantitative Real-Time Polymerase Chain Reaction.....	113
5.2.6	Western Blotting.....	114
5.2.7	Cellular Senescence.....	115
5.2.8	Cell Proliferation .....	115
5.2.9	Cell Migration .....	116
5.3	Results and Discussion .....	116
5.3.1	Characterization of Antibody and miRNA Loading in N1-34a-NPs and Interaction with TNBC Cells .....	116
5.3.2	N1-34a-NPs Regulate Notch Signaling and Downstream miR-34a Targets .....	119
5.3.3	N1-34a-NPs Induce Senescence and Reduce TNBC Cell Proliferation and Migration <i>In Vitro</i> .....	122
5.3.4	Discussion.....	124
5.4	Conclusions .....	127
6	CONCLUSIONS AND FUTURE WORK.....	128
6.1	Introduction .....	128
6.2	IR820-NPs as Potent Mediators of Photothermal Therapy .....	128
6.3	N1-ABT-NPs as an Effective Strategy for Targeted Drug Delivery.....	130
6.4	N1-34a-NPs for Gene Regulation .....	132
6.5	Future Directions .....	133
6.5.1	Formulation Optimization .....	134
6.5.2	Tumor Models .....	135
6.5.3	Evaluation of Notch-1 Expression.....	137
6.5.4	Dosing/Treatment Regimen Optimization and Further <i>In Vivo</i> Analysis .....	138
6.5.5	Improving Nanoparticle Penetration with Photothermal Therapy .....	140
6.5.6	Versatility of a Platform Enabling Bcl-2 Inhibition .....	140
6.5.7	Conclusions .....	141
	REFERENCES .....	142

## LIST OF TABLES

Table 4.1: Primer sequences used for qPCR. Reproduced from Valcourt, <i>et al. ACS Nano</i> (2020); 14(3): 3378-3388. [230].....	85
Table 5.1: Sequences of miR-Co and miR-34a. Reproduced from Valcourt DM, Day ES, Manuscript in revision. ....	111
Table 5.2: Primer sequences used for qPCR. Reproduced from Valcourt DM, Day ES, Manuscript in revision. ....	113

## LIST OF FIGURES

- Figure 1.1: Simplified scheme depicting the interplay between Notch signaling, Bcl-2, and miR-34a. Notch signaling is overactive in TNBC, promoting the transcription of genes associated with cell survival and proliferation and inhibiting the pro-apoptotic protein Noxa. Noxa displaces Bcl-2 family proteins, which are overexpressed in TNBC, from mitochondria-bound Bax to promote apoptosis. Bcl-2 and Notch expression are also regulated by miR-34a signaling, which is reduced in TNBC, thus contributing to disease progression..... 6
- Figure 1.2: Dysregulation of the developmental Wnt, Notch, and Hedgehog signaling pathways is implicated in all of the “hallmarks” of cancer, and all three pathways are hyperactive in TNBC. Reproduced from Valcourt, *et al. Annals Biomed Eng.* 2019. [4]..... 8
- Figure 1.3: Canonical Notch signaling is activated when Jagged or Delta ligands on a signal-sending cell bind the extracellular domain of the Notch receptor on a signal-receiving cell. The extracellular domain of Notch is subsequently cleaved by ADAM family proteases, then the intracellular domain (NICD) is cleaved by the  $\gamma$ -secretase complex. Released NICD translocates to the nucleus, where it acts as a promoter for the transcription of downstream target genes that support cell survival, proliferation, stemness, and other oncogenic behaviors. Reproduced from Valcourt, DM, Dang MN, Scully MA, Day ES, manuscript in revision. .... 10
- Figure 1.4: Simplified scheme of the p53 apoptotic signaling pathway in healthy cells versus TNBC cells. (a) Upon activation in healthy cells, acetylated p53 migrates to the mitochondria to induce Bax-mediated release of cytochrome c. There is a subsequent series of activation of caspases that ultimately leads to apoptosis. (b) In TNBC cells, Bcl-2 proteins are overexpressed, leading to inhibition of apoptotic signaling. .... 12

Figure 1.5: Scheme of miRNA biogenesis and mechanism of gene regulation. miRNAs are transcribed as pri-miRNAs in the nucleus, which are subsequently cleaved by Drosha to form pre-miRNAs. pre-miRNAs are then transported to the cytoplasm by exportin proteins. Cytoplasmic pre-miRNAs with unstable stem-loop structures are further cleaved by Dicer into small duplex RNA structures (miRNA:miRNA\*) that contain both mature miRNA and its complementary strand (miRNA\*). The miRNA\* strand is typically degraded, and the mature miRNA strand assembles into RISC and guides it to specific messenger RNAs (mRNAs) to induce gene silencing. Reproduced from Kapadia, *et al. J Appl Polym Sci.* 2019. [5] ..... 15

Figure 1.6: Upon activation of p53, miR-34a is processed and regulates gene expression to induce apoptosis, cell cycle arrest, and senescence, and inhibit cell migration. Reproduced from Hermeking, H. *Cell Death and Differentiation.* 2010. [84]..... 17

Figure 1.7: Scheme depicting how nanoparticles enhance drug delivery to solid tumors. After intravenous injection, nanoparticles passively accumulate in tumors (A) through leaky vasculature. Surface functionalized nanoparticles then enable active targeting (B) by binding to cell receptors. Reproduced from Dong. *Nanomed.* 2010. [104] ..... 19

Figure 1.8: Schematic of nanoparticle-mediated photothermal therapy. In nanoparticle-mediated photothermal therapy, (a) nanoparticles first accumulate in the tumor through leaky vasculature. (b) When these nanoparticles are irradiated with near-infrared (NIR) light, they convert the light into heat. (c) The heat shock induced by this irradiation then leads to tumor cell death. Modified from Riley, R.S. *WIREs.* 2017. [108]..... 20

Figure 1.9: The absorption of light by the major components of tissue: water, hemoglobin, and oxyhemoglobin. The near-infrared (NIR) window represents the region of wavelengths of light that is minimally absorbed by these components. Adapted from Weissleder. *Nat Biotechnol.* 2001. [111] ..... 21

Figure 1.10: In cancer cells, ligand/receptor interactions activate downstream oncogenic signaling. Antibodies can reduce signaling by competitively blocking signaling ligands from binding the receptor and locking the receptor in a non-responsive state. Antibody-nanoparticle conjugates can enhance signaling cascade interference by engaging multiple receptors simultaneously. Modified from Valcourt, D.M. <i>Annals Biomed Eng.</i> 2019. [4] .....	27
Figure 1.11: Scheme depicting the biological barriers that miRNA nanocarriers must overcome. To enable gene regulation, miRNA nanocarriers must: (1) prevent miRNA degradation from serum nucleases and provide long circulation in the blood, (2) cross vessel walls and penetrate through the extracellular matrix (ECM), (3) enter target cells, (4) facilitate endolysosomal escape, and (5) release miRNA in the cytoplasm for loading into the RNA-induced silencing complex (RISC) for subsequent gene regulation. Reproduced from Kapadia, <i>et al. J Appl Polym Sci.</i> 2019. [5].....	28
Figure 1.12: Chemical structure of poly(lactic co-glycolic acid).....	31
Figure 2.1: Single emulsion solvent evaporation method for encapsulation of hydrophobic cargo in poly(lactic co-glycolic acid) (PLGA) nanoparticles. Modified from Valcourt DM, Dang MN, Scully MA, Day ES, Manuscript in revision. ....	34
Figure 2.2: Double emulsion solvent evaporation method for encapsulation of hydrophilic cargo (e.g. miRNA) in poly(lactic co-glycolic acid) (PLGA) nanoparticles. Modified from Valcourt DM, Day ES, Manuscript in revision.....	35
Figure 2.3: Crosslinking reaction scheme for antibody functionalization of poly(lactic co-glycolic acid) nanoparticles using 1-ethyl-3-(3-dimethylaminopropyl)carbodiimide (EDC) chemistry with the addition of n-hydroxysulfosuccinimide (sulfo-NHS). Taken from “Carbodiimide Crosslinker Chemistry”. <i>ThermoFisher Scientific.</i> [150] .....	36
Figure 3.1: Characterization of IR820-NPs. (a) Scheme of IR820-loaded PLGA nanoparticles. (b) TEM image showing the size and morphology of IR820-NPs. Scale bar = 100 nm. Modified from Valcourt, <i>et al. JBMRA.</i> 2019. [192].....	53

Figure 3.2: Evaluating the heating capacity of free IR820 dye and IR820-NPs. (a) The heating profile of free IR820 dye and IR820-NPs upon laser irradiation with an 808 nm laser at 1.5 W/cm<sup>2</sup>. (b) The heating profile of IR820-NPs suspended in phosphate buffered saline at 10, 25, or 35 μm upon irradiation with an 808 nm laser at 1.5 W/cm<sup>2</sup>. (c) The heating profile of IR820-NPs suspended in phosphate buffered saline at 25 μm upon irradiation with an 808 nm laser at 0.5, 1, 1.5, 2, or 3 W/cm<sup>2</sup>. Modified from Valcourt, *et al. JBMRA*. 2019. [192] ..... 55

Figure 3.3: The absorption profile of free IR820 dye and IR820-NPs before and after storage in water at 4°C for 30 days as determined by UV-visible spectroscopy. The concentration of IR820 is 25 μm for both free and encapsulated dye. Modified from Valcourt, *et al. JBMRA*. 2019. [192]. 56

Figure 3.4: Evaluating the stability of IR820-NPs upon laser irradiation. (a) The absorption profile of IR820-NPs (suspended in phosphate buffered saline at 25 μm) before and after irradiation with the 808 nm laser for 5 minutes at 1.5 W/cm<sup>2</sup> as determined by UV-visible spectroscopy. (b) The hydrodynamic diameter (gray bars) and polydispersity index (red dots) of IR820-NPs before and after irradiation with the 808 nm laser for 5 minutes at 1.5 W/cm<sup>2</sup>. Modified from Valcourt, *et al. JBMRA*. 2019. [192] ..... 57

Figure 3.5: Evaluating the stability of IR820-NPs in storage conditions. (a) The hydrodynamic diameter and polydispersity index of IR820-NPs as determined by dynamic light scattering when stored in water at 4°C for 30 days. (b) The release of IR820 from IR820-NPs during storage in water at 4°C as determined by UV-visible spectroscopy. Modified from Valcourt, *et al. JBMRA*. 2019. [192] ..... 58

Figure 3.6: Flow cytometric analysis of the cellular binding and uptake of IR820-NPs based on (a) dose and (b) time of incubation. Modified from Valcourt, *et al. JBMRA*. 2019. [192] ..... 59

Figure 3.7: Relative metabolic activity of MDA-MB-231 TNBC cells exposed to free IR820 dye or IR820-NPs without light exposure. \*p<0.05 Modified from Valcourt, *et al. JBMRA*. 2019. [192] ..... 60

Figure 3.8: Relative metabolic activity of MDA-MB-231 cells that received photothermal therapy mediated by IR820-NPs at 35 μm and laser irradiation versus control cells that were exposed to only saline, only IR820-NPs at 35 μm, or saline and laser irradiation. \*p<0.05 versus untreated control. Modified from Valcourt, *et al. JBMRA*. 2019. [192]. 61

- Figure 3.9: Evaluation of mechanism of cell death induced by photothermal therapy mediated by IR820-NPs. (a) The percentage of apoptotic cells in MDA-MB-231 samples that were exposed to no treatment, laser irradiation only, IR820-NPs only (10  $\mu\text{m}$ ), or photothermal therapy (IR820-NPs and laser irradiation; 10  $\mu\text{m}$ ). #p=0.1 versus untreated control (b) Representative scatter plots demonstrating the fraction of MDA-MB-231 cells in early apoptosis (bottom right quadrant), late apoptosis (top right quadrant), or necrosis (top left quadrant) following treatment with media only, laser irradiation only, IR820-NPs only, or photothermal therapy (IR820-NPs and laser irradiation). Red color indicates a high density of cells and blue color indicates a low density of cells. Modified from Valcourt, *et al. JBMRA*. 2019. [192] ..... 62
- Figure 3.10: Investigating the biodistribution of IR820-NPs *in vivo*. (a) Mean fluorescence intensity (MFI) of IR820 in tumors of mice at different times post-intravenous injection of IR820-NPs. The inset displays a representative image of IR820-NP fluorescence at 24 hours after injection and the region of interest (ROI) in which the fluorescence intensity was measured. (b) *Ex vivo* analysis of IR820 signal in the brain, heart, liver, lungs, spleen, kidneys, and tumors of mice 24 hours after they received intravenous injections of IR820-NPs or saline. Modified from Valcourt, *et al. JBMRA*. 2019. [192] ..... 64
- Figure 3.11: Mean tumor temperature in mice treated with saline, free IR820 dye, or IR820-NPs during laser irradiation. These temperatures were recorded during the first of four treatment cycles. The red line at 42°C indicates the threshold considered sufficient to induce photothermal therapy under the conditions in this study. Modified from Valcourt, *et al. JBMRA*. 2019. [192]..... 65
- Figure 3.12: Tumor growth following photothermal therapy mediated by free IR820 dye or IR820-NPs. (a) Tumor volume versus time in mice exposed to photothermal therapy mediated by IR820-NPs or various control treatments. All treatments were injected intravenously at an IR820 concentration of 350  $\mu\text{M}$ . Mice whose tumors received laser exposure were irradiated at 1.5  $\text{W}/\text{cm}^2$  for five minutes. Black arrows indicate the days of treatment injections (days 0, 7, 14, and 21) and red arrows indicate the days of laser irradiation (days 1, 8, 15, and 22). \*\*p<0.01 (b) Image of all tumors excised from individual mice at the time of euthanization (day 30). (c) Tumor volume growth curves for individual mice in each treatment group (treated as described in part (a)). Modified from Valcourt, *et al. JBMRA*. 2019. [192] ..... 67

Figure 3.13: (a) Hematoxylin and eosin staining of major organs in mice exposed to saline, free IR820 dye, or IR820-NPs. Scale bars = 200 $\mu\text{m}$ (b) Hematoxylin and eosin staining of tumors in mice exposed to photothermal therapy mediated by IR820-NPs or various controls as indicated. Scale bars = 50 $\mu\text{m}$ . Modified from Valcourt, <i>et al. JBMRA</i> . 2019. [192] .....	68
Figure 4.1: Depiction of how Notch signaling and Bcl-2 contribute to TNBC progression. Notch signaling is activated in TNBC cells when overexpressed Notch-1 receptors interact with Jagged or Delta ligands on neighboring cells. This leads to cleavage of the Notch intracellular domain (NICD), which translocates to the nucleus to activate signaling that supports TNBC cell survival, proliferation, and apoptosis suppression. Bcl-2 is an anti-apoptotic protein that is also overexpressed in TNBC and contributes to poor clinical outcomes. Reproduced from Valcourt, <i>et al. ACS Nano</i> (2020); 14(3): 3378-3388. [230] .....	76
Figure 4.2: Characterization of N1-ABT-NPs. (a) Hydrodynamic diameter and zeta potential of ABT-737-loaded nanoparticles before and after antibody conjugation with IgG or Notch-1 antibodies. (b) Loading of ABT-737 and antibodies before and after antibody conjugation. Modified from Valcourt, <i>et al. ACS Nano</i> (2020); 14(3): 3378-3388. [230].....	90
Figure 4.3: ABT-737 release from N1-ABT-NPs in storage (4°C, water) and physiological (37°C, phosphate buffered saline (PBS)) conditions. Modified from Valcourt, <i>et al. ACS Nano</i> (2020); 14(3): 3378-3388. [230] .....	91
Figure 4.4: Serum stability of N1-ABT-NPs. (a) Hydrodynamic diameter and (b) zeta potential of N1-ABT-NPs in 0%, 10%, 50%, and 100% fetal bovine serum (FBS) over 24 hours. Valcourt, <i>et al. ACS Nano</i> (2020); 14(3): 3378-3388. [230] .....	92
Figure 4.5: Immunocytochemistry staining for the Notch-1 receptor (dark red signal) in MCF-10A healthy mammary cells and MDA-MB-231 TNBC cells. Scale bars = 100 $\mu\text{m}$ . Modified from Valcourt, <i>et al. ACS Nano</i> (2020); 14(3): 3378-3388. [230].....	92

Figure 4.6: Analysis of N1-DiD-NPs' interaction with TNBC cells versus healthy breast epithelial cells. (a) Fluorescence microscopy images showing MDA-MB-231 TNBC cells treated with no nanoparticles, IgG-DiD-NPs, or N1-DiD-NPs. Cell nuclei are blue (DAPI), actin is green (Phalloidin), and nanoparticles are red (DiD). Scale bars = 50  $\mu$ m. (b) Representative flow cytometry histograms of MDA-MB-231 TNBC cells exposed to IgG-DiD-NPs or N1-DiD-NPs. (c) Median DiD fluorescence intensity of MDA-MB-231 TNBC cells and healthy MCF-10A mammary cells treated with N1-DiD-NPs or IgG-DiD-NPs as measured by flow cytometry. Reproduced from Valcourt, *et al. ACS Nano* (2020); 14(3): 3378-3388. [230]..... 94

Figure 4.7: Relative metabolic activity of MDA-MB-231 cells treated with different doses of freely delivered IgG or Notch-1 (N1) antibodies and ABT-737 or with nanocarriers (IgG-ABT-NPs or N1-ABT-NPs) as measured by an MTT assay. Horizontal dotted line indicates 50% reduction in metabolic activity. Modified from Valcourt, *et al. ACS Nano* (2020); 14(3): 3378-3388. [230]..... 95

Figure 4.8: Analysis of the impact of N1-ABT-NPs on TNBC cell proliferation. (a) Percent proliferation of MDA-MB-231 TNBC cells that were untreated or exposed to IgG-ABT-NPs or N1-ABT-NPs. \* $p < 0.05$  (b) Representative flow cytometry histograms for EdU proliferation assay. Modified from Valcourt, *et al. ACS Nano* (2020); 14(3): 3378-3388. [230] ..... 96

Figure 4.9: Scheme of proposed NP interaction with MDA-MB-231 TNBC cells. Upon cellular binding, N1-ABT-NPs suppress Notch signaling through antibody-mediated signal cascade interference and also release ABT-737 to inhibit Bcl-2 and activate apoptosis. Modified from Valcourt, *et al. ACS Nano* (2020); 14(3): 3378-3388. [230]..... 97

Figure 4.10: qPCR analysis of relative Bcl-2, Noxa, Hes5, and HeyL mRNA expression after treatment with IgG- or N1-ABT-NPs compared to control (untreated) cells. RPLPO was used as a control and relative mRNA expression in nanoparticle-treated groups is normalized to that of untreated cells. \* $p < 0.05$ , ## $p = 0.06$ , # $p = 0.07$  Modified from Valcourt, *et al. ACS Nano* (2020); 14(3): 3378-3388. [230]..... 98

- Figure 4.11: Examination of the effects of N1-ABT-NPs on Notch signaling and Bcl-2 expression in TNBC cells. (a) Quasi-quantitative analysis of Western blotting for normalized Bcl-2, cleaved Notch-1, and Hes1 protein expression.  $\beta$ -actin was used as a control and expression in nanoparticle-treated samples was normalized to expression in untreated cells.  $**p < 0.01$  (b) Representative Western blot bands for Bcl-2, cleaved Notch-1, Hes1, and  $\beta$ -actin protein levels. Modified from Valcourt, *et al. ACS Nano* (2020); 14(3): 3378-3388. [230]..... 99
- Figure 4.12: *In vivo* evaluation of tumor accumulation of N1-ABT-NPs. (a) Relative mean fluorescence intensity of DiD in subcutaneous MDA-MB-231 tumors in mice 0, 6, 12, and 24 hours post-intravenous injection of IgG-DiD-NPs or N1-DiD-NPs (n=6). (b) Representative fluorescence images of a mouse treated with N1-DiD-NPs at 0, 12, and 24 hours after injection. Circles indicate the region of interest (ROI) where fluorescence intensity was measured. Modified from Valcourt, *et al. ACS Nano* (2020); 14(3): 3378-3388. [230]..... 100
- Figure 4.13: Average percent change in tumor volume (n=6 mice/group) after one and three weeks of treatment with saline, IgG-ABT-NPs, or N1-ABT-NPs at 10 mg ABT-737/kg once per week.  $\#p < 0.1$ ,  $*p < 0.05$  Modified from Valcourt, *et al. ACS Nano* (2020); 14(3): 3378-3388. [230]..... 101
- Figure 4.14: Kaplan-Meier survival curves for mice bearing subcutaneous MDA-MB-231 TNBC tumors that were treated intravenously with saline, IgG-ABT-NPs, or N1-ABT-NPs at 10 mg ABT-737/kg twice per week for four weeks (n=8 mice/group). Black arrows on the x-axis indicate days of treatment.  $\#p = 0.10$  Modified from Valcourt, *et al. ACS Nano* (2020); 14(3): 3378-3388. [230]..... 102
- Figure 4.15: Mouse weight and major organ histopathology following treatment with N1-ABT-NPs. (a) Average weight of mice bearing subcutaneous MDA-MB-231 tumors that were treated with saline, IgG-ABT-NPs, or N1-ABT-NPs twice weekly for 8 total injections (n=8 mice/group). (b) Hematoxylin and eosin staining of representative major organs excised from tumor-bearing mice treated with saline, IgG-ABT-NPs, or N1-ABT-NPs twice weekly for four weeks as described in part (a). Scale bars = 100  $\mu$ m. Reproduced from Valcourt, *et al. ACS Nano* (2020); 14(3): 3378-3388. [230] ..... 104

Figure 5.1: Characterization of N1-34a-NPs. (a) Hydrodynamic diameter and zeta potential of bare miR-Co-NPs, bare miR-34a-NPs, IgG-Co-NPs, IgG-34a-NPs, N1-Co-NPs, and N1-34a-NPs. Error bars indicate standard error. (b) Encapsulation efficiency of miRNA and loading of antibodies on the different nanoparticle formulations used in this study. Modified from Valcourt DM, Day ES, Manuscript in revision.. 118

Figure 5.2: Evaluation of nanoparticle binding to MDA-MB-231 cells. (a) Representative flow cytometry histogram of MDA-MB-231 TNBC cells exposed to N1-Cy5-NPs for increasing amounts of time. (b) Median Cy5 fluorescence intensity of MDA-MB-231 TNBC cells treated with IgG-Cy5-NPs or N1-Cy5-NPs for different amounts of time as measured by flow cytometry. Error bars indicate standard error. Modified from Valcourt DM, Day ES, Manuscript in revision... 119

Figure 5.3: Scheme of posited nanoparticle interaction with MDA-MB-231 TNBC cells. Upon cellular binding and uptake, N1-34a-NPs inhibit downstream Notch signaling through antibody-mediated signal cascade interference and also deliver miR-34a, which reduces the expression of several genes by guiding the RNA induced silencing complex (miRISC) to targeted mRNA sequences with perfect (1) or imperfect (2) complementarity, resulting in mRNA degradation or translational repression. Modified from Valcourt DM, Day ES, Manuscript in revision..... 120

Figure 5.4: Evaluation of nanoparticle-mediated gene regulation. (a) qPCR analysis of relative Bcl-2, survivin, CCND1, Notch-1, MDR1, and Hes5 mRNA expression after treatment with IgG-Co-NPs, IgG-34a-NPs, N1-Co-NPs, or N1-34a-NPs. GUSB was used as a control and relative mRNA expression is normalized to that of cells treated with IgG-Co-NPs. Error bars indicate standard error. # $p < 0.1$ , \* $p < 0.05$ , \*\* $p < 0.01$  (b) Quazi-quantitative analysis of Western blotting for normalized Bcl-2, CCND1, Notch-1, and Hes1 protein expression. A-tubulin was used as a control and expression was normalized to expression in cells treated with IgG-Co-NPs. Error bars indicate standard error. \* $p < 0.05$ , \*\* $p < 0.01$  (c) Representative Western blot bands for Bcl-2, CCND1, Notch-1, Hes1, and  $\alpha$ -tubulin protein levels. Bands are from a single blot that was stripped and probed for multiple targets. Modified from Valcourt DM, Day ES, Manuscript in revision. .... 121

Figure 5.5: Representative images of SA $\beta$ Gal assay of MDA-MB-231 cells treated with IgG-Co-NPs, IgG-34a-NPs, N1-Co-NPs, or N1-34a-NPs. Green color indicates  $\beta$ -galactosidase activity. Scale bars = 50  $\mu$ m. Modified from Valcourt DM, Day ES, Manuscript in revision. .... 122

Figure 5.6: Percent proliferation of MDA-MB-231 cells treated with IgG-Co-NPs, IgG-34a-NPs, N1-Co-NPs, or N1-34a-NPs normalized to that of cells treated with IgG-Co-NPs. Error bars indicate standard error. \* $p < 0.05$  Modified from Valcourt DM, Day ES, Manuscript in revision. .... 123

Figure 5.7: Effect of N1-34a-NPs on TNBC cell migration. (a) Normalized number of GFP-expressing MDA-MB-231 cells migrated through transwell insert after treatment with IgG-Co-NPs, IgG-34a-NPs, N1-Co-NPs, or N1-34a-NPs. Error bars indicate standard error. (b) Representative fluorescence images of GFP-expressing MDA-MB-231 cells migrated through transwell insert after treatment with IgG-Co-NPs, IgG-34a-NPs, N1-Co-NPs, or N1-34a-NPs. Scale bars = 500  $\mu$ m. Modified from Valcourt DM, Day ES, Manuscript in revision. .... 124

Figure 6.1: Scheme depicting the therapeutic potential of IR820-NPs as potent mediators of photothermal therapy both *in vitro* and *in vivo*. .... 129

Figure 6.2: Scheme depicting the therapeutic potential of N1-ABT-NPs as targeted drug delivery vehicles both *in vitro* and *in vivo*. Modified from Valcourt DM, Dang MN, Scully MA, Day ES, Manuscript in revision. 131

Figure 6.3: Scheme depicting the therapeutic potential of N1-34a-NPs for gene regulation *in vitro*. .... 133

## ABSTRACT

Triple-negative breast cancer (TNBC) is an aggressive disease that accounts for 15-25% of all breast cancer cases and is characterized by its cells' lack of expression of the three most common surface receptors detected on other subtypes: estrogen receptor, progesterone receptor, and human epidermal growth factor receptor 2. This lack of expression makes TNBC unsusceptible to current targeted or hormonal therapies, so new treatment strategies are desperately needed. This thesis makes progress towards this goal by developing poly(lactic co-glycolic acid) (PLGA) nanoparticles that can enable treatment of TNBC through three distinct mechanisms. PLGA is an ideal carrier material because the Food and Drug Administration (FDA) has already approved this polymer for human clinical use, and it readily degrades into non-toxic byproducts in the body, allowing for the creation of safe and effective therapeutics. Chapter 1 of this thesis provides an introduction to TNBC biology and the current state of cancer nanomedicine, while Chapter 2 describes common methods used in this work. The remaining Chapters discuss the specific therapies developed in this dissertation and provide insight on directions for future development.

The first objective of this thesis was to enable photothermal therapy (PTT) of TNBC using a biodegradable nanoparticle platform. PTT utilizes nanoparticles embedded in tumors as exogenous energy absorbers to convert externally applied near-infrared (NIR) light into heat to ablate cancer cells, and it has shown much promise as a novel cancer treatment strategy. Historically, PTT has utilized gold-based

nanoparticles to produce heat, but these materials will remain in the body indefinitely with unknown long-term health effects. To enable PTT with a biodegradable platform, we loaded PLGA nanoparticles with the NIR-absorbing dye, IR820. In Chapter 3, we demonstrate that these IR820-NPs are potent mediators of pro-apoptotic TNBC cell death *in vitro* and can significantly reduce tumor burden in murine TNBC xenograft models *in vivo*.

While PTT can be used to treat relatively superficial or accessible tumors, it is not well suited for treatment of tumors located in regions where NIR light cannot penetrate. Thus, the second and third objectives of this thesis developed a more widely applicable therapeutic strategy: using PLGA nanoparticles as delivery vehicles to regulate oncogenic signaling pathways in TNBC cells and tumors. In TNBC, the anti-apoptotic protein Bcl-2 is overexpressed, contributing to drug resistance. Prior studies have shown that the small molecule drug ABT-737, which inhibits Bcl-2 to reinstate apoptotic signaling, is a promising candidate for TNBC therapy. However, ABT-737 is poorly soluble in aqueous conditions and its orally bioavailable derivative causes severe thrombocytopenia. To enable targeted delivery of ABT-737 to TNBC and enhance its therapeutic efficacy, we encapsulated the drug in PLGA nanoparticles that were functionalized with Notch-1 antibodies to produce N1-ABT-NPs. The antibodies in this nanoparticle platform enable both TNBC cell-specific binding and suppression of Notch signaling within TNBC cells by locking the Notch-1 receptors in a ligand unresponsive state. This Notch inhibition potentiates the effect of ABT-737 by up-regulating Noxa, resulting in effective killing of TNBC cells. In Chapter 4, we present the results of *in vitro* studies that demonstrate N1-ABT-NPs can preferentially bind TNBC cells versus non-cancerous breast epithelial cells to effectively regulate Bcl-2

and Notch signaling to induce cell death. Further, we show that N1-ABT-NPs can accumulate in subcutaneous TNBC xenograft tumors in mice following systemic administration to reduce tumor burden and extend animal survival.

In Chapter 5, we introduce an alternative treatment strategy for TNBC that exploits its overexpression of Notch-1 receptors to enable targeted microRNA (miRNA) delivery. Studies have shown that introducing mimics of the tumor suppressive miRNA miR-34a to TNBC cells can effectively inhibit cancer growth, but miR-34a cannot be administered in the clinic without a carrier. To enable delivery of miR-34a to TNBC cells, we encapsulated miR-34a mimics in PLGA nanoparticles that were functionalized with Notch-1 antibodies to produce N1-34a-NPs. As in our second objective, the antibodies in this formulation not only enable binding of Notch-1 receptors overexpressed on the surface of TNBC cells, but also facilitate suppression of Notch signaling through signal cascade interference. The results presented in Chapter 5 demonstrate that N1-34a-NPs can regulate Notch signaling and downstream miR-34a targets in TNBC cells to induce senescence and reduce cell proliferation and migration. Thus, these nanoparticles are worthy of continued development as promising tools to combat TNBC.

In summary, this dissertation describes the development of three novel nanoparticles that can treat TNBC through distinct mechanisms: photothermal therapy, targeted drug delivery, and targeted miRNA replacement therapy. Future directions for this research are summarized in Chapter 6. With continued development and implementation, each of these nanoparticle formulations has great potential to improve patient outcomes.

## **Chapter 1**

### **INTRODUCTION**

Every year in the United States almost two million new cases of cancer are diagnosed and over half a million cancer-related deaths occur. [1] Since its peak in 1991, the cancer mortality rate has dropped approximately 1.5% every year, leading to an overall decline of 27% between 1991 and 2016. [2] This decreased death rate can largely be attributed to educational advances, including those warning against the dangers of smoking, and improvements in the areas of early detection and treatment. Despite these promising changes, in 2016, cancer was still the second leading cause of death after heart disease, accounting for 22% of all deaths. [2] Further, projected statistics for 2019 indicate that almost 1,700 Americans will have died daily from cancer that year. [3] This underscores the need for new and improved cancer therapies.

The overarching goal of this dissertation was to develop novel, nanoparticle-based treatment strategies for cancer, particularly triple-negative breast cancer (TNBC). This chapter discusses current treatment strategies for TNBC and introduces concepts that led to the development of the nanoparticles presented in this dissertation. Chapter 2 describes the methods used to synthesize and characterize the nanoparticles in this work, and Chapters 3-5 describe the specific nanoparticle therapies that we developed for TNBC. Throughout this work, we used poly(lactic co-glycolic acid) (PLGA) nanoparticles as a versatile platform to enable treatment of TNBC through three distinct mechanisms: photothermal therapy (Chapter 3), targeted drug delivery (Chapter 4), and gene regulation (Chapter 5). Finally, Chapter 6 discusses future

directions for the field that build upon this research. Some of the text in this chapter has been adapted from my following publications:

- (1) Valcourt DM, *et al. Annals Biomed. Eng.* 2019; 1-21. [4]
- (2) Kapadia CH, *et al. J. Appl. Polym. Sci.* 2019; 48651:1-16. [5]
- (3) Valcourt DM, *et al. Nano Research.* 2018; 11(10):4999-5016. [6]

### **1.1 An Introduction to Triple-Negative Breast Cancer**

In a study of projected cancer statistics in 2019, Jemal and colleagues found that breast cancer accounts for 30% of all new cancer diagnoses in women, which corresponds to approximately 270,000 new cases in the United States that year. [3] In fact, breast cancer is the most common form of cancer overall, according to the National Cancer Institute's estimated new cases in 2018. [1] Despite the frequency at which it occurs, unfortunately, breast cancer treatment and prognosis differs significantly from patient to patient. These differences are largely derived from the biological disparities between the subtypes of breast cancer, which are typically delineated based on the expression of three common cell surface receptors: the estrogen receptor (ER), progesterone receptor (PR), and human epidermal growth factor receptor 2 (HER2). [7] Varying expression levels of these receptors yield four major subtypes of breast cancer: ER/PR<sup>+</sup>Her2<sup>+</sup>, ER/PR<sup>+</sup>Her2<sup>-</sup>, ER/PR<sup>-</sup>Her2<sup>+</sup>, and ER/PR<sup>-</sup>Her2<sup>-</sup>. The latter subtype, also known as triple-negative breast cancer (TNBC), accounts for 15-25% of all breast cancer cases and has the highest mortality and recurrence rates of all subtypes. [7-12] The following section discusses the current standards for treatment of breast cancer as a whole and introduces the need for new therapeutic strategies for TNBC.

## **1.2 The Evolution of Current Cancer Treatments and the Need for Novel Therapeutic Strategies**

The earliest recorded cases of breast cancer date back to 3,000-2,500 B.C. in ancient Greece, at which time the only hope of finding relief was through votive offerings in the shape of a breast that were presented to the god of medicine, Asclepius. [13, 14] Since these times, treatment strategies for breast cancer have evolved dramatically, leading to the three major classes of cancer therapy used today: surgery, radiation, and chemotherapy. The first surgical removal of breast cancer by Leonides of Alexandria in the 1<sup>st</sup> century A.D marks the beginning of an extended period in which little progress was made towards improved cancer management strategies. In fact, the detailed reports of his surgical strategy laid the groundwork for contemporary surgical practices. The Renaissance saw a resurgence of surgical innovation with the “father” of investigative surgery, John Hunter, and ushered in an era of radical surgeries in the 19<sup>th</sup> century [13], including the first mastectomy performed in 1882 by William Halsted [14]. This radical strategy focused on removing whole tissues to prevent the spread and recurrence of the disease and remained the standard operation for the treatment of breast cancer into the 20<sup>th</sup> century. [13, 14]

As medical resources advanced in the late 19<sup>th</sup> century and into the 20<sup>th</sup> century, the radical mastectomy treatment strategy for breast cancer was gradually modified to preserve more tissue and combine this approach with newly discovered therapeutic options. In 1895, the X-ray was developed, which led to mammography and enabled earlier detection of lesions, altering surgical management strategies. Then, shortly after its discovery in 1898, radium was introduced as a new therapeutic agent for cancer, becoming the second major class of cancer therapy. By 1937, radiation therapy was used in addition to surgery as a mechanism to spare the breast. [14]

Finally, in 1942, the use of nitrogen mustard (a compound related to the poisonous gases used in World War I) to treat lymphosarcoma gave rise to the third major class of therapies still used for cancer treatment today: chemotherapy. [15]

While surgery, radiation, and chemotherapy can successfully manage cancer, these strategies are highly invasive and have significant off-target effects. Surgical resection of breast cancer is invasive and cannot guarantee the complete removal of cancerous cells. [16] In addition, concerning new evidence suggests that surgery-induced inflammation can actually increase the incidence of metastasis. [17, 18] Similarly, radiation can promote metastasis by disrupting the tumor microenvironment, making it easier for cancer cells to enter the bloodstream. [19] Another limitation of radiation and chemotherapy is that they are not targeted and therefore affect both healthy cells and cancer cells. In fact, chemotherapy can cause serious long-term adverse effects like heart and kidney problems. [20, 21] As more has been revealed about cancer biology and the hormone dependency of breast cancer in particular [22], researchers have begun to develop new targeted therapeutics that can overcome the limitations seen with these conventional treatment approaches.

There are several targeted therapies available for non-TNBC subtypes of breast cancer. For example, many treatments for HER2<sup>+</sup> breast cancer use monoclonal antibodies to target the HER2 protein found on the surface of these cancer cells. [23, 24] The first of these therapies, trastuzumab (Herceptin), was approved by the United States Food and Drug Administration (FDA) in 1998 [14], and has since been joined by pertuzumab (Perjeta), ado-trastuzumab emtansine (Kadcyla), Fam-trastuzumab deruxtecan (Enhertu), and two small molecule inhibitors Lapatinib (Tykerb) and Neratinib (Nerlynx) [24]. For ER/PR<sup>+</sup>Her2<sup>-</sup> subtypes, palbociclib (Ibrance), ribociclib

(Kisqali), abemaciclib (Verzenio), and everolimus (Afinitor) are all FDA approved targeted therapies. [24] Unfortunately, TNBC's characteristic lack of expression of ER, PR, and HER2 leave it unsusceptible to the targeted therapies mentioned above. Thus, new treatment strategies designed specifically for TNBC are desperately needed. This dissertation aims to meet this need with novel nanoparticle-based therapeutic strategies.

### **1.3 Biological Characteristics of Triple-Negative Breast Cancer**

To effectively treat a disease such as TNBC, it is imperative to understand the fundamental biology that drives disease progression. Indeed, the heterogenous nature of cancer still poses a significant challenge for developing effective therapeutic strategies. [25–27] This section provides an overview of some of the specific signaling pathways that are implicated in TNBC and therefore offer an opportunity for therapeutic manipulation. Specifically, this thesis exploits TNBC's aberrant expression of Notch signaling, Bcl-2, and miR-34a. The interplay of these molecules in TNBC is depicted simplistically in **Figure 1.1**. Below, a more detailed description of each pathway is provided.

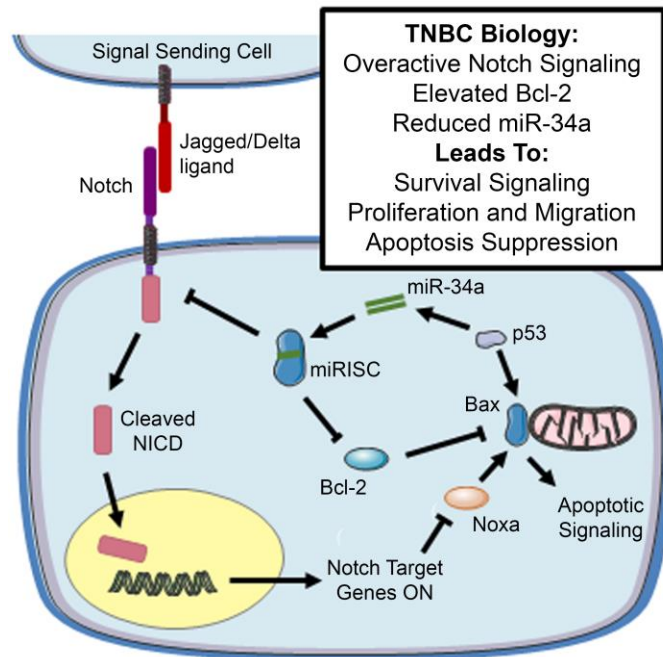


Figure 1.1: Simplified scheme depicting the interplay between Notch signaling, Bcl-2, and miR-34a. Notch signaling is overactive in TNBC, promoting the transcription of genes associated with cell survival and proliferation and inhibiting the pro-apoptotic protein Noxa. Noxa displaces Bcl-2 family proteins, which are overexpressed in TNBC, from mitochondria-bound Bax to promote apoptosis. Bcl-2 and Notch expression are also regulated by miR-34a signaling, which is reduced in TNBC, thus contributing to disease progression.

### 1.3.1 Notch Signaling in Triple-Negative Breast Cancer

Hanahan and Weinberg first proposed the “hallmarks” of cancer in 2000 and have expanded upon them in recent years to include ten major characteristics of cancer cells and their microenvironment that promote disease progression, many of which are directly influenced by developmental signaling pathways. [26, 28] The developmental Wnt, Hedgehog, and Notch signaling pathways guide early development through precise control of cell proliferation, differentiation, migration, and cell-to-cell communication, [29, 30] and they also preserve tissue function by regulating adult

stem cell populations [31]. Given the important and complex role these pathways play in controlling cellular function, it is unsurprising that their aberrant expression has been associated with the formation and progression of cancer [32–35] by supporting cancer cells' ability to grow, resist treatment, metastasize, and recur [26, 28, 36]. Indeed, overactive developmental signaling facilitates cancer cells' evasion of growth suppressors and the immune system, and supports the formation of new blood vessels to increase nutrient supply, contributing to unchecked disease progression. [26, 28] Additionally, the Wnt, Hedgehog, and Notch signaling pathways have a significant impact on cancer stem cell populations [37–41], which facilitates disease recurrence if tumors are not fully removed [40, 42, 43]. Overall, the integral role that Wnt, Hedgehog, and Notch signaling play in cancer progression (**Figure 1.2**) makes them extremely promising targets for new therapeutic strategies. While all three pathways are implicated in TNBC [44–46], this thesis investigates the use of nanoparticles as tools to regulate Notch signaling specifically. We demonstrate in Chapter 4 and 5 that by inhibiting Notch signaling using nanotherapeutics, TNBC progression may be dramatically slowed or even reversed.

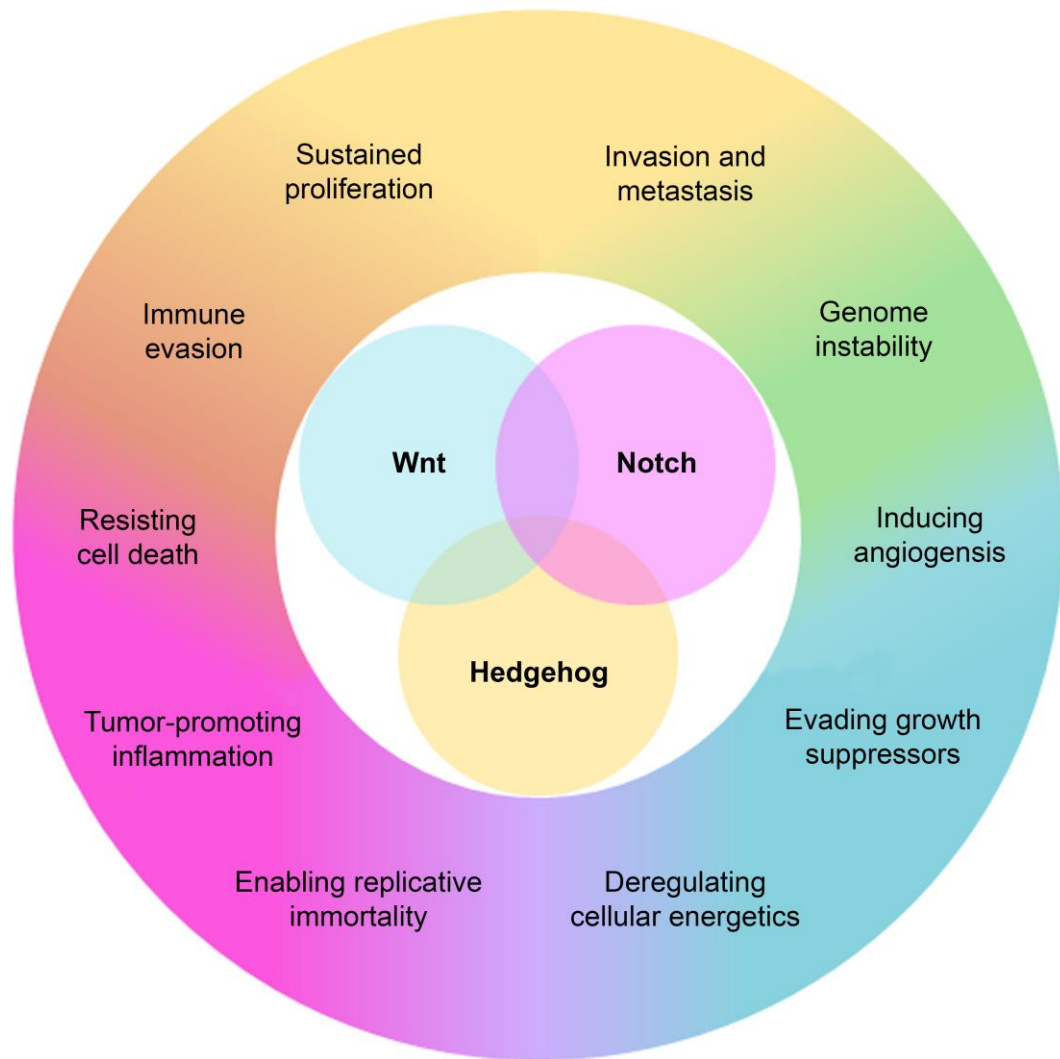


Figure 1.2: Dysregulation of the developmental Wnt, Notch, and Hedgehog signaling pathways is implicated in all of the “hallmarks” of cancer, and all three pathways are hyperactive in TNBC. Reproduced from Valcourt, *et al. Annals Biomed Eng.* 2019. [4]

As noted above, the Notch signaling pathway is frequently dysregulated in cancer. [47] Notch signaling is activated in cancer cells when one of four canonical ligands (Delta1, 3, or 4, or Jagged 1/2) on signal-sending cells bind the extracellular

region of Notch receptors 1-4 on signal-receiving cells. (**Figure 1.3**) [48] This initiates a downstream cascade of cleavages, first by ADAM family proteases that remove the extracellular portion of Notch receptors from their transmembrane domain, and subsequently by the gamma secretase complex that removes the intracellular portion of Notch receptors from the transmembrane domain. Ultimately, this cascade leads to the nuclear translocation of the Notch intracellular domain (NICD). [47] In the nucleus, NICD complexes with MAML1 and CSL to promote the transcription of genes associated with cell survival, proliferation, and stemness. In addition to this ligand dependent activity, the Notch signaling pathway can also undergo ligand independent activation that is mediated by ADAM17. [40]

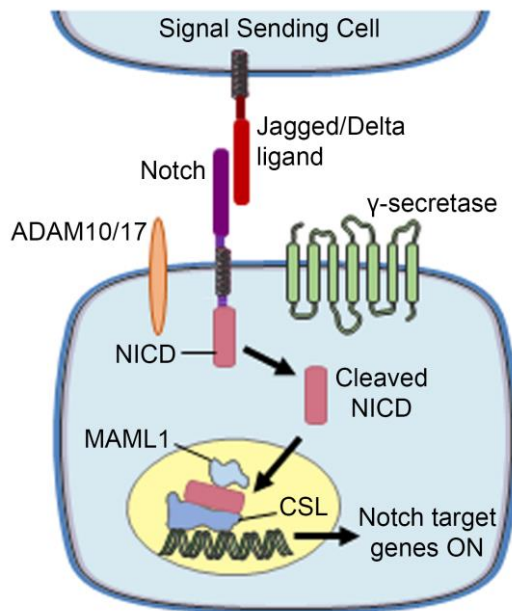


Figure 1.3: Canonical Notch signaling is activated when Jagged or Delta ligands on a signal-sending cell bind the extracellular domain of the Notch receptor on a signal-receiving cell. The extracellular domain of Notch is subsequently cleaved by ADAM family proteases, then the intracellular domain (NICD) is cleaved by the  $\gamma$ -secretase complex. Released NICD translocates to the nucleus, where it acts as a promoter for the transcription of downstream target genes that support cell survival, proliferation, stemness, and other oncogenic behaviors. Reproduced from Valcourt, DM, Dang MN, Scully MA, Day ES, manuscript in revision.

Depending on the type of cancer, different Notch receptors have varying levels of expression and prognostic implications. In certain cases, Notch can even serve as a tumor suppressor [49–51], but its overactivation is largely considered oncogenic [52]. While overexpression of Notch 2–4 has been implicated in a variety of cancers [52–55], Notch-1 in particular is frequently overexpressed in cancer and serves as a promising target for therapeutic manipulation. [40, 42, 48, 56, 57] In TNBC specifically, Speiser *et al* found elevated Notch-1 expression in 100% of cases. [54]

This overexpression in TNBC [54, 58] is associated with stem cell-like behavior, invasiveness, chemoresistance, and an overall poor prognosis [44, 59]. Patients with elevated Notch-1 signaling have a 42% 5-year survival rate, which compares to a 65% survival rate in patients with low Notch-1 levels. Chapters 4 and 5 of this thesis investigate the use of nanoparticles that exploit this overexpression of Notch-1 in TNBC to provide both targeted delivery of therapeutic cargo and suppression of Notch signaling.

### **1.3.2 The Role of p53 Apoptotic Signaling and Bcl-2 in Triple-Negative Breast Cancer**

Besides Notch signaling, several other signaling pathways are implicated in TNBC and often exhibit interplay with the Notch pathway to support tumorigenesis. One such critical pathway is the p53 apoptotic signaling pathway (simplified in **Figure 1.4**), which facilitates unchecked cell survival when dysregulated. [60, 61] Below we describe this pathway in detail, as Chapter 4 of this thesis introduces a strategy to manipulate p53 apoptotic signaling in combination with regulation of Notch signaling.

When healthy cells experience external stress or DNA damage, p53 signaling is activated (**Figure 1.4a**) and acetylated p53 migrates to the mitochondria, where it promotes Bax-mediated release of cytochrome c. [60] In the cytosol, cytochrome c activates caspases (cysteine proteases that cleave proteins after aspartic acid residues to produce morphological changes associated with apoptosis) by binding Apaf-1, creating an apoptosome. [62] The apoptosome subsequently recruits caspase-9, the initiator caspase, to the complex. This stimulates the autoactivation of procaspase-9

[63], which then initiates a downstream cascade of caspase activation that ultimately leads to apoptotic cell death [63–67].

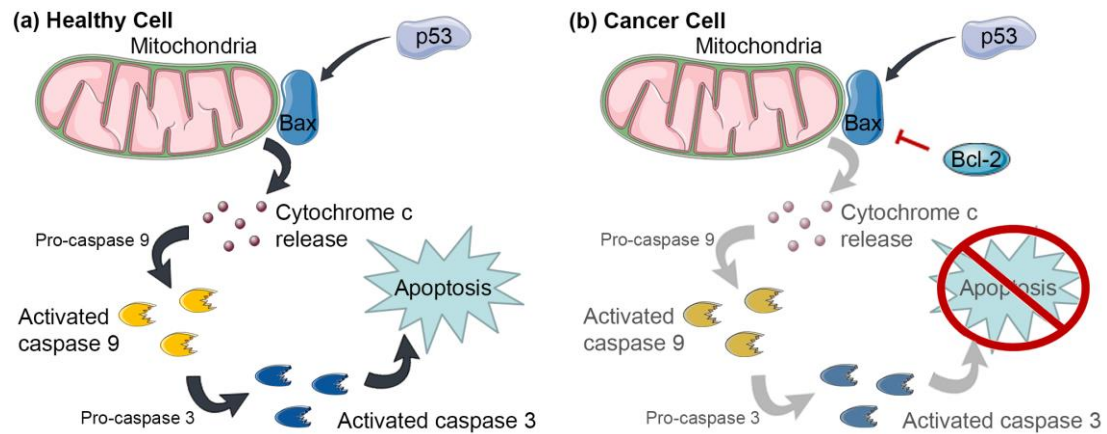


Figure 1.4: Simplified scheme of the p53 apoptotic signaling pathway in healthy cells versus TNBC cells. (a) Upon activation in healthy cells, acetylated p53 migrates to the mitochondria to induce Bax-mediated release of cytochrome c. There is a subsequent series of activation of caspases that ultimately leads to apoptosis. (b) In TNBC cells, Bcl-2 proteins are overexpressed, leading to inhibition of apoptotic signaling.

In TNBC cells, as well as many other cancer types, the p53 pathway is dysregulated, making the cells less prone to undergo apoptosis when exposed to external insults. Many molecules interact with the p53 apoptotic pathway in a regulatory capacity, but proteins belonging to the B-cell lymphoma 2 (Bcl-2) family are among those most heavily studied for their role in suppressing apoptosis. This family of proteins is divided by structure and function into three groups: Bcl-2 homology 3 (BH3) proteins (Bid, Bim, Noxa, Puma, etc.) that actively activate apoptosis, executioner proteins (Bax, Bak, Bok) that permeabilize the mitochondrial outer membrane to activate effector caspases, and apoptosis-suppressing proteins (Bcl-

2, Bcl-X<sub>L</sub>, Bcl-W, Mcl-1, Bfl-1/A1) that inhibit BH3 and executioner proteins. [68–70] In TNBC, the anti-apoptotic protein Bcl-2 is particularly overexpressed compared to healthy cells. [71, 72] Overexpressed Bcl-2 sequesters Bax-mediated permeabilization of the mitochondrial outer membrane, preventing the release of cytochrome c. **(Figure 1.4b)** Without subsequent activation of effector caspases by the cytochrome c/Apaf-1 complex, TNBC cells fail to react to external stress or DNA damage, thus promoting disease progression. The significant role Bcl-2 plays in regulating apoptosis and its aberrant expression in TNBC make it a promising target for novel therapeutic strategies. [73] Chapter 4 of this dissertation develops a nanotherapeutic strategy that manipulates Bcl-2 family proteins in combination with Notch signaling inhibition, which exhibits remarkable potency against TNBC.

### **1.3.3 The Role of miR-34a in TNBC and its Interplay with p53 Apoptotic Signaling**

In addition to Bcl-2 family proteins, microRNAs (miRNAs) can also interact with the p53 apoptotic pathway in a regulatory capacity. miRNAs are small, non-coding RNA molecules that regulate the expression of networks of genes. [74–76] The biogenesis of the majority of miRNAs **(Figure 1.5)** begins in the nucleus. miRNAs are initially transcribed by RNA polymerase II, producing primary miRNAs (pri-miRNAs) that have an internal hairpin within their larger structure. [77] These pri-miRNAs are cleaved by Drosha to remove each end, creating about 70 base pair (bp) long preliminary miRNAs (pre-miRNAs) with an imperfect stem-loop structure that are then exported from the nucleus into the cytoplasm by an exportin 5/RanGTP complex. [78, 79] Once pre-miRNAs reach the cytoplasm, the RNase III endonuclease Dicer removes their terminal loop, resulting in mature double-stranded miRNA

duplexes that are approximately 22 bp long. [78, 80] After generation, one strand of the mature miRNA duplex, known as the guide strand or miRNA strand, is incorporated into the miRNA-induced silencing complex (miRISC), which contains Argonaute proteins and is also known as the miRNA-containing ribonucleoprotein complex. The other strand, known as the passenger strand or miRNA\* strand, is typically degraded, although there are instances where the miRNA\* strand is loaded into miRISC to facilitate gene silencing. [81] Once the mature miRNA is loaded into miRISC, it guides the complex to its cognate messenger RNA (mRNA) either with perfect complementarity or with imperfect base pairing. This results in either degradation or translational repression of the targeted mRNA, which thereby inhibits production of the encoded protein.

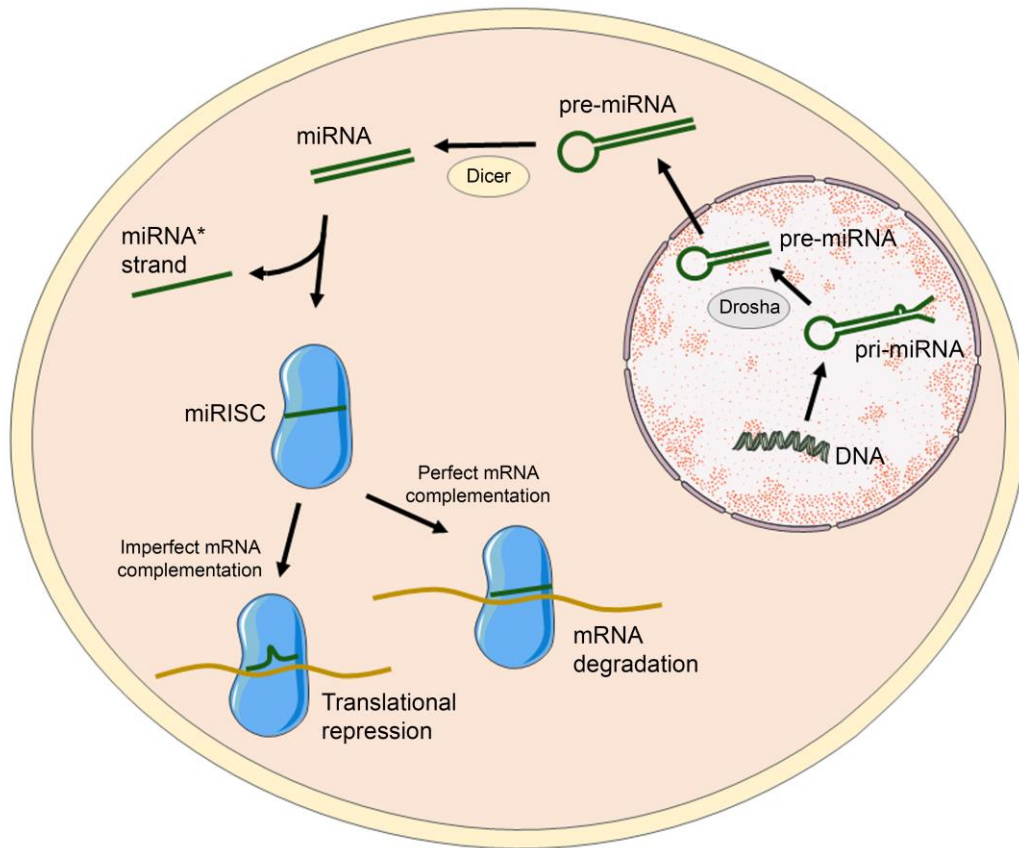


Figure 1.5: Scheme of miRNA biogenesis and mechanism of gene regulation. miRNAs are transcribed as pri-miRNAs in the nucleus, which are subsequently cleaved by Drosha to form pre-miRNAs. pre-miRNAs are then transported to the cytoplasm by exportin proteins. Cytoplasmic pre-miRNAs with unstable stem-loop structures are further cleaved by Dicer into small duplex RNA structures (miRNA:miRNA\*) that contain both mature miRNA and its complementary strand (miRNA\*). The miRNA\* strand is typically degraded, and the mature miRNA strand assembles into RISC and guides it to specific messenger RNAs (mRNAs) to induce gene silencing. Reproduced from Kapadia, *et al. J Appl Polym Sci.* 2019. [5]

The interaction between the p53 apoptotic pathway and miRNA processing is critical for promoting proper cellular function. When cells experience DNA damage, p53 facilitates the post-transcriptional maturation of miRNAs associated with growth

suppression by interacting with Drosha to enhance the processing of pri-miRNAs into pre-miRNAs. [82] Hermeking has investigated this process for the miR-34 family, in particular. **(Figure 1.6)** [83, 84] Downstream of p53 activation, pri-miR-34 is processed into mature miR-34 capable of regulating a variety of genes, including Bcl-2 and cyclin D1. By suppressing the expression of these genes, miR-34 can induce apoptosis, senescence, and G1 cell cycle arrest and reduce proliferation and migration. [84] Unfortunately, miR-34 expression is reduced in a number of cancers [85–88], and in TNBC, this downregulation is associated with reduced survival and an overall poor prognosis [84, 89]. Several studies have shown that miR-34a specifically interferes with cellular proliferation [90], migration [89], chemosensitivity [91, 92], and invasion [93]. Thus, restoring the normal expression of tumor-suppressive miR-34a through a process known as miRNA replacement therapy is a promising treatment strategy for TNBC and other cancers characterized by loss of miR-34a expression. Chapter 5 of this dissertation introduces nanoparticles that can delivery miR-34a into TNBC cells by exploiting their overexpression of Notch-1 receptors.

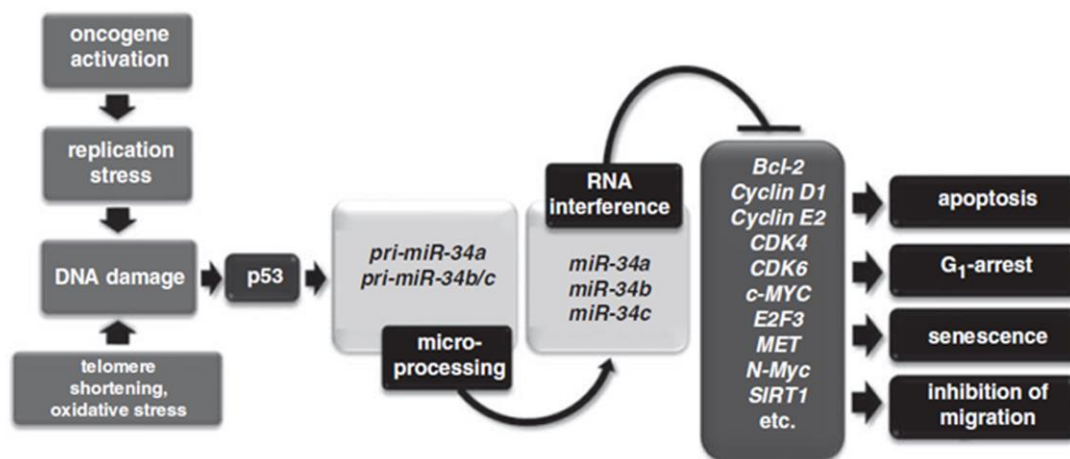


Figure 1.6: Upon activation of p53, miR-34a is processed and regulates gene expression to induce apoptosis, cell cycle arrest, and senescence, and inhibit cell migration. Reproduced from Hermeking, H. *Cell Death and Differentiation*. 2010. [84]

### 1.3.4 The Need for Delivery Technologies to Manipulate TNBC Biology

The preceding sections have introduced some of the key biological characteristics that drive TNBC progression. However, therapeutic manipulation of these features has remained an elusive goal. The following section introduces the use of nanoparticles as tools to deliver therapeutic cargo specifically to cancer cells. It provides an overview of various types of cancer nanomedicine and introduces how this thesis builds upon the state of the art in the field.

## 1.4 Nanotechnology in Cancer Treatment

The clinical application of free therapeutic agents, including antibodies, small molecule drugs, and RNA therapeutics, is frequently plagued by poor pharmacokinetics and biodistribution profiles. To improve the efficacy and safety of these therapies, researchers have developed nanoparticle-based medicines that can enhance tumor-specific delivery of their cargo. The concept of nanoparticles was

originally inspired by Paul Ehrlich who called his idea for a new delivery system “Zauberkekeln”, which translates to “Magic Bullets” in English. [94] Utilizing nanoparticles for cancer therapy dates back to the late 1970s and early 1980s, and their use quickly garnered interest after demonstrations of enhanced efficacy and reduced adverse effects. [95–101] These highly tunable systems can encapsulate therapeutic molecules or present them on their surface, and they can exploit the leaky vasculature associated with tumors to facilitate passive accumulation within the tumor microenvironment. (**Figure 1.7**) [102–104] Additionally, the surface of nanoparticles may be modified with “targeting” agents such as antibodies, peptides, or other small molecules, to facilitate cancer cell-specific binding and uptake once they have passively accumulated in the tumor. This section introduces the three major classes of cancer nanomedicine, each of which are explored and developed further in Chapters 3-5 of this dissertation: light-activated nanoparticles for phototherapy, nanocarriers for drug delivery, and nanotherapeutics for gene regulation.

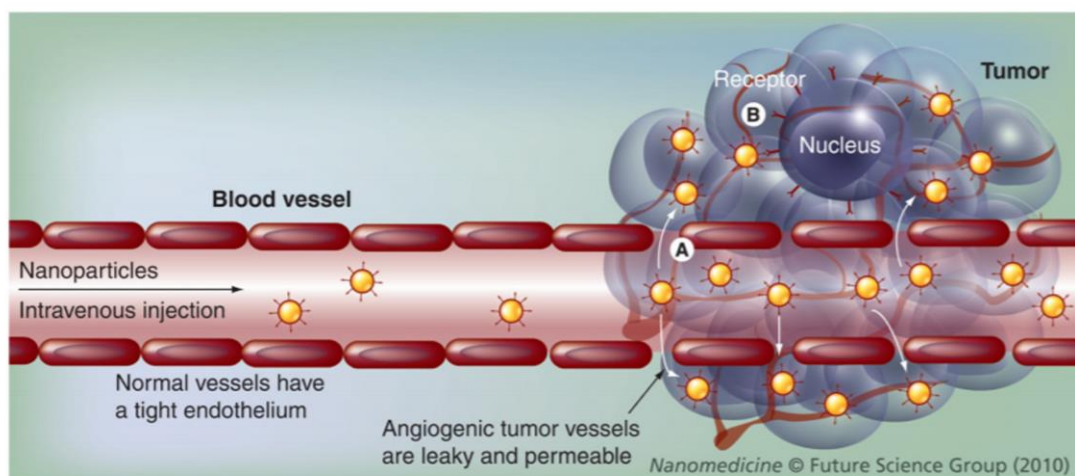


Figure 1.7: Scheme depicting how nanoparticles enhance drug delivery to solid tumors. After intravenous injection, nanoparticles passively accumulate in tumors (A) through leaky vasculature. Surface functionalized nanoparticles then enable active targeting (B) by binding to cell receptors. Reproduced from Dong. *Nanomed.* 2010. [104]

#### 1.4.1 Photoresponsive Nanomedicines

The two main classes of light-activated, or photoresponsive, nanoparticle-mediated therapy are photothermal therapy (PTT) and photodynamic therapy. In these therapies, administered nanoparticles are excited by externally applied light to induce cell death through the production of heat or reactive oxygen species, respectively.

[105] These are considered precision therapies that enable spatiotemporal control of the treatment, as the therapeutic effect should be achieved only when and where both the nanoparticles and light are applied. Accordingly, off-target effects of these therapies are extremely low. Chapter 3 of this thesis describes the development of a new nanoparticle to mediate PTT, and therefore this section introduces PTT in detail.

As noted above, PTT utilizes nanoparticles embedded in tumors as exogenous energy absorbers to convert externally applied near-infrared (NIR) light into heat to

ablate cancer cells (**Figure 1.8**), and it has shown much promise as a novel cancer treatment strategy. [106–108] Indeed, PTT mediated by silica core/gold shell “nanoshells” has recently been evaluated in human patients with promising results. [109, 110]

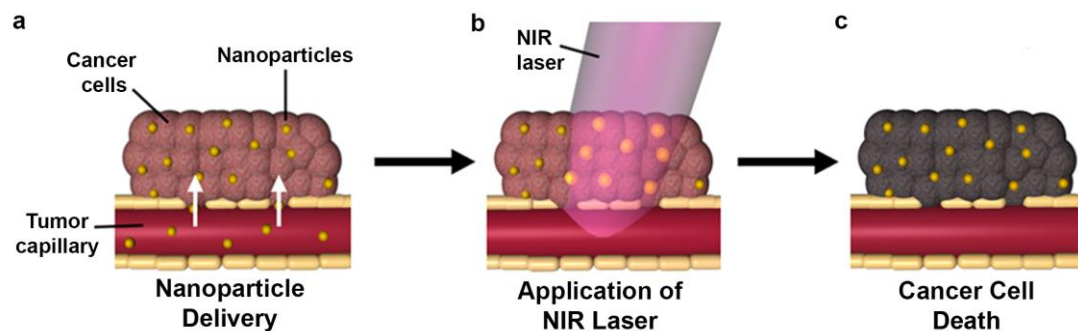


Figure 1.8: Schematic of nanoparticle-mediated photothermal therapy. In nanoparticle-mediated photothermal therapy, (a) nanoparticles first accumulate in the tumor through leaky vasculature. (b) When these nanoparticles are irradiated with near-infrared (NIR) light, they convert the light into heat. (c) The heat shock induced by this irradiation then leads to tumor cell death. Modified from Riley, R.S. *WIREs*. 2017. [108]

The use of nanoparticles such as nanoshells that respond to NIR light is important for PTT because NIR light can penetrate deeper into tissue than visible wavelengths of light. This is because NIR light is minimally absorbed by the major components of tissue it will encounter prior to reaching the diseased site. (**Figure 1.9**) [111] Thus, NIR light can facilitate treatment in tumors further under the surface of the skin while leaving healthy tissue unharmed. The key advantages of PTT over conventional treatment strategies are that it is simple to perform, it is tumor-specific,

and it is less susceptible to cellular resistance because it induces cell death through physical mechanisms such as membrane rupture and protein denaturation. [112]

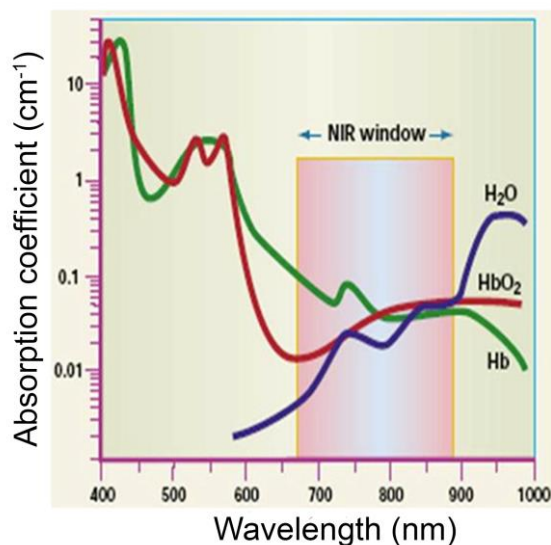


Figure 1.9: The absorption of light by the major components of tissue: water, hemoglobin, and oxyhemoglobin. The near-infrared (NIR) window represents the region of wavelengths of light that is minimally absorbed by these components. Adapted from Weissleder. *Nat Biotechnol.* 2001. [111]

Historically, most PTT strategies have used nanoparticles based on gold because they offer high photothermal conversion efficiencies as well as ease of synthesis and surface modification [108, 113–116]. Nanoshells, in particular, have progressed into clinical trials to mediate PTT of head and neck tumors and prostate tumors. [110, 117, 118] However, these and other gold-based nanoparticles will remain in the body for extended periods of time with unknown long-term health effects. [108] To prevent possible undesired side effects associated with non-

degradable nanoparticles, researchers have begun to develop organic photothermal agents. [119] By incorporating NIR-absorbing dyes into biodegradable platforms, these nanoparticles can facilitate photothermal ablation of tumors, while also providing dual-imaging capabilities. [120–128] Chapter 3 of this dissertation develops one such organic photothermal agent for the treatment of TNBC, and demonstrates it is effective both *in vitro* and *in vivo*.

#### **1.4.2 Nanotechnology to Enable Drug and Antibody Delivery**

While PTT can be applied to kill TNBC cells, it will be limited to the treatment of tumors located in regions where NIR light can penetrate. A more widely applicable strategy would be to directly regulate aberrantly expressed signaling pathways, such as the p53 apoptotic pathway described previously, through nanoparticle-mediated delivery of small molecule agents that re-establish programmed cell death signaling in TNBC cells. There are three main classes of agents that can be used to regulate aberrantly expressed signaling pathways in cancer: antibodies, small molecules, and nucleic acids. This dissertation explores all three of these agents. Specifically, in Chapters 4 and 5, nanoparticles that co-deliver antibodies along with either small molecule drugs or miRNA therapeutics are examined. Here, we introduce the use of nanoparticles as vehicles for small molecule and antibody delivery. Then, in the following section, we introduce the use of nanoparticles for nucleic acid delivery.

Small molecule inhibitors of various oncogenic signaling pathways have been widely explored. However, they often encounter issues with solubility, bioavailability, targeted cellular uptake, and systemic toxicity that hinder their clinical translation. [129] Encapsulating these molecules inside nanoparticles or loading them on nanoparticles' exterior can improve their stability, pharmacokinetics, biodistribution,

and tissue/cell-specific delivery. This enables the nanoformulations to be much more effective than their freely delivered counterparts. [6, 130–132] To achieve effective drug delivery, there are many nanoparticle design parameters to consider, including size, shape, and surface coating. With respect to size, nanoparticles with diameters less than ~5 nm rapidly undergo renal clearance upon intravenous administration and those with diameters greater than ~200 nm exhibit splenic filtration due to the 200-500 nm size range of inter-endothelial cell slits. [133] Accordingly, nanoparticle-based drug delivery vehicles should be designed with a diameter between 5 and 200 nm. Generally, nanoparticles with diameters less than 100 nm are the longest circulating and they also achieve the greatest tissue/cell uptake. [133, 134]

In addition to size, surface charge and surface chemistry also play a significant role in nanomaterial circulation time and cellular entry and should thus be considered when designing nanotherapeutics. Since cells have negatively charged membranes, they can internalize positively charged nanomaterials more readily than negatively charged or neutral materials due to electrostatic interactions. However, when injected in the bloodstream, positively charged nanoparticles are cleared more rapidly than negative or neutral particles and can induce hemolysis and platelet aggregation. [135] Within the bloodstream, all nanoparticles, regardless of charge, are masked by a biological corona (mainly consisting of opsonin proteins) that leads to their sequestration by the mononuclear phagocytic systems (MPS), reducing their distribution half-life. [135, 136] The rapid clearance of positively charged nanoparticles is likely a consequence of the fact that the initial surface charge of a nanoparticle will dictate the specific makeup of the protein corona that forms on its

surface, giving it a new “biological identity” that ultimately dictates pharmacokinetics and biodistribution. [136]

One strategy to minimize protein corona formation is to passivate the nanoparticle surface with poly(ethylene glycol) (PEG) polymer chains containing a methoxy end group. This provides a “stealth effect” in which a water hydration layer surrounds the nanoparticle to prevent opsonization and sequestration by the MPS. For example, adding PEG to liposomal doxorubicin increased its half-life from minutes to hours. [137] While there are numerous examples of PEGylation being used to enhance nanoparticle circulation and target delivery, there are also some limitations to PEGylation. [138, 139] For example, PEGylation can lead to an immune response, as up to 70% of people have anti-PEG antibodies existing in their body. [140] Additionally, PEGylation can limit the cellular uptake of nanoparticles. This can be overcome by simultaneously decorating nanoparticles with ligands designed to bind specific receptors that are overexpressed on the surface of the target cells in order to facilitate receptor-mediated endocytosis. [141, 142] We recently reviewed the different types of targeting strategies that are utilized in nanomedicine [6] and note that there is currently substantial debate regarding the benefits of targeting agents. For targeting agents to effectively mediate cell-specific binding and internalization, the nanoparticles must first reach the diseased tissue, penetrate through the tissue to interact with the desired cells, and then engage the targeted receptors. This requires the protein corona formed around the nanoparticle to not limit the effectiveness of the targeting agent, which is difficult to achieve. Recent meta-analyses and experimental studies have emphasized this point by showing that targeting agents only modestly improve the percentage of nanoparticles that reach their target cells. [143, 144] These

findings, and the challenges associated with the PEG immune response, have led researchers to begin exploring alternative strategies to enhance nanoparticle delivery to target cells, such as designing nanoparticles to mimic cells within the body to hide them from the immune system and increase target delivery. [6, 145–147]

In this thesis, we explore the use of antibody modification of nanoparticles for the dual purpose of achieving TNBC cell-specific binding and inhibiting oncogenic signaling. Antibodies were among the first biomolecules explored as targeting agents for nanotherapies [148, 149], and are considered beneficial targeting moieties because they have high specificity for their target, their production is well-established, and they can easily be exchanged to target a variety of different cell surface proteins important for disease progression. [141] Additionally, the bioconjugation of antibodies to nanoparticles typically involves simple chemical reactions. Chapter 2 of this dissertation further details antibody conjugation to polymer nanoparticles using 1-ethyl-3-(3-dimethylaminopropyl)carbodiimide (EDC) chemistry [150], which forms an amide bond between exposed carboxylic acid functional groups on the surface of the nanoparticle and amine functional groups on the conserved fragment of the antibody. Importantly, directionality of the antibody may play a role in its binding affinity, as the antigen-binding sites need to be accessible for efficient targeting. [151, 152] With EDC chemistry, antibodies are randomly oriented, which reduces selective binding efficiency, may have low coupling efficiency, and can result in nanoparticle aggregation. [153] With directional conjugation methods, antibodies are directly linked to the nanoparticle by the conserved fragment of the antibody, leaving the antigen-binding region unhindered. [151, 154] With these strategies, fewer antibodies

are needed per nanoparticle to achieve the same targeting effect, thus reducing cost and enhancing performance. [152, 154]

Perhaps one of the most exciting features of antibodies (which we exploit in this thesis) is that, in addition to providing cell-specific binding, they can also confer a therapeutic benefit on the nanoparticles. This is because, upon binding to their targeted receptor, antibodies (and antibody-nanoparticle conjugates) can competitively block signaling ligands from binding the receptor, leading to inhibition of the downstream signaling pathway. (**Figure 1.10**) [155, 156] A major benefit of utilizing antibody-nanoparticle conjugates over freely delivered antibodies to elicit such signal cascade interference is that antibody-nanoparticle conjugates demonstrate multivalency, in which they have increased binding affinity for their target compared to free antibodies. [142, 155, 157] We and others have shown that this increased valency correlates with enhanced signal cascade interference. [155, 158] Antibody-nanoparticle conjugates that continue to explore the benefits of combining multivalent targeting and signal cascade interference with the ability to specifically deliver a payload may be highly suited for the safe and effective treatment of a variety of cancers. Chapters 4 and 5 of this dissertation directly investigate this concept by using antibody-modified nanoparticles to deliver small molecule therapeutics and tumor suppressive miRNAs to TNBC, respectively.

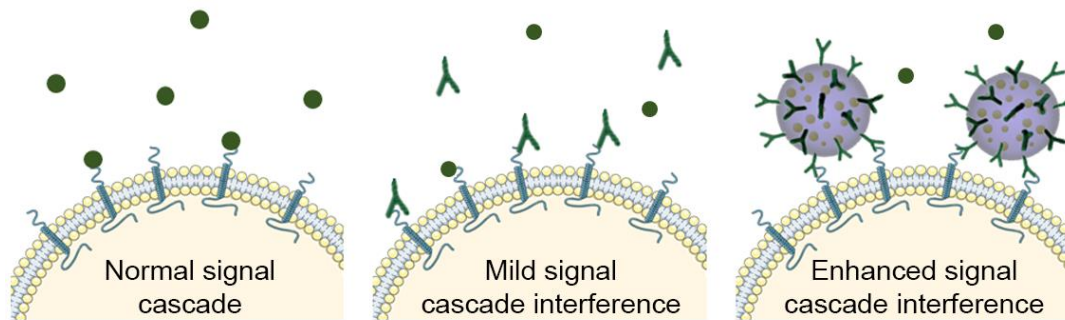


Figure 1.10: In cancer cells, ligand/receptor interactions activate downstream oncogenic signaling. Antibodies can reduce signaling by competitively blocking signaling ligands from binding the receptor and locking the receptor in a non-responsive state. Antibody-nanoparticle conjugates can enhance signaling cascade interference by engaging multiple receptors simultaneously. Modified from Valcourt, D.M. *Annals Biomed Eng.* 2019. [4]

### 1.4.3 Nanotechnology for Nucleic Acid Delivery

Besides facilitating delivery of small molecules and antibodies, nanoparticles can also be used to enhance nucleic acid delivery to cancer cells. The use of small interfering RNA (siRNA) or miRNA molecules to suppress desired targets in cancer through RNA interference has received substantial attention lately as a promising alternative treatment strategy that may enable reduction of cancer cell survival, proliferation, and stemness. However, the clinical translation of RNA therapeutics is limited due to their susceptibility to nuclease degradation, rapid clearance from the bloodstream, their inability to passively enter cells, and their activation of the innate immune system causing undesirable immunological side effects. [159–162] Thus, to facilitate successful gene regulation, systemically administered RNA molecules and their carriers must overcome these many physiological barriers. (**Figure 1.11**) [5]

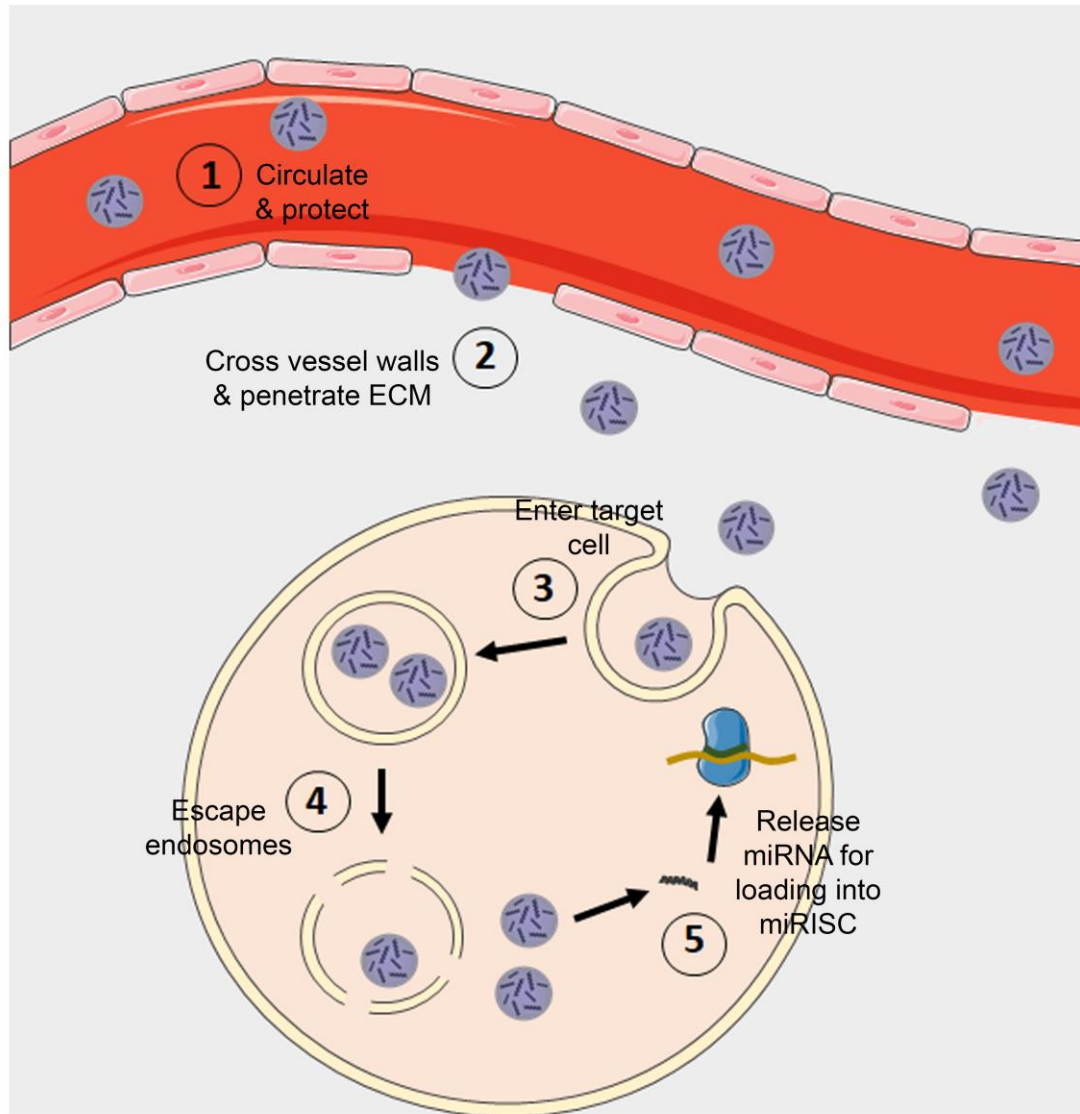


Figure 1.11: Scheme depicting the biological barriers that miRNA nanocarriers must overcome. To enable gene regulation, miRNA nanocarriers must: (1) prevent miRNA degradation from serum nucleases and provide long circulation in the blood, (2) cross vessel walls and penetrate through the extracellular matrix (ECM), (3) enter target cells, (4) facilitate endolysosomal escape, and (5) release miRNA in the cytoplasm for loading into the RNA-induced silencing complex (RISC) for subsequent gene regulation. Reproduced from Kapadia, *et al. J Appl Polym Sci.* 2019. [5]

Historically, chemical modifications have been used to increase the stability and limit the immunogenicity of RNA therapeutics. [163] Phosphorothioate modification of the RNA backbone, which substitutes a sulfur atom for an oxygen atom, reduces the ability of nucleases to degrade this bond. [163] Likewise, replacing the 2'-OH with 2'-*O*-methyl, 2'-*O*-methoxyethyl, or 2'-fluoro groups can increase binding affinity to target mRNA [164], enhance nuclease stability [165], and extend serum stability [166]. However, chemical modifications can also reduce the specificity and functionality of RNA therapeutics, and such alterations typically do not improve penetration across biological barriers. [165] Therefore, there is a need to develop innovative delivery vehicles that can protect RNA therapeutics from degradation and deliver them to target cells to induce robust gene regulation. Nanoparticles have shown great promise in meeting this need, as they are ideally suited to protect RNA from degradation, extend circulation half-life, facilitate cellular entry, and increase therapeutic index. [167] Indeed, various nanoparticle delivery systems have shown considerable promise for the delivery of plasmid DNAs, antisense oligonucleotides, siRNAs, and miRNAs to diseased cells *in vitro* and *in vivo*. [160, 168–181]

Perhaps one of the biggest challenges in developing RNA nanocarriers is ensuring the cargo reaches the cytosol of the target cell after internalization, so that it can engage RISC to induce gene silencing. Cells can take up nanoparticles through either receptor-mediated or nonreceptor-mediated endocytosis, and the specific mechanism is influenced by both nanoparticle size and surface functionality. The mechanism of uptake is critical since it dictates the microenvironment the particles will ultimately face after internalization. If nanoparticles are internalized by clathrin-mediated endocytosis, the classic method of uptake, they will be routed to endosomes

and then to lysosomes, where the harsh acidic and enzyme-rich environment will degrade nucleic acid cargo. [133, 134, 167] Alternatively, if nanoparticles are internalized by caveolin-mediated endocytosis, they will be trafficked to neutral caveosomes and bypass the acidic lysosomal environment. [133, 134, 167] The ultimate fate of nanomaterials in caveosomes is still being explored, but some evidence suggests caveosomes route their cargo to the endoplasmic reticulum and the cytoplasm. [182].

Since clathrin-mediated uptake is the primary method by which nanoparticles enter cells, an extraordinary amount of research has explored ways to enable endolysosomal escape of particles prior to lysosomal fusion. [183–185] Studies have shown that materials with a high buffering capacity (such as polyethyleneimine) can be incorporated into nanoparticles to induce swelling and rupture of endosomes. This is often attributed to the “proton sponge effect”, wherein proton absorption by the material leads to an influx of water and rupture of the endosomal compartment, but recent studies have called into question the accuracy of this proposed phenomenon. [186, 187] An alternative strategy is to coat RNA carriers with fusogenic peptides, lipids, or membrane-destabilizing peptides. [133] Finally, cationic polymers can be incorporated into nanoparticles to mediate endosome escape by causing the positive surface of the nanoparticle to interact with the negative outer surface of the endosome, leading to membrane flipping and cargo release via the “flip-flop” mechanism. [188, 189]

In Chapter 5 of this thesis, we use antibody-modified nanoparticles to facilitate RNA delivery to TNBC cells. These nanoparticles, and all the nanoparticles described in this thesis, are based on poly(lactic-co-glycolic acid) (PLGA) structures. In the

following section of this chapter, we describe the characteristics of PLGA that make it well-suited as a therapeutic delivery vehicle.

### 1.5 Poly(Lactic Co-Glycolic Acid) Nanoparticles in Cancer Therapy

To facilitate the delivery of photothermal and gene regulatory agents like those introduced in this chapter, we have utilized the versatile and commercially available polymer poly(lactic co-glycolic acid) (PLGA) in each of the nanoparticle formulations described in Chapters 3-5. PLGA is an FDA-approved polymer that has been extensively investigated for drug delivery applications and has demonstrated utility in delivering a wide variety of therapeutic agents, including chemotherapy, antibiotics, proteins, and more. [190] Its structure (**Figure 1.12**) contributes to its versatility, allowing researchers control over degradation, drug release, functionalization, and other important characteristics that contribute to the success of nanocarriers.

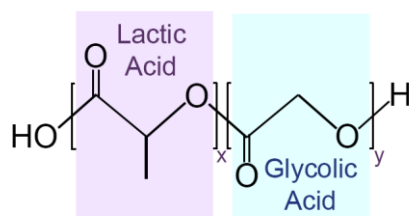


Figure 1.12: Chemical structure of poly(lactic co-glycolic acid).

The composition of PLGA (i.e. the ratio of lactic acid to glycolic acid and the overall molecular weight) has a significant impact on the degradation of the polymer and therefore the performance of the subsequently formed nanoparticles. PLGA is degraded through hydrolysis, which importantly creates the non-toxic products water

and carbon dioxide, which are easily eliminated from the body. [190] As the ratio of lactic acid to glycolic acid increases, PLGA becomes more hydrophobic, which slows the rate of degradation and thus drug release from nanoparticles. Additionally, higher molecular weight PLGA has a similar effect on the degradation and drug release rate, while further having a direct relationship to the size of the nanoparticles. Thus, nanoparticle characteristics including hydrophobicity, drug loading and release, and pharmacokinetic profile are all tunable by manipulating the ratio of lactic acid to glycolic acid and the overall molecular weight of the polymer. [190] In addition to the impact of composition on degradation of PLGA, the presence of both hydrophilic glycolic acid and hydrophobic lactic acid facilitates loading of a wide variety of cargoes using simple emulsion techniques and functionalization chemistries. [190] Chapter 2 introduces these methods, which are used throughout the remainder of this dissertation. Notably, in Chapters 3 and 4, hydrophobic cargoes are loaded within PLGA nanoparticles, while in Chapter 5, hydrophilic RNA cargoes are loaded in the nanoparticles, demonstrating the versatility of this material as a nanoparticle building block. Overall, this thesis utilizes this versatile platform to enable potent treatment of TNBC through three novel nanoparticle formulations.

## Chapter 2

### MATERIALS AND METHODS FOR NANOPARTICLE SYNTHESIS AND CHARACTERIZATION

Poly(lactic co-glycolic acid) (PLGA) nanoparticles are a versatile, biodegradable platform that can enable targeted delivery of hydrophobic or hydrophilic cargo to cancer. This chapter provides an overview of some of the common methods used throughout this dissertation to synthesize and characterize PLGA nanoparticles.

#### 2.1 Single Emulsion Solvent Evaporation Method for the Encapsulation of Hydrophobic Cargo

Hydrophobic cargo, like those presented in Chapters 3 and 4, is efficiently encapsulated in PLGA nanoparticles using a single emulsion (oil/water) solvent evaporation method. (**Figure 2.1**) The oil phase is composed of the desired cargo and PLGA dissolved in a volatile organic solvent (e.g. acetone). This solution is subsequently added to an aqueous phase, thus creating an emulsion in which the cargo is naturally encapsulated in the polymer matrix of the self-assembled nanoparticles. This mixture is then stirred to allow the solvent to evaporate and the nanoparticles are further purified to remove unencapsulated cargo. The single emulsion solvent evaporation method is described in further detail for the specific nanoparticle formulations presented in Chapters 3 and 4.

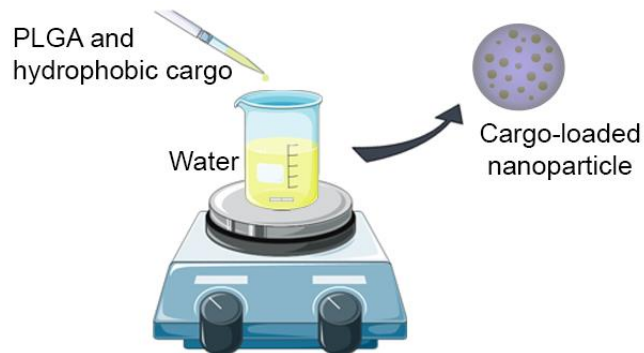


Figure 2.1: Single emulsion solvent evaporation method for encapsulation of hydrophobic cargo in poly(lactic go-glycolic acid) (PLGA) nanoparticles. Modified from Valcourt DM, Dang MN, Scully MA, Day ES, Manuscript in revision.

## 2.2 Double Emulsion Solvent Evaporation Method for Encapsulation of Hydrophilic Cargo

Hydrophilic cargo, such as the miRNA mimics presented in Chapter 5, is readily encapsulated in PLGA nanoparticles using a double emulsion (water/oil/water) solvent evaporation method. (**Figure 2.2**) The water 1 phase consists of the desired cargo and an excipient (e.g. polyvinyl alcohol (PVA)) dissolved in an aqueous phase. This solution is then added to the oil phase, which is composed of PLGA dissolved in a volatile organic solvent, to form the primary emulsion. Once homogenized, the primary emulsion is subsequently introduced to a second aqueous phase often containing a surfactant, thus forming a secondary emulsion. During the nanoparticle self-assembly process, the hydrophilic cargo is encapsulated in water pockets within the PLGA. This mixture is then stirred to allow the solvent to evaporate and the nanoparticles are further purified to remove unencapsulated cargo. The double emulsion solvent evaporation method for miRNA-loaded PLGA nanoparticles is described in further detail in Chapter 5.

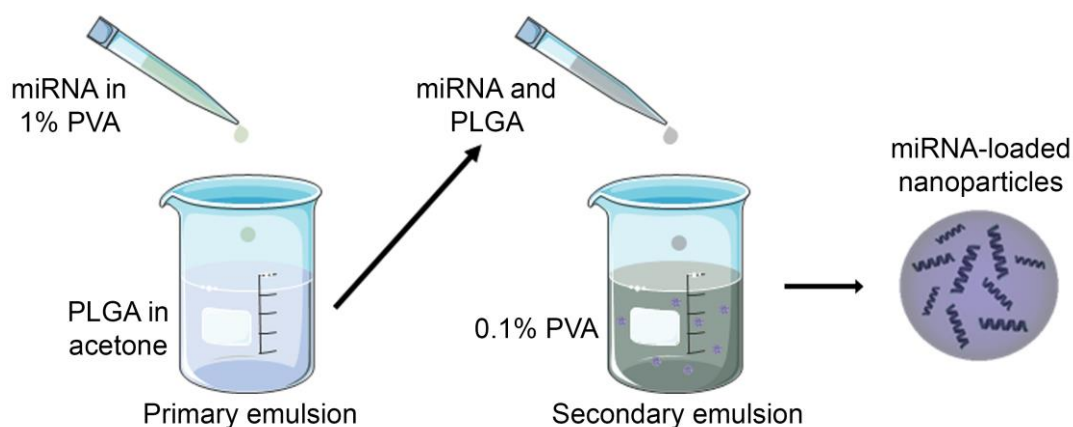


Figure 2.2: Double emulsion solvent evaporation method for encapsulation of hydrophilic cargo (e.g. miRNA) in poly(lactic co-glycolic acid) (PLGA) nanoparticles. Modified from Valcourt DM, Day ES, Manuscript in revision.

### 2.3 Antibody Functionalization of Nanoparticles

PLGA nanoparticles are an adaptable nanocarrier because they are easily functionalized with targeting modalities like antibodies. Upon synthesis through the methods described above, PLGA nanoparticles have exposed carboxylic acid functional groups on their surface. These groups can be activated using 1-ethyl-3-(3-dimethylaminopropyl)carbodiimide (EDC). (**Figure 2.3**) With the addition of n-hydroxysulfosuccinimide (sulfo-NHS), an amine-reactive sulfo-NHS ester is formed that, upon introduction to a primary amine like those on the conserved fragment of antibodies, will form an amide bond and a resulting stable antibody-nanoparticle conjugate.

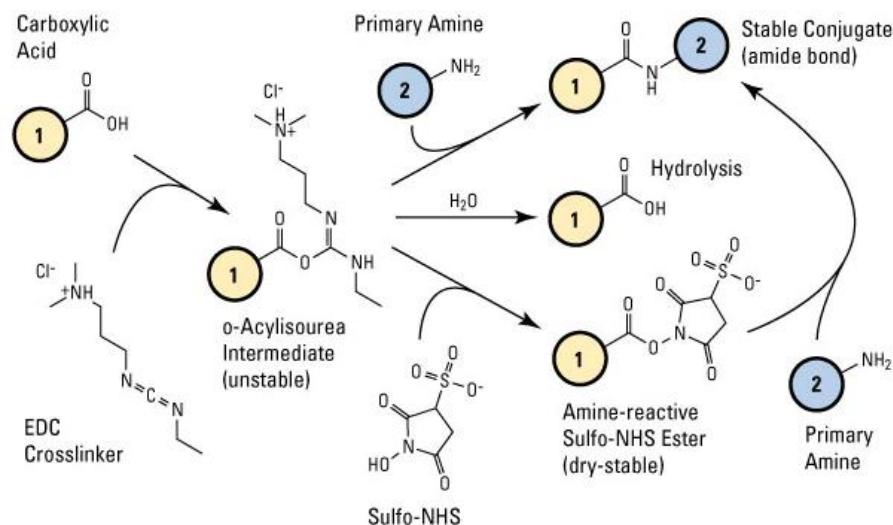


Figure 2.3: Crosslinking reaction scheme for antibody functionalization of poly(lactic co-glycolic acid) nanoparticles using 1-ethyl-3-(3-dimethylaminopropyl)carbodiimide (EDC) chemistry with the addition of n-hydroxysulfosuccinimide (sulfo-NHS). Taken from “Carbodiimide Crosslinker Chemistry”. *ThermoFisher Scientific*. [150]

## 2.4 Characterization Methods

The following methods are used to characterize nanoparticle size, morphology, and surface charge, and loading of hydrophobic and hydrophilic cargo and targeting moieties. Each method is introduced in brief and applied to specific nanoparticle formulations in Chapters 3-5.

### 2.4.1 UV-Visible Spectroscopy and Absorbance Readings

UV-visible spectroscopy and absorbance readings were used throughout this thesis to confirm encapsulation of hydrophobic cargo, quantify the loading of hydrophobic cargo and the concentration of the resulting nanoparticles, and to evaluate the stability of the encapsulated cargo. Loaded nanoparticles or

unencapsulated cargo were diluted in DI water or phosphate buffered saline (PBS) and analyzed using a spectrophotometer or plate reader.

#### **2.4.2 Dynamic Light Scattering and Zeta Potential**

Dynamic light scattering (DLS) and zeta potential measurements were used to quantify the hydrodynamic diameter and surface charge, respectively, of bare or antibody-functionalized nanoparticles throughout this thesis and provide evidence for successful surface functionalization. Nanoparticles suspended in solution are in a constant state of Brownian motion, the speed of which is dependent upon their size. This difference in speed thus causes various sizes of nanoparticles to scatter light differently. DLS measures the light scattered by the particles to calculate hydrodynamic diameter and the dispersity of the nanoparticles in solution.

While in suspension, nanoparticles are “coated” with a stationary layer of the medium in which they are suspended. This layer includes ions that create a difference in electrical potential between the mobile medium and the stationary layer. Zeta potential measurements quantify this difference in potential, resulting in a value indicating the surface charge of the nanoparticle. An increase in hydrodynamic diameter and more neutral surface charge were used to indicate successful antibody conjugation to the surface of PLGA nanoparticles in the formulations used throughout this dissertation.

#### **2.4.3 Electron Microscopy**

Transmission electron microscopy (TEM) was used to evaluate the morphology and dispersity of nanoparticles. Samples were prepared for imaging on 400 mesh carbon-coated copper grids that were rendered hydrophilic in a PELCO

easiGlow glow discharge unit. The freshly glow discharged grids were floated on drops of the sample for several seconds, washed with nanopure water, and negative stained with 2% uranyl acetate. After drying, the grids were imaged on a Zeiss LIBRA 120 TEM operating at 120 kV.

#### **2.4.4 Quantification of miRNA Loading in Nanoparticles**

The loading of miRNA in PLGA nanoparticles (presented in Chapter 5) was determined using a Quant-iT OliGreen assay on unencapsulated miRNA. Filtrates were collected during nanoparticle synthesis and concentrated prior to incubation with components of the OliGreen kit. The fluorescence intensity was compared to that of a standard curve to determine the nmol of miRNA encapsulated per mg of PLGA.

#### **2.4.5 Quantification of Antibody Loading onto Nanoparticles**

Antibody loading on the surface of PLGA nanoparticles was evaluated using a solution-based enzyme-linked immunosorbent assay (ELISA) modified from a previously published protocol. [191] Bare or functionalized nanoparticles were incubated with secondary antibodies conjugated with horseradish peroxidase (HRP). After removing unbound secondary antibodies, the samples were diluted in PBS and developed in 3,3',5,5'-tetramethylbenzidine (TMB) solution. The absorbance was then compared to that of a standard curve of known HRP-IgG concentration to calculate the quantity of antibodies conjugated per mg of PLGA.

### **2.5 Conclusions**

The methods described in this chapter provide an overview of the synthesis and characterization of single and double emulsion PLGA nanoparticles and functionalization of these nanoparticles with antibodies. These methods were used

throughout this dissertation to prepare nanoparticles and determine doses used in all experiments.

## Chapter 3

### DELIVERY OF IR820 DYE FOR PHOTOTHERMAL THERAPY

The work presented in this chapter is adapted from Valcourt, *et al.* *JBMRA* (2019); 107(8): 1702-1712. [192]

#### 3.1 Introduction

Triple-negative breast cancer (TNBC) accounts for 15-25% of all breast cancer cases and it lacks expression of the three most common receptors found on other subtypes of breast cancer: estrogen receptor, progesterone receptor, and human epidermal growth factor receptor 2. [8, 193] This lack of expression makes TNBC unsusceptible to current targeted or hormonal therapies and results in high recurrence and mortality rates. [8, 9, 193] Several alternative treatment strategies have shown promise against TNBC, including photothermal therapy (PTT), [194–197] which utilizes nanoparticles (NPs) embedded in tumors as exogenous energy absorbers to convert externally applied near-infrared (NIR) light into heat to ablate cancer cells. [106–108] In NP-mediated PTT, NPs delivered systemically accumulate in tumors through their leaky vasculature, [103, 198] and are then irradiated with NIR light, which causes them to produce heat sufficient to induce tumor cell death. [108, 199] The use of NIR light is important for PTT because NIR light can penetrate deeper into tissue than visible wavelengths since it is minimally absorbed by the major components of tissue it will encounter prior to reaching the diseased site. [107, 108, 200–202] The key advantages of PTT are that it is simple to perform, it enables high

precision since heat is generated only where NPs and light are combined, and it is less susceptible to cellular resistance because it induces cell death through physical mechanisms such as membrane rupture and protein denaturation. [108] Additionally, the mechanism of cell death can be tuned between apoptosis and necrosis by controlling treatment parameters such as the type of NP used and the irradiation conditions. [106] This is elaborated upon below and is important since the mechanism of cell death can influence overall treatment success when PTT is applied alone or in combination settings. In this chapter, we aimed to develop biodegradable, polymeric NPs to mediate pro-apoptotic PTT of TNBC as a standalone therapy.

As just introduced, the mechanism of cell death induced by PTT plays a critical role in treatment success. Typically, PTT has been applied in a manner that yields rapid and very high heating that causes cellular necrosis. However, when cells undergo necrosis, there is a pro-inflammatory response that can elicit a negative immune reaction, which may actually promote tumor recurrence. [106, 112, 203] It is critical to produce immunogenic cell death, which is largely temperature-dependent, to achieve long-term survival. [204] Thus, applying mild hyperthermia to induce apoptosis rather than necrosis may be preferable when PTT is applied as a standalone therapy because apoptosis is anti-inflammatory and can promote a positive immune response that enhances tumor regression and long-term remission. [106, 205] However, there are instances where necrosis may be the preferred mechanism of cell death, such as when PTT is combined with immunotherapy. This is because PTT that induces necrosis can release damage associated molecular patterns and tumor-associated antigens that may engage a tumor-specific immune response to potentiate immunotherapy. [206, 207] Bear and colleagues demonstrated that the

proinflammatory cytokines and chemokines released during PTT-induced necrosis could promote the maturation of dendritic cells in tumor-draining lymph nodes. [112] However, they found this does not contribute to overall antitumor immunity and may even promote the growth of distant metastases unless combined with a form of immunotherapy, in this case adoptive T cell transfer. [112] Chen and colleagues similarly found that combining indocyanine green-mediated PTT with an immune adjuvant imiquimod R837 could generate a vaccine-like function in mice bearing 4T1 TNBC tumors. [206] These examples demonstrate the importance of understanding the fundamental mechanism of cell death induced by PTT, and the need to tailor the mechanism based on the specific application and whether PTT is applied as a standalone or combination therapy.

Since the mechanism of cell death is influenced by the level of tumor heating achieved during treatment, it is important to note that there are several parameters that influence heat production in NP-mediated PTT, including the photothermal conversion efficiency of the NPs, the energy of irradiation applied, the density of the surrounding tissue, and even the localization of the NPs within the target cells and tissue. [208, 209] For example, apoptosis can be achieved as the primary mechanism of cell death by using lower energy irradiation. [106, 210–212] To control NP localization in the tumor microenvironment, targeting agents could be incorporated into the NP design, but there is currently substantial debate surrounding the benefit provided by this strategy, as targeted NPs may not offer a dramatic benefit compared to NPs that rely on strictly passive tumor accumulation. [144] Finally, heat production during PTT could be altered by using NPs with different photothermal conversion efficiencies. Historically, photothermally active NPs used for PTT have been gold-based because

they offer high photothermal conversion efficiencies as well as ease of synthesis and surface modification. [108, 113–116] Nanoshells, in particular, are currently being investigated in clinical trials to mediate PTT of head and neck tumors and prostate tumors. [110, 213, 214] However, gold-based NPs will remain in the body for extended periods of time with unknown long-term health effects. [108] To prevent possible long-term health effects associated with non-degradable NPs, researchers have begun to develop organic, non-gold-based photothermal agents. [119] By incorporating NIR-absorbing dyes into biodegradable platforms, these nanocarriers can facilitate photothermal ablation of tumors, while also providing dual imaging capabilities. [120–128]

Some examples of organic PTT agents reported in the literature include micelles [215] and lipid-based bilayers [216], as well as more complex polymer blends [217] and conjugates [120]. Peng and colleagues have loaded micelles with IR780 dye and labeled these NPs with radionuclide rhenium-188 to further enhance their imaging capabilities. [215] Lovell *et al.* have developed unique NPs designated as porphosomes, which are a self-assembled bilayer of porphyrin that can provide PTT following irradiation with 660 nm light without loading any additional photothermal agents. [216] In addition, Yue and colleagues have created IR780-loaded heparin-folic acid conjugates for targeted imaging and photothermal ablation of MCF-7 xenograft tumors. [120] While these and other organic NP platforms show great promise in treating primary tumors, few studies have examined the mechanism of cell death induced by PTT with these agents, which is critical to maximize treatment success. One such study, conducted by Li *et al.*, used a terminal deoxynucleotidyl transferase dUTP nick end labeling (TUNEL) assay on tumors excised after treatment to show

that their full NP formulation (docetaxel and IR820 co-loaded micelles functionalized with Lyp-1 peptides) could induce apoptosis in tumors in mice leading to remission. [218] This was an exciting finding, but the complexity of this NP formulation may pose a significant barrier to its clinical translation. [6] Similarly, Zheng *et al.* developed polymer NPs encapsulating both doxorubicin and indocyanine green and evaluated their impact on cellular apoptosis and necrosis post-irradiation *in vitro* using an Annexin V/Propidium Iodide (PI) assay. [219] They found that PTT mediated by their NPs induced a substantial amount of cell death, but the amount of cell death was only ~10% greater than that induced by the NPs without light irradiation, which provide strictly doxorubicin delivery. Further, of this additional cell death, >33% was necrotic, rather than apoptotic [219], suggesting there is still more for the field to learn regarding designing biodegradable NPs to maximize apoptosis upon PTT. Overall, these prior studies and others demonstrate that organic PTT agents are an attractive alternative to gold-based NPs that can yield potent anti-tumor effects. [206, 217–219]

In this chapter, we have developed biodegradable, polymeric NPs comprised of poly(lactic-co-glycolic acid) (PLGA) loaded with the NIR-absorbing dye IR820 (IR820-NPs) to enable pro-apoptotic PTT of TNBC. These NPs eliminate the health concerns associated with gold-based NPs and are capable of dual imaging and therapy since IR820 not only heats, but also emits fluorescence at 820 nm upon excitation with 710 nm light, which overlaps with the first characteristic extinction peak of the dye. The ability to image these NPs can inform therapy by indicating when the NPs have maximally accumulated within tumors, marking the optimal time for laser application. We also demonstrate that PTT mediated by these NPs, under the laser irradiation conditions utilized here, induces cell death primarily through apoptosis rather than

necrosis, which is important given the above discussion regarding the consequences this may have on tumor recurrence and metastasis. Overall, we demonstrate the utility of IR820-NPs as potent mediators of pro-apoptotic PTT both *in vitro* and *in vivo*, warranting further investigation of their use to treat TNBC and other forms of cancer that lack effective treatment strategies.

## **3.2 Materials and Methods**

### **3.2.1 Synthesis of IR820-NPs**

IR820-NPs were synthesized using the well-established single emulsion solvent evaporation method. [220] Briefly, PLGA (Lactel, 50:50 carboxylic acid terminated) was dissolved in acetone (VWR) at 1 mg/mL. IR820 dye (Sigma, stored in methanol at 0.5 g/mL) was added to the PLGA in acetone solution at a concentration of 0.5 mg/mL, and this mixture was subsequently added dropwise to distilled water in a 1:3 volume ratio while stirring. This emulsion continued to stir for 2 hours, letting the acetone evaporate. The NPs were then purified using centrifugal filtration (Millipore, 10k MWCO, 4200 g, 30 min) to remove unencapsulated IR820 and excess solvent.

### **3.2.2 Stability and Heating Capacity**

The purified NPs were characterized by dynamic light scattering (DLS) and zeta potential measurements on a Litesizer500 instrument (AntonPaar), and the reported intensity-based hydrodynamic diameter is the z-average of three measurements. DLS measurements of hydrodynamic diameter and polydispersity index, which is an output of the equipment, were taken every two days for one month to demonstrate the NPs' stability in storage conditions (4°C in water). The data shown

are the average of three trials and error bars represent standard deviations. IR820-NP samples for transmission electron microscopy (TEM) were prepared on 400 mesh carbon coated copper grids that were rendered hydrophilic in a Pelco EasiGlow glow discharge unit. The freshly glow discharged grids were floated on drops of the sample for several seconds, washed with Nanopure water, and negative stained with 2% uranyl acetate. After drying, the grids were imaged (Gatan Ultrascan 1000 CCD camera) on a Zeiss LIBRA 120 TEM operating at 120 kV.

IR820 encapsulation in NPs was characterized by UV-visible spectroscopy (Cary60 spectrophotometer, Agilent) based on reading the absorbance of the NPs at 810 nm and comparing to a standard curve of known dye concentration. The samples were scanned from 400-1100 nm with baseline correction at a scan rate of 2400 nm/s. The amount of IR820 released from the NPs while in storage conditions was also examined by UV-visible spectroscopy. At several time points between 0 and 30 days post-preparation, NP samples were centrifuge filtered to separate the NPs from released IR820, and the collected released IR820 was compared to a standard curve of known dye concentration using the same scanning conditions as described above. Studies to analyze IR820 release in storage conditions were performed three times and the data shown are the average and standard deviation of all three trials.

The heating profile of free IR820 and IR820-NPs was measured upon laser excitation with thermal camera imaging (FLIR A5). Samples were suspended in phosphate buffered saline (PBS) at an IR820 concentration of 25  $\mu$ M and incubated at 37°C prior to laser irradiation. The free dye and NP samples were then irradiated with a continuous wave 808 nm laser (B&W Tek) for 5 minutes at 1.5 W/cm<sup>2</sup>. The concentration dependence of the heating profile for IR820-NPs was examined by

irradiating IR820-NPs at concentrations of 10, 25, or 35  $\mu\text{M}$  IR820 with the 808 nm laser set to 1.5  $\text{W}/\text{cm}^2$  for 5 minutes. The dependence of heating on laser intensity was similarly evaluated by irradiating IR820-NPs suspended in PBS at 25  $\mu\text{M}$  with the 808 nm laser set to 0.5, 1, 1.5, 2, or 3  $\text{W}/\text{cm}^2$  for 5 minutes. The temperature in each sample was recorded once every minute during irradiation and experiments were repeated three times. To understand the influence of heating on the optical and physical properties of the NPs, the absorbance spectra, hydrodynamic diameter, and polydispersity index of IR820-NPs stored in PBS at 25  $\mu\text{M}$  were recorded by UV-vis spectroscopy and dynamic light scattering both before and after irradiation of samples with the 808 nm laser at 1.5  $\text{W}/\text{cm}^2$  for 5 minutes. Hydrodynamic diameter and polydispersity index data shown are an average of three measurements taken before and after irradiation. Error bars represent standard deviation.

### **3.2.3 Cell Culture**

MDA-MB-231 TNBC cells (ATCC) were cultured in Dulbecco's Modified Eagle's Medium (DMEM, VWR) supplemented with 10% fetal bovine serum (Gemini Bio Products) and 1% penicillin-streptomycin (VWR). The culture was maintained at 37°C in a 5%  $\text{CO}_2$  humidified environment. When cells reached 80-90% confluency in T75 cell culture flasks, they were passaged or plated by detaching the cells from the flask using Trypsin-EDTA (ThermoFisher) and then counting the cells with a hemocytometer.

### **3.2.4 Cellular Binding and Uptake**

To analyze cellular binding and uptake of free IR820 dye and IR820-NPs by flow cytometry, cells were plated at  $1 \times 10^5$  cells per well in 24-well plates and

incubated overnight. Cells were then treated with 0, 10, 25, or 35  $\mu\text{M}$  free IR820 dye or IR820-NPs (prepared as described above) and incubated for 4 hours to evaluate dose-dependency. To prepare the free IR820 samples, IR820 stored in methanol at 0.5 g/mL was first diluted in PBS to 350  $\mu\text{M}$  and then added to the cell culture media to yield these respective concentrations. After 4 hours, the cells were rinsed with PBS, lifted off the plate with Trypsin-EDTA, and resuspended in PBS to yield a single cell suspension for analysis of uptake by flow cytometry using an Acea Novocyte 2060 flow cytometer. To evaluate time-dependency, cells were treated with 35  $\mu\text{M}$  free IR820 dye or IR820-NPs for 0, 2, 4, 6, or 8 hours prior to rinsing with PBS. The cells were then lifted off the plate with Trypsin-EDTA and resuspended in PBS to yield a single cell suspension. All cell suspensions were analyzed using an Acea Novocyte 2060 flow cytometer with the APC-Cy7 (excitation, 640 nm; emission, 780/60 nm) channel. Density plots showing forward and side scatter data were used to create a primary gate for cells, excluding debris, prior to analyzing IR820 content.

### **3.2.5 Viability Assay and Mechanism of Cell Death**

To evaluate the toxicity of free IR820 and IR820-NPs in the dark using a 3-(4,5-dimethylthiazol-2-yl)-2,5-diphenyltetrazolium bromide (MTT) assay, cells were seeded in a 96-well plate at  $1 \times 10^4$  cells per well and incubated overnight. Cells were treated with 0, 5, 10, 15, 25, or 35  $\mu\text{M}$  of free IR820 dye or IR820-NPs for 4 hours. Then the cells were washed with PBS and incubated in fresh media for an additional 24 hours prior to being incubated in MTT solution per the manufacturer's instructions (ThermoFisher). After 3 hours, the MTT solution was replaced with dimethyl sulfoxide (DMSO) and the absorbance at 540 nm was read on a Synergy H1 plate reader (BioTek). To analyze the data, background (DMSO in wells without cells) was

subtracted from the absorbance reading in each well. Triplicate well signals were averaged and then normalized to untreated cells. These experiments were performed in triplicate and analyzed by Student's *t*-tests at each concentration.

Cells were seeded as described above and treated with IR820-NPs at 35  $\mu\text{M}$  or with fresh media (no treatment control) for 4 hours while incubating at 37°C. The cells were then washed with PBS and incubated in fresh media for 30 minutes to bring the temperature to 37°C. Cells were then irradiated with the 808 nm continuous wave laser at 1.5  $\text{W}/\text{cm}^2$  for 5 min/well. The irradiation was performed at room temperature, with samples returned to the 37°C incubator immediately following irradiation. After 24 hours, an MTT assay was performed as described above. Data shown is from three experiments that were each run with triplicate wells and the data was analyzed by one-way ANOVA with post-hoc Tukey.

To analyze the mechanism of cell death induced by PTT mediated by IR820-NPs, cells were seeded at  $3 \times 10^4$  cells per well in a 24-well plate and incubated overnight. Cells were then treated with 0 or 10  $\mu\text{M}$  IR820-NPs for 4 hours, at which time the cells were rinsed with PBS and the wells replenished with fresh media. The appropriate wells were then irradiated with continuous wave 808 nm light at 2  $\text{W}/\text{cm}^2$  for 5 min/well such that the treatment groups included no treatment, IR820-NPs only, light only, or IR820-NPs + light (PTT). These experiments were performed on a digital dry block heater (VWR) to ensure the initial temperature of 37°C was maintained in each well through all irradiation procedures, and the samples were returned to the incubator after irradiation. After 24 hours, an AnnexinV/PI stain (Cayman Chemicals) was conducted per the manufacturer's instructions. Briefly, cells were lifted from the plate with Trypsin-EDTA, washed with 1x binding buffer, and

resuspended in 50  $\mu$ L binding buffer containing 1:500 Annexin V and 1:1000 PI stains for 10 minutes in the dark. The samples were then diluted with 150  $\mu$ L 1x binding buffer and analyzed on the Acea Novocyte 2060 flow cytometer with FITC (excitation, 488 nm; emission, 530/30 nm) and PerCP (excitation, 488 nm; emission, 675/30 nm) channels. Data analysis was performed in NovoExpress software (ACEA Biosciences). Density plots showing forward and side scatter data were used to create a primary gate for cells, excluding debris, prior to establishing gates for Annexin V-positive and PI-positive cells. Positive stained gates were based off of unstained cells and single stained controls were used for compensation. The data presented are the average of three experiments and were analyzed by one-way ANOVA.

### **3.2.6 Tumor Model**

Female nude mice around 5 weeks old were purchased from Charles River Laboratories. The Institutional Animal Care and Use Committee (IACUC) of the University of Delaware approved the procedures. MDA-MB-231 cells in matrigel (1 x 10<sup>6</sup> cells per 100  $\mu$ L) were administered subcutaneously into the right flank of the mice and tumor growth was monitored at least 3x weekly thereafter with Vernier calipers. Treatments (100  $\mu$ L of either saline, free IR820 dye at a concentration of 350  $\mu$ M, or IR820-NPs at a concentration of 350  $\mu$ M) were administered intravenously when tumors reached 5 mm in diameter. The treatment concentration of 350  $\mu$ M was based off of literature values for intravenously delivered NIR-absorbing dyes. [196, 206, 219, 221] A preliminary biodistribution study utilized 4 mice (2 that received saline and 2 that received IR820-NPs), and a therapeutic efficacy study utilized 47 mice that were treated as follows: saline (8 mice), saline with NIR irradiation (7 mice), free IR820 dye (8 mice), free IR820 dye with NIR irradiation (8 mice), IR820-NPs (8

mice), and IR820-NPs with NIR irradiation (8 mice). Details of these studies are provided in the following sections.

### **3.2.7 Biodistribution Study**

Our previous experience has revealed that 24 hours is typically the optimum time for laser irradiation following intravenous delivery of photothermally active NPs [200, 201], as this is when NPs maximally accumulate in tumors relative to adjacent healthy tissue. To reveal whether 24 hours is also when IR820-NPs display maximum tumor accumulation, during the therapeutic efficacy study, the mice that received 100  $\mu$ L of IR820-NPs were imaged under isoflurane anesthesia with an IVIS Lumina Imaging System (PerkinElmer) both immediately and again every 24 hours for 4 days to monitor IR820 signal in the tumors versus time using the ICG channel (excitation, 788 nm; emission, 813 nm). We did not analyze earlier time points because many of the NPs would likely still be in circulation prior to 24 hours. The fluorescence intensity at each time point was measured in ImageJ software after drawing a region of interest around the tumor, and the mean intensity at each time point was calculated. This confirmed 24 hours was the time of maximum NP accumulation in tumors, so we performed a separate biodistribution study with a small number of mice (2 that received saline, 2 that received IR820-NPs) to reveal the more complete biodistribution of IR820-NPs at this timepoint. Twenty-four hours post-intravenous injection of the saline or IR820-NPs, the mice were euthanized and their major organs (heart, brain, liver, lungs, kidneys, and spleen) and tumors excised for analysis of IR820 signal using the IVIS.

### **3.2.8 Tumor Temperature and Growth**

Mice were injected with 100  $\mu\text{L}$  of free IR820 dye (350  $\mu\text{M}$ ), IR820-NPs (350  $\mu\text{M}$ ), or saline when tumors reached 5 mm in diameter as described above (hereafter, this is referred to as Day 0). Twenty-four hours later, half of the mice in each group were anesthetized with isoflurane and their tumors irradiated with a continuous wave LightForce FXi laser (LiteCure) at  $1.5 \text{ W/cm}^2$  for 5 minutes using a band pass filter at 810 nm. During irradiation, the temperature of the tumor in each mouse was measured every minute using an FLIR A5 thermal camera. The mean and standard deviation of the tumor temperature in each treatment group were calculated. Subsequently, all six groups of mice (saline  $\pm$  laser; free IR820  $\pm$  laser; IR820-NPs  $\pm$  laser) received three additional rounds of treatment on days 7, 14 and 21 for a total of four treatments. The tumor length and width in each mouse were measured with Vernier calipers 3x per week for one month and tumor volume was calculated as  $(\text{tumor length}) \times (\text{tumor width})^2/2$ . These data were used to calculate the mean and standard error of tumor volume in each group, and statistical differences between groups were determined by two-way ANOVA with post hoc Tukey.

### **3.2.9 Biocompatibility**

On day 30, the mice were euthanized and the major organs (spleen, liver, kidneys, heart, lungs, and brain) and tumors were excised for histological analysis by hematoxylin and eosin (H&E) staining. The excised tissues were placed into embedding cassettes, rinsed once in 1x PBS, and then fixed in 4% paraformaldehyde at  $4^\circ\text{C}$  for 72 hours. The tissues were then rinsed 3 times in 70% ethanol for 10 minutes each and stored in 70% ethanol until processing. The fixed tissues were processed and embedded with paraffin. Embedded tissues were cut into 5  $\mu\text{m}$  slices

and stained with H&E to enable visualization of tissue structure. Briefly, the tissues were deparaffinized with xylene and rehydrated prior to hematoxylin staining and subsequent counterstaining with eosin. After staining, the tissues were dehydrated and mounted for imaging with a xylene-based mounting medium. H&E stained tissues were imaged on an Axioobserver Z1 Inverted Fluorescence Microscope (Zeiss).

### 3.3 Results and Discussion

#### 3.3.1 IR820 Dye Maintains its Optical Properties when Encapsulated in Stable, Monodisperse Nanoparticles

IR820-NPs were first characterized with TEM, DLS, and zeta potential measurements, which showed that they are monodisperse and spherical (**Figure 3.1**) with a hydrodynamic diameter of  $60 \pm 10$  nm and a surface charge of  $-40 \pm 6$  mV. The stated synthesis conditions yielded IR820-NPs with 90% encapsulation efficiency and 18% loading capacity.

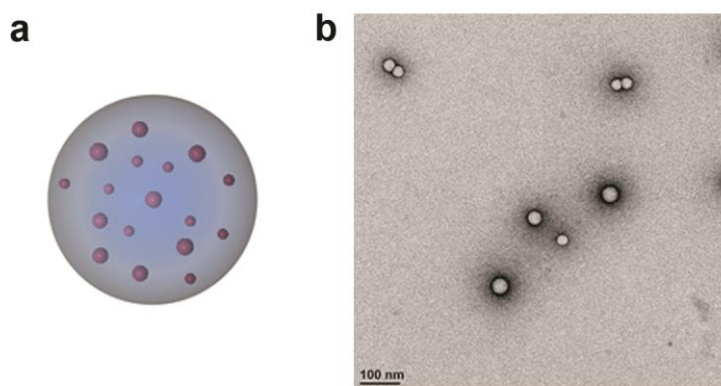


Figure 3.1: Characterization of IR820-NPs. (a) Scheme of IR820-loaded PLGA nanoparticles. (b) TEM image showing the size and morphology of IR820-NPs. Scale bar = 100 nm. Modified from Valcourt, *et al. JBMRA*. 2019. [192]

The heating profile of IR820 dye free in solution or encapsulated in PLGA NPs was examined by irradiating samples diluted in PBS at 25  $\mu\text{M}$  with 808 nm light for 5 minutes at 1.5  $\text{W}/\text{cm}^2$ . Thermal imaging showed that free IR820 dye and IR820-NPs heat similarly (**Figure 3.2a**), indicating that encapsulating the dye does not alter its optical properties or its capacity to heat. Additional testing of the IR820-NPs demonstrated that their heat production is dependent upon both concentration and laser intensity (**Figure 3.2b and 3.2c**).

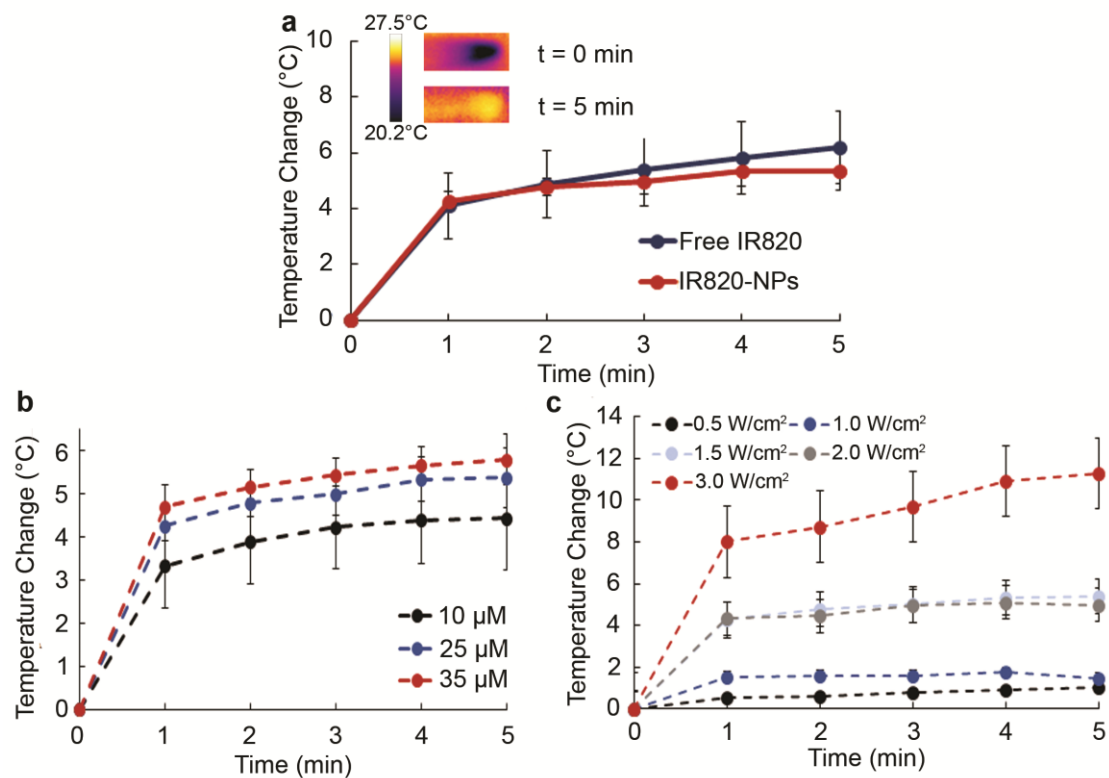


Figure 3.2: Evaluating the heating capacity of free IR820 dye and IR820-NPs. (a) The heating profile of free IR820 dye and IR820-NPs upon laser irradiation with an 808 nm laser at 1.5 W/cm<sup>2</sup>. (b) The heating profile of IR820-NPs suspended in phosphate buffered saline at 10, 25, or 35 μM upon irradiation with an 808 nm laser at 1.5 W/cm<sup>2</sup>. (c) The heating profile of IR820-NPs suspended in phosphate buffered saline at 25 μM upon irradiation with an 808 nm laser at 0.5, 1, 1.5, 2, or 3 W/cm<sup>2</sup>. Modified from Valcourt, *et al. JBMRA*. 2019. [192]

We further examined the optical properties and stability of IR820 dye free in solution or encapsulated in NPs by using UV-visible spectroscopy to analyze the extinction spectrum of freshly made samples and samples that had been stored in water at 4°C for 30 days. Free IR820 dye has two characteristic extinction peaks at 810 and 685 nm that are red-shifted after encapsulation (**Figure 3.3**). After storage in

water at 4°C for 30 days, we observed that free IR820 dye loses its absorption capabilities, whereas IR820 encapsulated in PLGA NPs maintains its optical properties (**Figure 3.3**).

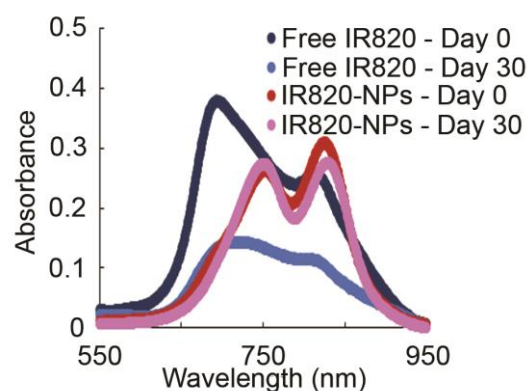


Figure 3.3: The absorption profile of free IR820 dye and IR820-NPs before and after storage in water at 4°C for 30 days as determined by UV-visible spectroscopy. The concentration of IR820 is 25  $\mu\text{M}$  for both free and encapsulated dye. Modified from Valcourt, *et al. JBMRA*. 2019. [192]

To understand whether irradiation leading to heating impacts the optical and physical properties of the NPs, we measured their absorption spectra, hydrodynamic diameter, and polydispersity index before and after irradiation with the 808 nm laser at 1.5 W/cm<sup>2</sup> for 5 minutes. This revealed that IR820-NPs lose their absorption capabilities post-irradiation (**Figure 3.4a**), and this is coupled with an increase in their hydrodynamic diameter and polydispersity index (**Figure 3.4b**). This suggests that IR820-NPs are best suited for application in single rounds of PTT.

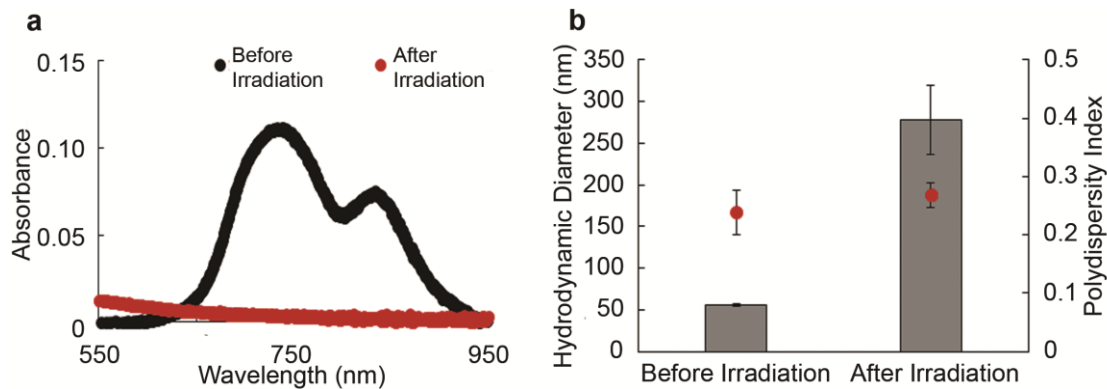


Figure 3.4: Evaluating the stability of IR820-NPs upon laser irradiation. (a) The absorption profile of IR820-NPs (suspended in phosphate buffered saline at 25  $\mu\text{m}$ ) before and after irradiation with the 808 nm laser for 5 minutes at 1.5  $\text{W}/\text{cm}^2$  as determined by UV-visible spectroscopy. (b) The hydrodynamic diameter (gray bars) and polydispersity index (red dots) of IR820-NPs before and after irradiation with the 808 nm laser for 5 minutes at 1.5  $\text{W}/\text{cm}^2$ . Modified from Valcourt, *et al. JBMRA*. 2019. [192]

We also examined the stability of IR820-NPs in storage conditions using DLS. The hydrodynamic diameter and polydispersity index of the NPs were measured every two days for 30 days and showed no notable change throughout this time period (**Figure 3.5a**). There was also negligible release of the IR820 dye from the IR820-NPs over a 30-day storage period after an initial burst release (**Figure 3.5b**).

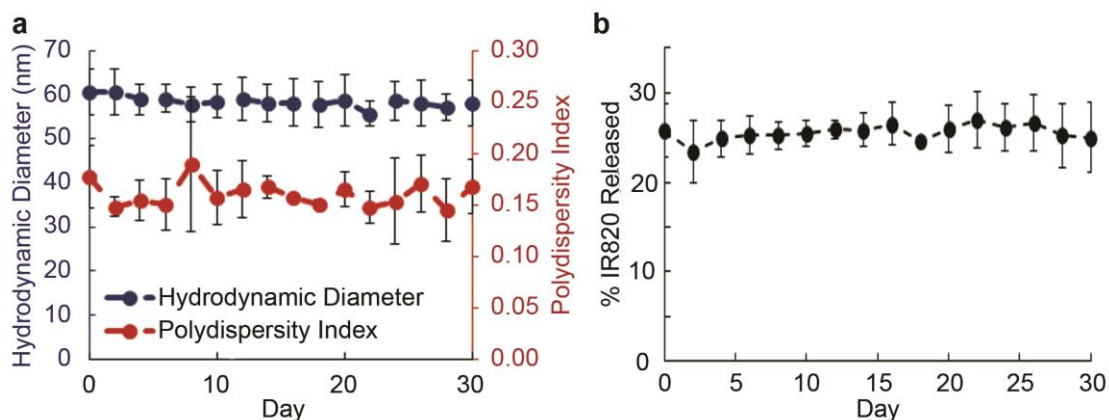


Figure 3.5: Evaluating the stability of IR820-NPs in storage conditions. (a) The hydrodynamic diameter and polydispersity index of IR820-NPs as determined by dynamic light scattering when stored in water at 4°C for 30 days. (b) The release of IR820 from IR820-NPs during storage in water at 4°C as determined by UV-visible spectroscopy. Modified from Valcourt, *et al. JBMRA*. 2019. [192]

Altogether, these data indicate that IR820 encapsulated in PLGA NPs maintains its optical properties and these NPs are monodisperse and stable for at least one month in storage conditions.

### 3.3.2 IR820-NPs Demonstrate Time- and Dose-Dependent Cellular Binding and Uptake

Next, we examined the cellular binding and uptake of free IR820 dye and IR820-NPs in MDA-MB-231 TNBC cells. We treated cells with a range of doses from 0-35  $\mu$ M and flow cytometry showed that binding and/or uptake in cells was dose-dependent for both formulations (**Figure 3.6a**; only data for IR820-NPs is shown). We further evaluated cellular binding and uptake over a range of 8 hours by treating cells with free IR820 dye and IR820-NPs at 35  $\mu$ M. Flow cytometry analysis indicates that, at this dose, cellular binding and uptake of free dye and NPs is also time-dependent

(**Figure 3.6b**; only data for IR820-NPs is shown). Based on these data, we chose to examine the toxicity of each treatment over the full dosing range investigated here. Additionally, we selected 4 hours as the time of treatment incubation for further *in vitro* toxicity and efficacy studies because it was the time needed to achieve a log increase in uptake of the NPs.

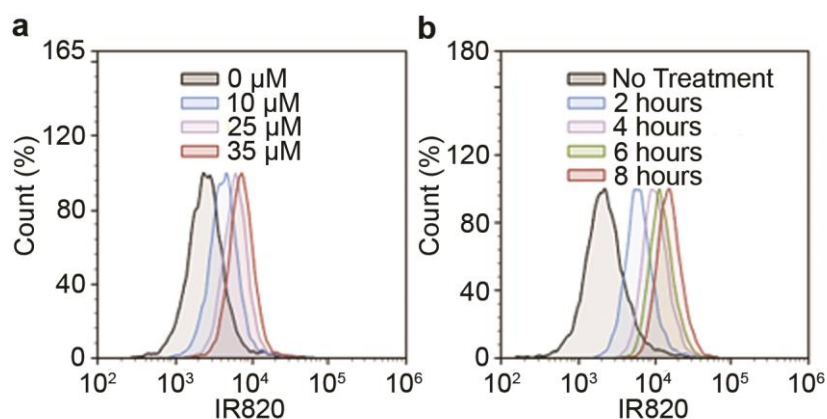


Figure 3.6: Flow cytometric analysis of the cellular binding and uptake of IR820-NPs based on (a) dose and (b) time of incubation. Modified from Valcourt, *et al. JBMRA*. 2019. [192]

### 3.3.3 IR820 Encapsulated in PLGA Nanoparticles Reduces Effect on Cell Viability in the Absence of Light Activation Compared to Free IR820

We used an MTT assay to examine the relative metabolic activity of cells treated with free IR820 dye and IR820-NPs in the absence of light activation. We treated cells with each formulation at a range of doses from 0-35  $\mu\text{M}$  for four hours and then allowed the cells to incubate in fresh media for another 24 hours. The MTT assays showed that free IR820 dye demonstrates toxicity at concentrations above 10  $\mu\text{M}$ , as indicated by cell viability of <80% (**Figure 3.7**). IR820-NPs, however, showed

no toxicity with doses up to 35  $\mu\text{M}$  (**Figure 3.7**). These data indicate that encapsulation of IR820 dye has less effect on metabolic activity and therefore a higher dose can be safely administered.

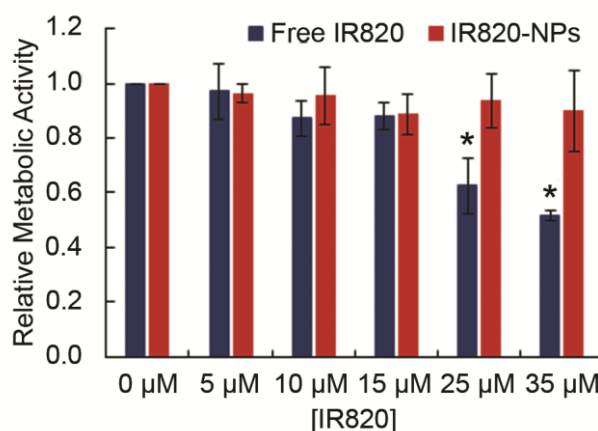


Figure 3.7: Relative metabolic activity of MDA-MB-231 TNBC cells exposed to free IR820 dye or IR820-NPs without light exposure. \* $p < 0.05$  Modified from Valcourt, *et al. JBMRA*. 2019. [192]

### 3.3.4 IR820-NPs Enable Proapoptotic Photothermal Therapy *In Vitro*

We next investigated the use of IR820-NP mediated PTT as a treatment strategy for TNBC and probed the mechanism of cell death induced by this treatment. MDA-MB-231 TNBC cells were exposed to 0 or 35  $\mu\text{M}$  IR820-NPs, the maximum tolerated dose determined previously, for four hours and then half of the samples were irradiated with an 808 nm laser. The combination of IR820-NPs and laser irradiation resulted in a significant reduction in metabolic activity 24 hours post-treatment as measured by an MTT assay (**Figure 3.8**).

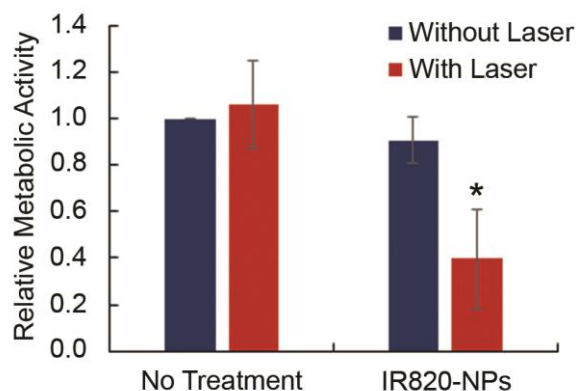


Figure 3.8: Relative metabolic activity of MDA-MB-231 cells that received photothermal therapy mediated by IR820-NPs at 35  $\mu\text{m}$  and laser irradiation versus control cells that were exposed to only saline, only IR820-NPs at 35  $\mu\text{m}$ , or saline and laser irradiation. \* $p < 0.05$  versus untreated control. Modified from Valcourt, *et al. JBMRA*. 2019. [192]

After showing that IR820-NPs can successfully induce cell death, we further evaluated the mechanism through which this occurs. As described previously, it is imperative to induce apoptosis rather than necrosis for optimal therapeutic outcomes. Thus, we assessed the mechanism of cell death by first treating cells with 0 or 10  $\mu\text{M}$  IR820-NPs for 4 hours and then irradiating half of the samples with 808 nm light for 5 min at 2  $\text{W}/\text{cm}^2$ . After 24 hours of incubation, cells were stained with Annexin V (FITC channel) and PI (PerCP channel) for analysis by flow cytometry. Cells that stain positive for Annexin V only (bottom right quadrant) are undergoing early apoptosis, cells that stain positive for Annexin V and PI (top right quadrant) are undergoing late apoptosis, and cells that stain positive for PI only (top left quadrant) are undergoing necrosis. The flow cytometric analysis showed that PTT mediated by IR820-NPs primarily induces cell death through apoptosis with no notable increase in necrotic cell percentage (**Figure 3.9a**, representative scatter plots are shown in **Figure**

**3.9b).** By ANOVA with post-hoc Tukey, the p-value for the difference in apoptosis between media and IR820-NP PTT was 0.1. These data together with the MTT data indicate that IR820-NPs can successfully mediate pro-apoptotic PTT of TNBC *in vitro*.

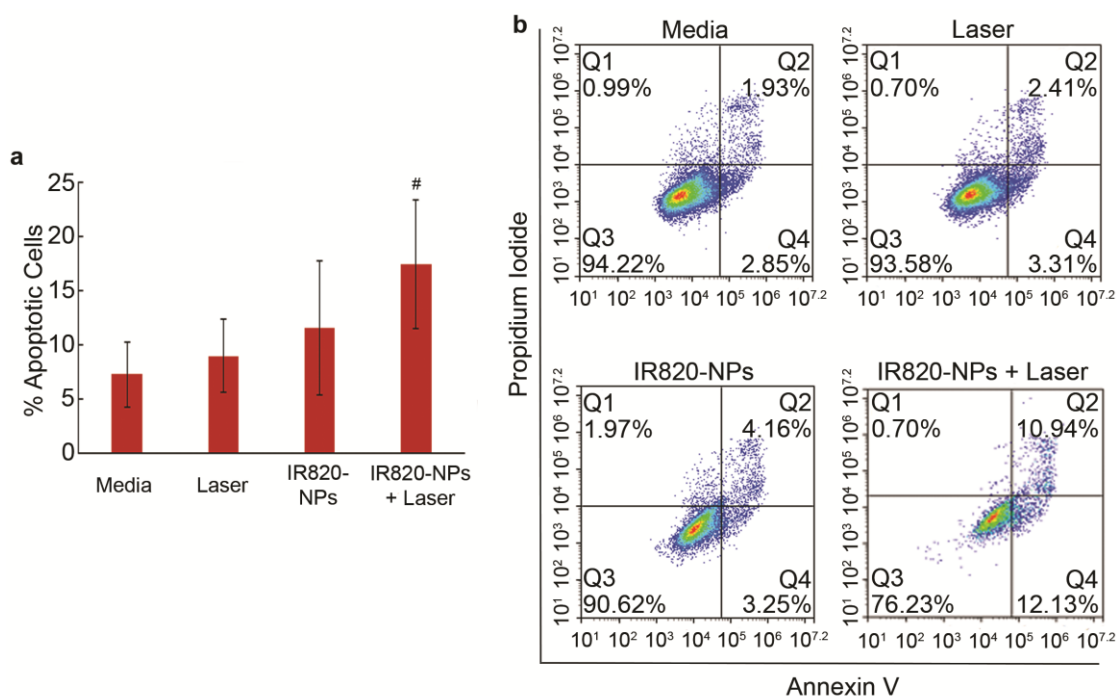


Figure 3.9: Evaluation of mechanism of cell death induced by photothermal therapy mediated by IR820-NPs. (a) The percentage of apoptotic cells in MDA-MB-231 samples that were exposed to no treatment, laser irradiation only, IR820-NPs only (10  $\mu$ m), or photothermal therapy (IR820-NPs and laser irradiation; 10  $\mu$ m). <sup>#</sup>p=0.1 versus untreated control (b) Representative scatter plots demonstrating the fraction of MDA-MB-231 cells in early apoptosis (bottom right quadrant), late apoptosis (top right quadrant), or necrosis (top left quadrant) following treatment with media only, laser irradiation only, IR820-NPs only, or photothermal therapy (IR820-NPs and laser irradiation). Red color indicates a high density of cells and blue color indicates a low density of cells. Modified from Valcourt, *et al. JBMRA*. 2019. [192]

### 3.3.5 IR820-NPs Maximally Accumulate in Tumors Within 24 Hours

After evaluating IR820-NPs *in vitro*, we then examined their ability to mediate PTT of TNBC *in vivo* using a subcutaneous murine xenograft model. First, we investigated the tumor accumulation and biodistribution of these particles after intravenous injection. The tumor accumulation studies, which monitored IR820 signal in the tumors with an IVIS system over a period of 4 days post-injection, indicated that IR820-NPs maximally accumulate in tumors at or before 24 hours (**Figure 3.10a**). We examined the distribution of the IR820 signal in mice exposed to IR820-NPs at 24-hours post-injection by excising the major organs (liver, brain, heart, lungs, kidneys, and spleen) and tumors for *ex vivo* fluorescence imaging. In addition to prominent accumulation of IR820 in the tumors, we also found IR820 signal in the liver, lungs, and kidneys (**Figure 3.10b**). Overall, these data mark the optimal timing for laser irradiation after intravenous injection as 24 hours post-delivery.

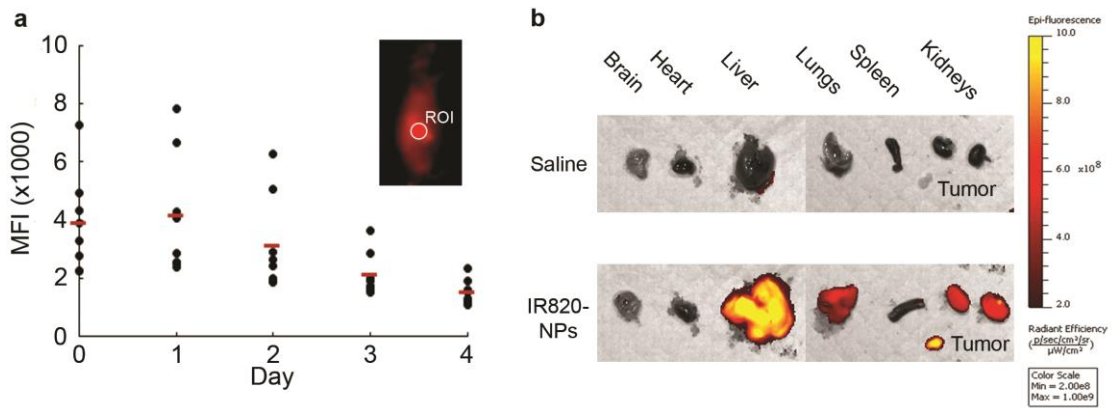


Figure 3.10: Investigating the biodistribution of IR820-NPs *in vivo*. (a) Mean fluorescence intensity (MFI) of IR820 in tumors of mice at different times post-intravenous injection of IR820-NPs. The inset displays a representative image of IR820-NP fluorescence at 24 hours after injection and the region of interest (ROI) in which the fluorescence intensity was measured. (b) *Ex vivo* analysis of IR820 signal in the brain, heart, liver, lungs, spleen, kidneys, and tumors of mice 24 hours after they received intravenous injections of IR820-NPs or saline. Modified from Valcourt, *et al. JBMRA*. 2019. [192]

### 3.3.6 Photothermal Therapy Mediated by IR820-NPs Provides Sufficient Heating of Tumors

Next, we evaluated the ability of free IR820 dye and IR820-NPs to enable tumor heating during irradiation with NIR light by thermal camera imaging. We injected saline, free IR820 dye, or IR820-NPs through the tail vein of tumor-bearing mice and let the treatments circulate for 24 hours. The tumors were then irradiated with an 810 nm laser for 5 minutes and the temperature was monitored with a thermal camera. While free IR820 dye provided mild and un-sustained heating over the five-minute irradiation period, IR820-NPs produced sustained heating above 42°C, the threshold considered sufficient for photothermal therapy under the conditions in this study (**Figure 3.11**). [222]

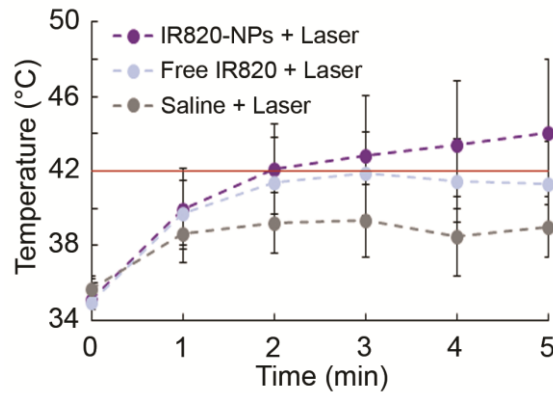


Figure 3.11: Mean tumor temperature in mice treated with saline, free IR820 dye, or IR820-NPs during laser irradiation. These temperatures were recorded during the first of four treatment cycles. The red line at 42°C indicates the threshold considered sufficient to induce photothermal therapy under the conditions in this study. Modified from Valcourt, *et al. JBMRA*. 2019. [192]

### 3.3.7 Photothermal Therapy with IR820-NPs Significantly Reduces Tumor Growth

We then investigated whether PTT mediated by IR820-NPs could reduce tumor growth in our subcutaneous xenograft model. The mice were divided into six treatment groups: saline  $\pm$  irradiation, free IR820 dye  $\pm$  irradiation, and IR820-NPs  $\pm$  irradiation. Throughout a 30-day treatment period, the mice were injected with the treatments and irradiated four times (days indicated by black and red arrows, respectively, in **Figure 3.12a**), and tumor volume was measured three times per week. The mean tumor volume within each treatment group is shown in **Figure 3.12a** and the individual tumor growth curves and final tumor size for each mouse are shown in **Figure 3.12b**. Mice treated with free IR820 dye and irradiated with the laser showed a slight reduction in tumor volume at the end of the treatment period (**Figure 3.12a and 3.12c**). By comparison, mice treated with IR820-NPs and irradiated with the laser

experienced a substantial and statistically significant reduction in tumor growth, and two mice even exhibited complete regression (**Figure 3.12a and 3.12c**).

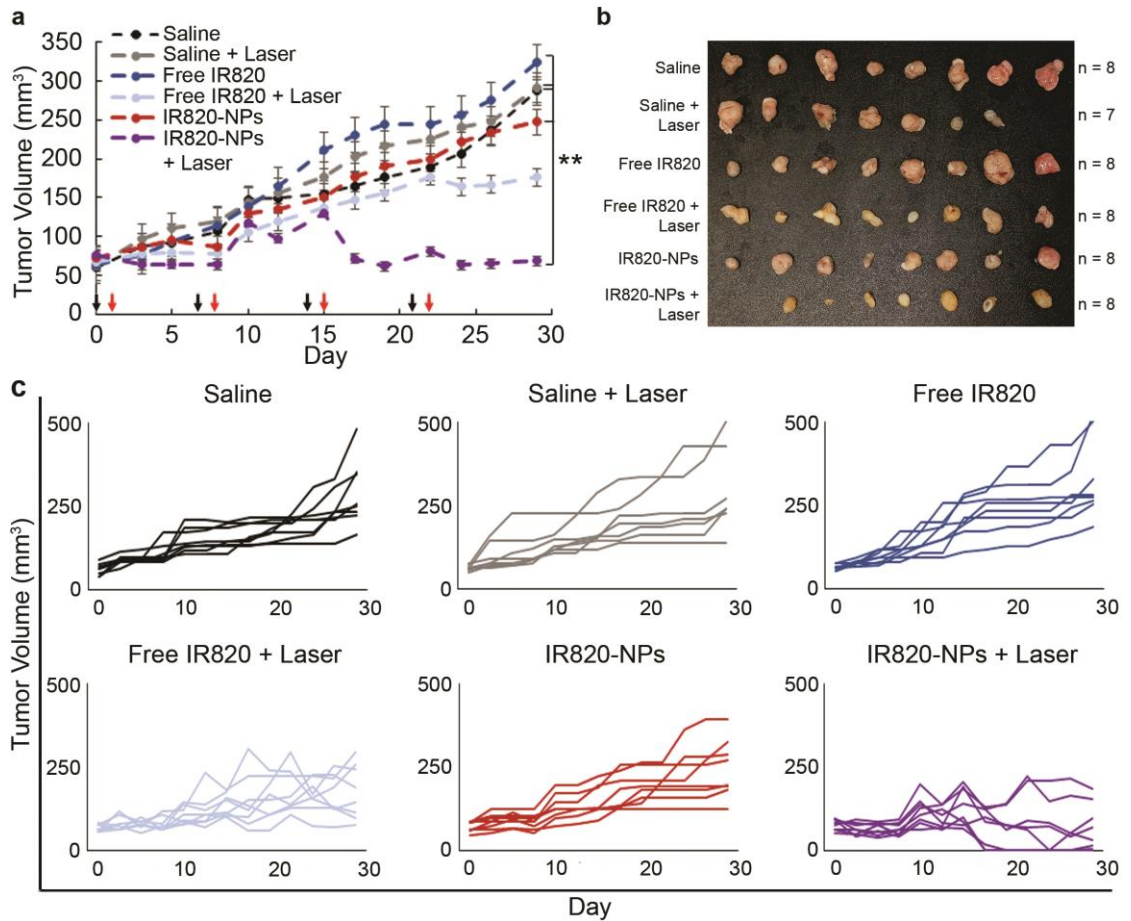


Figure 3.12: Tumor growth following photothermal therapy mediated by free IR820 dye or IR820-NPs. (a) Tumor volume versus time in mice exposed to photothermal therapy mediated by IR820-NPs or various control treatments. All treatments were injected intravenously at an IR820 concentration of  $350 \mu\text{M}$ . Mice whose tumors received laser exposure were irradiated at  $1.5 \text{ W/cm}^2$  for five minutes. Black arrows indicate the days of treatment injections (days 0, 7, 14, and 21) and red arrows indicate the days of laser irradiation (days 1, 8, 15, and 22).  $**p < 0.01$  (b) Image of all tumors excised from individual mice at the time of euthanization (day 30). (c) Tumor volume growth curves for individual mice in each treatment group (treated as described in part (a)). Modified from Valcourt, *et al. JBMRA*. 2019. [192]

Finally, we evaluated the impact of each treatment on the morphology of major organs and tumors using H&E staining. Only the tumors treated with IR820-NPs and irradiated with the laser demonstrated any notable changes in tissue morphology, indicative of the effects of PTT (**Figure 3.13**). Together, these data confirm that the effects of PTT are confined to TNBC tumors where both IR820-NPs and light are applied.

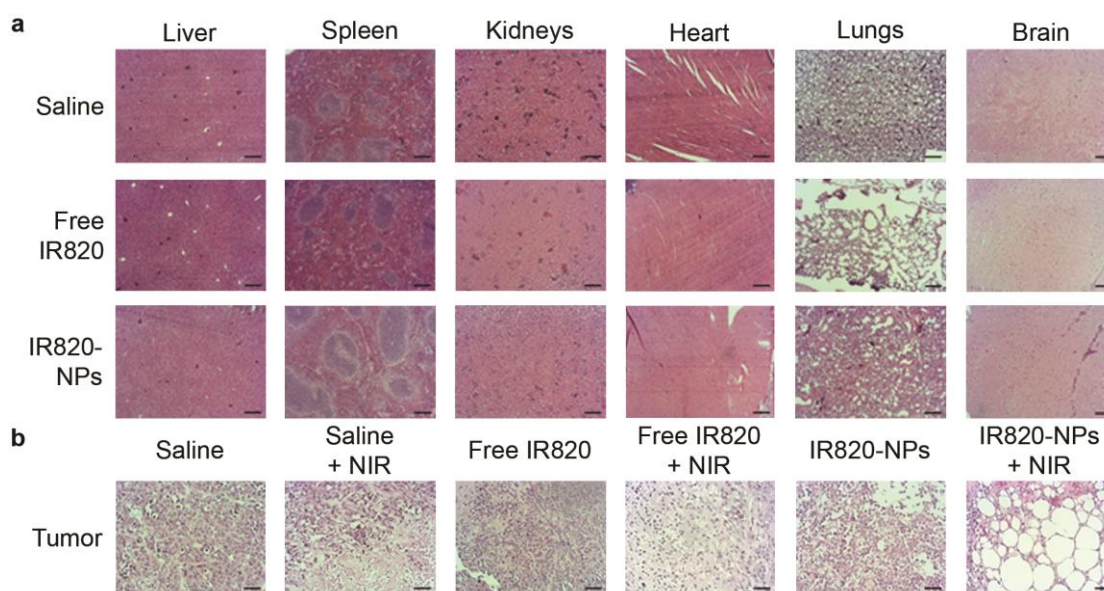


Figure 3.13: (a) Hematoxylin and eosin staining of major organs in mice exposed to saline, free IR820 dye, or IR820-NPs. Scale bars = 200  $\mu\text{m}$  (b) Hematoxylin and eosin staining of tumors in mice exposed to photothermal therapy mediated by IR820-NPs or various controls as indicated. Scale bars = 50  $\mu\text{m}$ . Modified from Valcourt, *et al.* *JBMRA*. 2019. [192]

### 3.3.8 Discussion

PTT has shown promise as an alternative strategy for TNBC therapy, [107, 194–197] and in this chapter we aimed to expand this potential by creating a

biodegradable NP platform that enables pro-apoptotic PTT. The key advantage of PTT relative to other therapies is its high precision, as the use of tissue-penetrating NIR light as an activating source means that heat is produced only where this light and photoresponsive NPs are combined within tumors. In addition, PTT is minimally invasive, has negligible morbidity, and is less susceptible to cellular resistance than other treatments because it induces cell death primarily through physical, rather than biochemical, mechanisms. In the past, PTT has most commonly been mediated by gold-based NPs. [108, 113–116] However, these formulations have unknown long-term health effects and typically result in rapid and very high heating that leads to cellular necrosis. Necrosis has been shown to yield a pro-inflammatory immune response, which can promote tumor recurrence if PTT is not combined with an appropriate immunotherapy regimen. [106, 112, 203] Thus, it is imperative that PTT regimens intended for use as a monotherapy be designed to induce apoptosis, which can yield an anti-inflammatory immune response and promote long-term remission. While it is possible to tune the parameters of PTT mediated by gold-based NPs to primarily induce apoptosis, for example by lowering the intensity of the incident light, these types of NPs will still remain in the body for extended periods of time with unknown long-term consequences. Several researchers have developed biodegradable, NIR-absorbing NPs to address the safety concerns associated with gold-based NPs [120–128, 206, 217–219], but they have not fully evaluated whether the mechanism of cell death induced by PTT with these NPs is primarily apoptotic or necrotic. In this work, we developed biodegradable NPs loaded with IR820 dye, and demonstrated that they enable pro-apoptotic PTT of TNBC. Further, we showed that PTT mediated by these NPs could induce tumor regression *in vivo*. Thus, with this formulation, we not

only address the potential health concern related to gold-based NPs currently used for PTT, but also provide a potent new platform for pro-apoptotic PTT of TNBC.

To evaluate PTT mediated by IR820-NPs as a pro-apoptotic strategy for TNBC therapy, we examined the optical properties and stability of these NPs, their ability to enter cells, their toxicity without light exposure, and their effect on cell viability after irradiation. Our results show that these NPs are stable for one month in storage conditions and that IR820 maintains its optical properties when encapsulated in PLGA. Encapsulation also decreases the toxicity of the dye, which amplifies the dose that can be safely administered for more potent mediation of PTT. We also demonstrated that these NPs can bind and enter MDA-MB-231 cells, as IR820 signal is detectable at significant quantities in and/or on MDA-MB-231 cells over an 8-hour period following NP addition to cell culture, but we have not probed the mechanism by which IR820-NPs might enter these cells. Literature has shown that polymeric micelles can deliver hydrophobic cargo to other cell types through membrane-mediated transport, likely facilitated by poly(ethylene glycol)-induced fusion with the cell membrane. [223] The uptake of NPs composed strictly of PLGA has also been investigated in various cell types, indicating uptake occurs by an endocytic process [224, 225]. Future studies should evaluate the mechanism by which IR820-NPs enter MDA-MB-231 and other TNBC cells using inhibitors of various endocytic pathways to corroborate these prior findings and the results presented here.

In further *in vitro* studies, we demonstrated that PTT mediated by IR820-NPs primarily induces apoptosis, which is vastly preferred over necrosis when PTT is used as a standalone therapy. The treatment conditions used in our analysis of cellular apoptosis versus necrosis likely contributed to the pro-apoptotic results, as we

previously noted that the ability to induce apoptosis versus necrosis depends on a variety of factors, including irradiation time, irradiation intensity, NP concentration, and more [106]. In this chapter, we demonstrate that the heating profile of IR820-NPs is dependent upon both concentration and laser intensity. Thus, we posit that performing these experiments at elevated concentrations and/or laser intensities would increase the relative fraction of cells undergoing necrosis versus apoptosis, though this would have to be evaluated through further experimentation.

We also examined the ability of IR820-NPs to mediate PTT *in vivo* using mice bearing subcutaneous TNBC xenografts by investigating their biodistribution, studying their ability to heat tumors upon light exposure resulting in tumor regression, and examining their impact on off-target organs. Our results demonstrate that IR820-NPs maximally accumulate in tumors within 24 hours after intravenous injection. At this time point, we found notable IR820 signal in the liver, lungs, and kidneys, in addition to significant accumulation in the tumor. Given the size of our NPs, we posit that the IR820 signal in the liver is due to clearance by the mononuclear phagocytic system, and the signal in the kidneys is likely free IR820 dye released from the NPs. While our observation that IR820-NPs accumulate in tumors to a greater extent at 24 hours than at later time points is consistent with our previous experience using other nanoparticles [200, 201], in this study we did not examine time points prior to 24 hours. Future studies should examine the biodistribution and tumor accumulation of IR820-NPs at earlier time points, as these studies may reveal a more optimal time to perform the laser irradiation.

Our results also showed that IR820-NPs produce sufficient heat during tumor irradiation to significantly slow the growth of subcutaneous MDA-MB-231 tumors,

with some mice even experiencing complete remission. The administered dose of IR820 used in these studies (100  $\mu$ L at 350  $\mu$ M) was selected based on prior literature reports using intravenously injected near-infrared absorbing dyes [196, 206, 219, 221]. Traditionally, PTT is only administered once, but in this study we performed four rounds of treatment (one per week). The reason for this is that we were operating under nanoparticle dose and laser irradiation conditions that would induce mild tumor heating, rather than high tumor heating, and we expected that this approach would require more than one round of treatment to induce tumor regression. Indeed, after the third round of treatment we began to observe substantial differences in tumor growth between the IR820-NP PTT group and the other treatment groups. In the future, the nanoparticle dose, laser irradiation conditions, and time of laser irradiation post-nanoparticle injection should be altered to determine whether effective tumor regression can be achieved with only a single round of treatment. In addition, future studies should investigate whether PTT mediated by IR820-NPs is effective against other models of TNBC. Here, we used human MDA-MB-231 cells implanted subcutaneously in nude mice, but several other TNBC models exist that may more accurately reflect the aggressive nature of human TNBC [226–228]. For example, studies could be performed using tumors implanted orthotopically in the mammary fat pad or using murine 4T1 cells that grow in immune-competent mice and can spontaneously metastasize to distant sites after implantation. Since PTT can induce an anti-tumor immune response, performing studies in immune competent animals could more thoroughly reveal the potential impact of this treatment. Further, the use of humanized patient-derived xenograft (PDX) TNBC models that are responsive to immunotherapy could allow for analysis of this strategy in combination with

immunotherapy. Overall, demonstrating the effectiveness of this treatment in several animal models will validate its potential as an anti-TNBC therapy.

Finally, we demonstrated that only tumors that were exposed to both IR820-NPs and light showed notable changes in tissue morphology, consistent with the effects and high precision of PTT. Given that these NPs are biodegradable and the IR820 (which is cytotoxic on its own in high concentrations) will be released over time, future studies should investigate the long-term effects of the released IR820 on the organs in which the IR820-NPs accumulate. Based on the degradation profile of PLGA in physiological conditions [229], we anticipate that the amount of released IR820 present in various tissues would not surpass cytotoxic thresholds. However, future safety studies need to be performed in order to validate the compatibility of this platform and determine the maximum tolerated dose. These should be performed using immune competent animals, as this would most accurately reflect the body's response to the nanoparticles and released IR820.

### **3.4 Conclusions**

In summary, in this chapter we present IR820-loaded PLGA NPs as new, biodegradable, potent mediators of PTT for the treatment of TNBC. These NPs overcome the limitations of other established PTT mediators in that they are biodegradable and enable cell death through apoptosis. Future work should directly compare these IR820-NPs to traditional gold-based PTT agents for a quantitative analysis of the differences seen in each treatment. Additionally, future studies will need to be performed to validate that the mechanism of cell death triggered by PTT with these NPs *in vivo* is also apoptotic, as our studies only confirmed this to be the case *in vitro*. Further, future studies should examine the anti-tumor potency and long-

term safety of this nanoformulation using mice with an intact immune system, as this will reveal the full therapeutic potential of this formulation. Overall, our work lays the foundation for successful use of these IR820-NPs to enable pro-apoptotic PTT of TNBC and other solid cancer tumors.

## Chapter 4

### CO-DELIVERY OF NOTCH-1 ANTIBODIES AND ABT-737 FOR TARGETED DRUG DELIVERY

The work presented in this chapter is adapted from Valcourt, *et al. ACS Nano* (2020); 14(3): 3378-3388. [230]

#### 4.1 Introduction

Triple-negative breast cancer (TNBC) is an aggressive disease that accounts for 15-25% of all breast cancer cases, yet it lacks effective treatment strategies. [8, 193] As its name implies, TNBC does not express the three most common receptors found on other subtypes of breast cancer: estrogen receptor, progesterone receptor, and human epidermal growth factor receptor 2. This characteristic lack of expression leaves TNBC unsusceptible to current targeted or hormonal therapies, thus resulting in high mortality and recurrence rates. [8, 9, 193] In this chapter, we exploited TNBC cells' overexpression of Bcl-2 anti-apoptotic proteins and Notch-1 receptors to develop an effective targeted therapy. [54, 73, 231–233]

The p53 apoptotic pathway is activated in healthy cells when they experience external stress or DNA damage. [193] Upon activation, acetylated p53 migrates to the mitochondria where it induces Bax-mediated release of cytochrome c. Cytochrome c then stimulates a series of caspase activations that ultimately promote apoptosis in the cell. [60] In TNBC, however, the pro-survival protein Bcl-2 is overexpressed and this amplification is associated with poor prognosis. [71, 234] Bcl-2 binds to Bax, suppressing cytochrome c release from the mitochondria to prevent initiation of

apoptosis [60, 235] (**Figure 4.1**). Thus, inhibiting Bcl-2 to promote apoptosis is a promising alternative strategy to combat TNBC. [73]

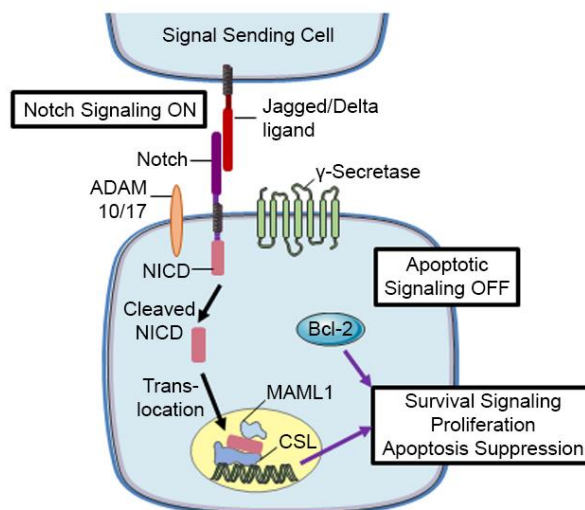


Figure 4.1: Depiction of how Notch signaling and Bcl-2 contribute to TNBC progression. Notch signaling is activated in TNBC cells when overexpressed Notch-1 receptors interact with Jagged or Delta ligands on neighboring cells. This leads to cleavage of the Notch intracellular domain (NICD), which translocates to the nucleus to activate signaling that supports TNBC cell survival, proliferation, and apoptosis suppression. Bcl-2 is an anti-apoptotic protein that is also overexpressed in TNBC and contributes to poor clinical outcomes. Reproduced from Valcourt, *et al. ACS Nano* (2020); 14(3): 3378-3388. [230]

Several methods to inhibit Bcl-2 are in development, and some of these use Bcl-2 homology 3 (BH3) mimetics to bind Bcl-2 directly. [236–238] One such BH3 mimetic, ABT-737, has been shown to potently induce apoptosis in cancer cells characterized by dysregulated p53 signaling by reinstating Bax-mediated release of cytochrome c. [132, 236–239] However, ABT-737 has poor aqueous solubility and has therefore only been delivered orally in the clinic. Unfortunately, orally delivered

ABT-737 has poor bioavailability, so it has not been explored further in clinical trials. [240] An orally bioavailable derivative of ABT-737, Navitoclax (ABT-263), has also been explored in the clinic, but it causes severe thrombocytopenia. [241–243] New strategies for ABT-737 delivery to targeted tumors are needed to allow this drug to realize its clinical potential.

To improve the solubility and bioavailability of ABT-737, two different research teams have encapsulated the drug in nanoparticles (NPs). [131, 132] Schmid *et al.* showed that encapsulating ABT-737 in PEGylated polymeric NPs could reduce the thrombocytopenia associated with delivery of the free drug. [132] They also co-encapsulated a topoisomerase I inhibitor, camptothecin, to achieve synergistic apoptosis in *in vitro* and *in vivo* colorectal cancer models. [132] Jin and colleagues similarly co-encapsulated ABT-737 and an IRAK1/4 inhibitor in PEG-modified poly(lactic co-glycolic acid) (PLGA) NPs to synergistically treat T cell acute lymphoblastic leukemia (T-ALL). [131] They demonstrated that IRAK/ABT-NPs could effectively induce an apoptotic T-ALL fraction at a concentration two-fold lower than the free drug combination *in vitro* and significantly restore white blood cell numbers in the peripheral blood of a T-ALL mouse model. [131] The demonstration that these two NP formulations could effectively mitigate the side effects of ABT-737 while maintaining its potency prompted us to develop a NP platform for targeted delivery of ABT-737 to TNBC. In designing this platform, we desired not only to provide targeted delivery of ABT-737 to TNBC cells, but also to combat resistance to ABT-737 that is present in TNBC cells and driven by Notch signaling.

Recent studies in a variety of cancers have shown that aberrant activation of Notch signaling contributes to cellular resistance to ABT-737. [238, 239, 244] In brief,

the Notch signaling pathway is activated in cancer cells when Jagged/Delta ligands on signal sending cells interact with Notch receptors on signal receiving cells. This leads to a sequence of two cleavages of the Notch transmembrane receptor by ADAM 10/17 and the  $\gamma$ -secretase complex, with the Notch intracellular domain (NICD) ultimately translocating to the nucleus where it promotes the expression of several downstream oncogenes (**Figure 4.1**). [4] Gamma secretase inhibitors are a class of drugs that prevent the second of the Notch receptor cleavage events, thus inhibiting downstream activity in the Notch signaling pathway. [239] When Notch signaling is suppressed, a protein called Noxa that is associated with overcoming resistance to ABT-737 is upregulated. Noxa displaces the Bcl family proteins Bcl-B, Bfl-1, and Mcl-1 from Bax, thus reinstating downstream apoptotic signaling. Accordingly, by combining Notch inhibitors with ABT-737, apoptosis induction is enhanced. [236, 239, 244] Given that Notch signaling is elevated in TNBC [54, 58], and that combining Notch inhibitors with Bcl-2 inhibitors has shown promise in other cancers, we aimed to develop NPs that could enable targeted treatment of TNBC while simultaneously exploiting this dual therapeutic strategy.

In this work, we coated ABT-737-loaded PLGA NPs with Notch-1 antibodies to produce N1-ABT-NPs that enable TNBC cell-specific drug delivery and simultaneous inhibition of Notch signaling. Notch-1 receptors are overexpressed on the surface of TNBC cells [54, 58], and thus provide a handle for NP attachment that helps retain the NPs in the tumor microenvironment. [245] Further, upon binding TNBC cells, the N1-ABT-NPs can block Notch-1 receptor interactions with Jagged/Delta ligands on neighboring cells to suppress Notch signaling. Notably, our group and others have shown that antibody-coated NPs exhibit multivalent binding

that leads to enhanced signal cascade interference relative to freely delivered antibodies. [156, 246] Thus, by functionalizing our NP formulation with Notch-1 antibodies, we can enable Notch signaling inhibition to potentiate the effect of ABT-737 while simultaneously providing targeted drug delivery. In this chapter, we demonstrate that N1-ABT-NPs regulate Bcl-2 and Notch signaling to enhance cell death *in vitro* and reduce tumor burden *in vivo*, warranting their further investigation for treatment of TNBC and other cancers that are characterized by aberrant Bcl-2 and Notch signaling.

## **4.2 Materials and Methods**

### **4.2.1 Synthesis of N1-ABT-NPs**

ABT-737-loaded PLGA NPs were synthesized using the well-established single emulsion solvent evaporation method. [220] Briefly, PLGA (Lactel, 50:50 carboxylic acid terminated) was dissolved in acetone (VWR) at 1 mg/mL. ABT-737 (Selleckchem, stored in dimethyl sulfoxide (DMSO) at 50 mg/mL) was added to the PLGA in acetone solution at a concentration of 0.05 mg/mL, and this mixture was subsequently added dropwise to distilled water in a 1:3 volume ratio while stirring. This emulsion continued to stir for 2 hours, letting the acetone evaporate. The NPs were then purified using centrifugal filtration (Millipore, 10k MWCO, 4200 g, 30 min) to remove unencapsulated ABT-737 and excess solvent. Rabbit anti-human IgG or Notch-1 antibodies were then conjugated to the surface of the NPs using 1-ethyl-3-(3-dimethylaminopropyl)carbodiimide (EDC) chemistry. [220, 247] Briefly, after centrifugal filtration, ABT-737-loaded NPs were suspended in 4 mM EDC and 4 mM n-hydroxysulfosuccinimide sodium salt (sulfo-NHS) and incubated on a rocker at 4°C.

IgG or Notch-1 antibodies were then added to the solution for further incubation at 4°C. To remove free antibodies from solution after conjugation, the NPs were purified using trans-flow filtration (Spectrum, 300 kDa MWCO). NPs were freshly prepared and used immediately for experiments.

#### **4.2.2 Characterization of N1-ABT-NPs and ABT-737 Release**

Purified NPs were characterized by dynamic light scattering (DLS) and zeta potential measurements on a Litesizer500 instrument (AntonPaar) before and after antibody conjugation, and the reported intensity-based hydrodynamic diameter is the average of three measurements. ABT-737 encapsulation and release was quantified by measuring the absorbance at 300 nm on a Synergy H1 plate reader (BioTek). During NP synthesis, all filtrate containing unencapsulated ABT-737 was collected and lyophilized, then suspended in water and the absorbance readings were compared to a standard curve of known ABT-737 concentration. To evaluate the release of ABT-737 in storage (water at 4°C) and physiological (PBS at 37°C) conditions, NPs were suspended in their respective solvents after antibody conjugation and centrifuge filtered (4200 rpm, 30 min) at 4, 8, 24, 48, and 72 hours to remove released ABT-737. All filtrates were lyophilized and ABT-737 concentration quantified as described above. To further evaluate the serum stability of N1-ABT-NPs, NPs were suspended in 0%, 10%, 50%, or 100% fetal bovine serum (FBS) diluted in PBS for 2, 6, 12, and 24 hours at 37°C with gentle shaking. DLS and zeta potential measurements were taken at each time point and the reported hydrodynamic diameter and surface charge are the average of three measurements.

Antibody loading on the NPs was quantified using a solution-based ELISA modified from a previously published protocol. [191] IgG-ABT-NPs, N1-ABT-NPs,

or ABT-NPs were incubated with 10 µg/mL horseradish peroxidase (HRP)-conjugated anti-rabbit IgG antibodies for 1 hour at room temperature. Unbound secondary antibodies were removed through centrifugation and the samples were suspended in 3% bovine serum albumin in PBS. The samples were then developed in 3,3',5,5'-tetramethylbenzidine solution (TMB, Sigma-Aldrich) for 10 minutes before the reaction was stopped with 2 mM sulfuric acid. The absorbance was then measured at 450 nm on a Synergy H1 plate reader and compared to a standard curve of known HRP concentration to calculate the quantity of IgG or Notch-1 antibodies conjugated on 1 mg of PLGA.

#### **4.2.3 Cell Culture**

MDA-MB-231 TNBC cells (American Type Culture Collection, ATCC) were cultured in Dulbecco's Modified Eagle's Medium (DMEM, VWR) supplemented with 10% FBS (Gemini Bio Products) and 1% penicillin-streptomycin (pen-strep; VWR). MCF-10A cells (ATCC) were cultured in DMEM supplemented with 1% pen-strep, 5% FBS, 50 µg/mL bovine pituitary extract (Sigma), 0.5 µg/mL hydrocortisone (Sigma), 20 ng/mL human epidermal growth factor (StemCell Tech), 10 µg/mL insulin (ThermoFisher), and 100 ng/mL cholera toxin (Sigma). The cultures were maintained at 37°C in a 5% CO<sub>2</sub> humidified environment. When cells reached 80-90% confluency in T75 cell culture flasks, they were passaged or plated by detaching the cells from the flask using Trypsin-EDTA (ThermoFisher) and then counting cells with a hemocytometer.

#### **4.2.4 Notch-1 Receptor Expression**

Notch-1 receptor expression in MDA-MB-231 TNBC cells and MCF-10A breast epithelial cells was analyzed using immunocytochemistry staining. Cells were plated at  $2.5 \times 10^4$  cells per well (MDA-MB-231 cells) or  $1.0 \times 10^4$  cells per well (MCF-10A cells) in a 24-well plate and incubated for approximately 48 hours. The cells were then fixed in 4% formaldehyde prior to quenching peroxidase reactions with 3% peroxide. The samples were then rinsed with phosphate buffered saline (PBS) and blocked with 3% bovine serum albumin in PBS (PBSA) for one hour. After blocking, the cells were then rinsed and incubated in primary anti-human Notch-1 antibody (Santa Cruz;  $1 \mu\text{g/mL}$ ) for one hour at room temperature. The samples were subsequently rinsed three times in PBS and incubated in secondary HRP-conjugated goat anti-rabbit IgG antibody (Pierce;  $0.8 \mu\text{g/mL}$ ) for 40 minutes at room temperature. The cells were rinsed three times in PBS and developed in 3-amino-9-ethylcarbazole (AEC) for 15 minutes. Finally, the cells were rinsed in PBS and imaged on a Zeiss Axioobserver Z1 Inverted Fluorescence Microscope.

#### **4.2.5 Cellular Binding and Uptake**

To analyze cellular binding and uptake of antibody-functionalized particles, PLGA NPs were loaded with DiD fluorophores (Fisher Scientific; excitation 644 nm/emission 665 nm) instead of ABT-737 and functionalized as described above to create IgG-DiD-NPs and N1-DiD-NPs. For image-based analysis, cells were plated at  $6 \times 10^4$  cells per well (MDA-MB-231 cells) or  $2.5 \times 10^4$  cells per well (MCF-10A cells) in an 8-well Lab-Tek II chamber slide and incubated overnight. Cells were then treated with IgG-DiD-NPs and N1-DiD-NPs at 80 nM DiD or were left untreated and incubated for 4 hours. After 4 hours, the cells were rinsed with PBS to remove

unbound NPs, fixed in 4% formaldehyde, and permeabilized with 0.5% Triton X-100 in PBS with 5% bovine serum albumin. The cells were then counterstained with DyLight<sup>TM</sup>554-Phalloidin (Cell Signaling Technology) overnight at 4°C. The slides were mounted in ProLong Gold Antifade with DAPI (Vectashield) and imaged on an Axioobserver Z1 Inverted Fluorescence Microscope (Zeiss).

For flow cytometric analysis of cellular binding and uptake, cells were plated at  $3 \times 10^4$  cells per well (MDA-MB-231 cells) or  $2 \times 10^4$  cells per well (MCF-10A cells) in a 24-well plate and incubated overnight. Cells were then treated with IgG-DiD-NPs and N1-DiD-NPs at 50 nM DiD or were left untreated and incubated for 0, 1, 4, 8, 12, 16, or 24 hours prior to rinsing with PBS. The cells were then lifted off the plate with Trypsin-EDTA and resuspended in PBS to yield a cell suspension. All cell suspensions were analyzed using an Acea Novocyte 2060 flow cytometer with the APC (excitation, 640 nm; emission, 675/30 nm) channel. Density plots showing forward and side scatter data were used to create a primary gate for cells, excluding debris, prior to analyzing DiD content. Flow cytometric analysis was performed in triplicate.

#### **4.2.6 Cell Viability**

To evaluate the toxicity of freely delivered ABT-737 and IgG or Notch-1 antibodies versus nanocarriers (i.e., IgG-ABT-NPs and N1-ABT-NPs) using a 3-(4,5-dimethylthiazol-2-yl)-2,5-diphenyltetrazolium bromide (MTT) assay, MDA-MB-231 cells were plated at  $5 \times 10^3$  cells per well in a 96-well plate and incubated overnight. Cells were treated with 0, 1, 2, 3, 4, or 5  $\mu$ M ABT-737 and 0, 0.3, 0.6, 0.9, 1.2, or 1.5  $\mu$ g/mL IgG or Notch-1 antibody, either freely in solution or in NP form for 72 hours. After 72 hours, the treatments were removed, and the cells were incubated in MTT

solution per the manufacturer's instructions (ThermoFisher). After 3 hours, the MTT solution was replaced with DMSO and the absorbance at 540 nm was read on a Synergy H1 plate reader (BioTek). To analyze the data, background (DMSO in wells without cells) was subtracted from the absorbance reading in each well. Triplicate well signals were averaged and then normalized to untreated cells. These experiments were performed in triplicate and data was analyzed by one-way ANOVA with post-hoc Tukey.

#### **4.2.7 Cell Proliferation**

To analyze the effect of IgG-ABT-NPs and N1-ABT-NPs on cellular proliferation via an EdU assay, cells were seeded at  $1.0 \times 10^5$  cells per well in a 12-well plate and incubated overnight. Cells were then treated with IgG-ABT-NPs or N1-ABT-NPs at 3  $\mu$ M ABT-737 for 72 hours. 16 hours prior to the end of the treatment period, cells were spiked with EdU at 10  $\mu$ M. Cells were then prepared per the manufacturer's instructions modified for a single cell suspension. Briefly, cells were fixed in 4% formaldehyde and permeabilized with 0.5% Triton X-100. They were subsequently incubated in the Click-iT reaction cocktail, washed in PBS, and examined on an Acea Novocyte 2060 flow cytometer with the FITC (excitation, 488 nm; emission, 530/30 nm) channel. Density plots showing forward and side scatter data were used to create a primary gate for cells, excluding debris, prior to analyzing EdU-labeling azide content. Flow cytometric analysis was performed in quadruplicate and statistical analysis was performed using a one-way ANOVA with post-hoc Tukey.

#### 4.2.8 Quantitative Real-Time Polymerase Chain Reaction

To determine the effects of IgG-ABT-NPs and N1-ABT-NPs on gene expression in TNBC cells by quantitative real-time polymerase chain reaction (qRT-PCR), MDA-MB-231 cells were seeded at  $1.5 \times 10^5$  cells per well in a 6-well plate and incubated overnight. Cells were then treated with IgG-ABT-NPs or N1-ABT-NPs at 3  $\mu$ M ABT-737 for 72 hours. At the conclusion of the treatment period, cells were rinsed with PBS and mRNA was extracted using a Bioline Isolate II RNA Mini Kit. qRT-PCR was then performed using SensiFAST SYBR One-Step Master Mix on a LightCycler 96 (Roche) and gene expression was normalized to that of RPLPO. These experiments were performed in triplicate and analyzed using a one-way ANOVA with post-hoc Tukey. Primer sequences are listed in **Table 4.1**.

Table 4.1: Primer sequences used for qPCR. Reproduced from Valcourt, *et al. ACS Nano* (2020); 14(3): 3378-3388. [230]

Gene	Forward Sequence	Reverse Sequence
RPLPO	AACCCAGCTCTGGAGAAACT	CCCCTGGAGATTTTAGTGGT
Bcl-2	GACTTCTCCCGCCGCTACC	CCCAGTTCACCCCGTCCCT
Noxa	GCTGGAAGTCGAGTGTGCTA	CCTGAGCAGAAGAGTTTGGA
Hes5	CCGGTGGTGGAGAAGATGCG	GCGACGAAGGCTTTGCTGTG
HeyL	AGCCAGGAAGAAACGCAGAGG	GCTGTTGAGGTGGGAGAGAAGG

#### 4.2.9 Western Blotting

To further evaluate the effects of N1-ABT-NPs on Bcl-2 and Notch signaling targets by Western blotting, MDA-MB-231 cells were plated at  $1.5 \times 10^5$  cells per well in a 6-well plate and incubated overnight. Cells were then treated as described for qRT-PCR. After 72 hours of treatment with IgG-ABT-NPs or N1-ABT-NPs, the cells were rinsed with PBS and lysed in RIPA buffer supplemented with Halt Protease Inhibitor in a 1:50 volume ratio. After removing membrane debris through

centrifugation, the extracted protein was quantified using a DC Protein Assay (BioRad), and 10  $\mu$ g of protein was separated on 4-12% Bis-tris gels at 135V for 60 minutes. Then, the protein was transferred to a 0.2 micron nitrocellulose membrane for 10 minutes using a Power Blotter System (Invitrogen). The membrane was subsequently blocked for 60 minutes in 5% milk in tris buffered saline with 0.1% Tween-20 (TBS-T) and then incubated with rabbit anti-human Bcl-2 (ProteinTech; 1:1000), cleaved Notch-1 (Cell Signaling Technology; 1:250), and Hes1 antibodies (Cell Signaling Technology; 1:500) in 5% milk in TBS-T overnight at 4°C. Mouse anti-human  $\beta$ -actin antibody (Cell Signaling Technology; 1:20,000) was used as the normalization control. After incubation in primary antibodies, membranes were washed 3x in TBS-T and incubated with HRP-anti-rabbit or mouse IgG antibody (VWR; 1:25,000) in 5% milk in TBS-T for 1 hour at room temperature. Membranes were then washed 2x in TBS-T and 2x in TBS (without Tween-20) and protein bands were visualized using a Pierce enhanced chemiluminescence detection solution (ECL, Thermo Scientific). Band densities were quantified in ImageJ and Bcl-2, cleaved Notch-1, and Hes1 densities were normalized to that of  $\beta$ -actin prior to further normalizing treatment groups to the control untreated group. The data shown represents the average band density across three trials and was analyzed using a one-way ANOVA with post-hoc Tukey.

#### **4.2.10 Tumor Model**

Female nude mice around 5 weeks old were purchased from Charles River Laboratories. The Institutional Animal Care and Use Committee (IACUC) of the University of Delaware approved all procedures. MDA-MB-231 cells in matrigel (1 x 10<sup>6</sup> cells per 100  $\mu$ L) were administered subcutaneously into the right flank of the

mice and tumor growth was monitored at least 3x per week afterwards with Vernier calipers. Treatments for three separate studies were administered intravenously when tumors reached 5 mm in diameter. A preliminary biodistribution study utilized 6 mice per treatment group (saline, IgG-DiD-NPs, N1-DiD-NPs), a dose optimization study utilized 6 mice per treatment group (saline, IgG-ABT-NPs, N1-ABT-NPs), and a larger therapeutic study utilized 8 mice per treatment group (saline, IgG-ABT-NPs, N1-ABT-NPs). Details of these studies are provided in the following sections.

#### **4.2.11 Biodistribution Study**

To reveal the time of maximum NP accumulation within tumors following intravenous administration, mice were injected with 100  $\mu$ L saline or with IgG-DiD-NPs or N1-DiD-NPs at a concentration of 50  $\mu$ M DiD. These mice were imaged under isoflurane anesthesia with an IVIS Lumina Imaging System (PerkinElmer) immediately, 6 hours, 12 hours, and 24 hours after injection to monitor DiD signal in the tumors versus time using the Cy5.5 (excitation, 678 nm; emission, 694 nm) channel. The fluorescence intensity within the tumors at each time point was measured in ImageJ software after drawing a region of interest (ROI) around the tumor, and the mean intensity at each time point was calculated.

#### **4.2.12 Tumor Growth and Survival**

Mice were injected with saline or with IgG-ABT-NPs or N1-ABT-NPs as doses of 10 mg ABT-737/kg when tumors reached 5 mm in diameter (day 0) for a dose optimization and full study, as described above. For the dose optimization study, mice received two subsequent injections on days 7 and 14 for a total of three treatments. The tumor length and width in each mouse were measured with Vernier

calipers 3x per week until day 21 and tumor volume was calculated as (tumor length) x (tumor width)<sup>2</sup>/2. These data were used to calculate the mean tumor volume in each group and the relative tumor volume compared to day 0. On day 21, the mice were euthanized. Statistical analysis was performed on the average percent change in tumor volume using a one-way ANOVA with post-hoc Tukey.

For the full therapeutic study in which treatment was performed twice per week, mice were injected as stated above on day 0 and received seven subsequent injections on days 4, 7, 11, 14, 18, 21, and 25 for a total of eight treatments. The tumor length and width in each mouse were measured with Vernier calipers 3x per week until day 55 and tumor volume was calculated as above. Mice were euthanized upon >20% loss in weight, when tumors reached 10 mm in diameter, or on day 55, whichever came first. These data were used to create the presented Kaplan-Meier survival curves, and statistical significance was examined using a log-rank test.

#### **4.2.13 Biocompatibility**

Upon euthanasia, the major organs (spleen, liver, kidneys, heart, GI tract, lungs, and brain) of the mice used in the full therapeutic study were excised for histological analysis by hematoxylin and eosin (H&E) staining. The excised tissues were placed into embedding cassettes, rinsed once in 1x PBS, and then fixed in 4% paraformaldehyde at 4°C for 72 hours. The tissues were then rinsed 3 times in 70% ethanol for 10 minutes each and stored in 70% ethanol until processing. The fixed tissues were processed and embedded with paraffin. Embedded tissues were cut into 5 µm slices and stained with H&E to enable visualization of tissue structure. Briefly, the tissues were deparaffinized with xylene and rehydrated prior to hematoxylin staining and subsequent counterstaining with eosin. After staining, the tissues were dehydrated

and mounted for imaging with a xylene-based mounting medium. H&E stained tissues were imaged on an Axioobserver Z1 Inverted Fluorescence Microscope (Zeiss).

### **4.3 Results and Discussion**

#### **4.3.1 Characterization of Antibody and Drug Loading in N1-ABT-NPs**

N1-ABT-NPs synthesized as described in the Methods were characterized using dynamic light scattering (DLS), zeta potential, absorbance, and enzyme-linked immunosorbent assay (ELISA) measurements, which demonstrated that antibodies were successfully conjugated to the surface of ABT-737-loaded NPs. Before antibody conjugation, ABT-737-loaded NPs had a hydrodynamic diameter of  $52.8 \pm 0.9$  nm and a surface charge of  $-41.3 \pm 5.6$  mV, with 48  $\mu$ g ABT-737 encapsulated per 1 mg of PLGA (**Figure 4.2a and 4.2b**). Upon conjugation of IgG or Notch-1 antibodies, the NPs' hydrodynamic diameter increased by approximately 20 nm and the zeta potential approached neutral, indicating successful antibody attachment (**Figure 4.2a**). During antibody conjugation, about 50% of the encapsulated ABT-737 is lost, leaving 23-26  $\mu$ g drug encapsulated per mg PLGA (**Figure 4.2b**).

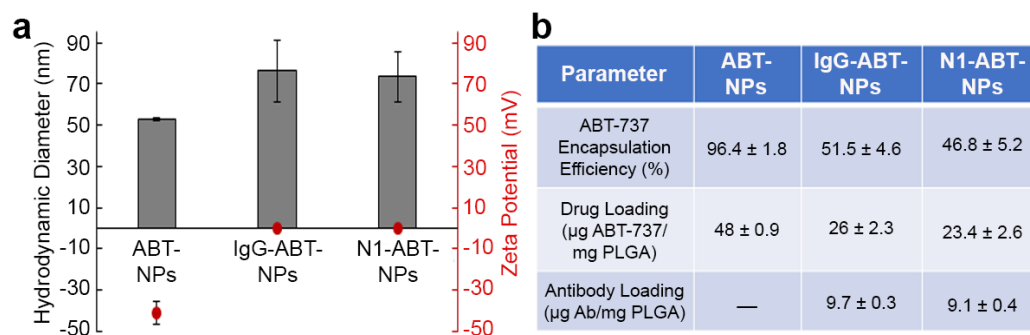


Figure 4.2: Characterization of N1-ABT-NPs. (a) Hydrodynamic diameter and zeta potential of ABT-737-loaded nanoparticles before and after antibody conjugation with IgG or Notch-1 antibodies. (b) Loading of ABT-737 and antibodies before and after antibody conjugation. Modified from Valcourt, *et al. ACS Nano* (2020); 14(3): 3378-3388. [230]

We further evaluated the release of ABT-737 from the NPs in storage (4°C in water) and physiological conditions (37°C in phosphate buffered saline) over a three-day period using absorbance values of the lyophilized drug no longer encapsulated in the NPs. After 72 hours in storage conditions, less than 15% of the ABT-737 was released from N1-ABT-NPs. At 37°C in PBS, however, up to 55% was released within the same 72-hour time period (**Figure 4.3**).

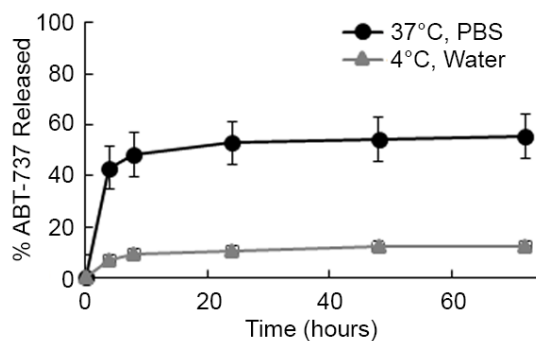


Figure 4.3: ABT-737 release from N1-ABT-NPs in storage (4°C, water) and physiological (37°C, phosphate buffered saline (PBS)) conditions. Modified from Valcourt, *et al. ACS Nano* (2020); 14(3): 3378-3388. [230]

We then examined the stability of N1-ABT-NPs in 0%, 10%, 50%, and 100% FBS over a 24-hour period. The hydrodynamic diameter (**Figure 4.4a**) and zeta potential (**Figure 4.4b**) of these NPs remained relatively stable at serum concentrations up to 50%. When incubated in 50% and 100% FBS, the size and surface charge of these NPs notably increased over 24 hours, indicating a substantial protein corona accumulates on the particles at these higher serum concentrations. Altogether, these data demonstrate ABT-737 can be successfully loaded inside antibody-functionalized NPs that are stable and will release the therapeutic cargo upon exposure to physiological conditions.

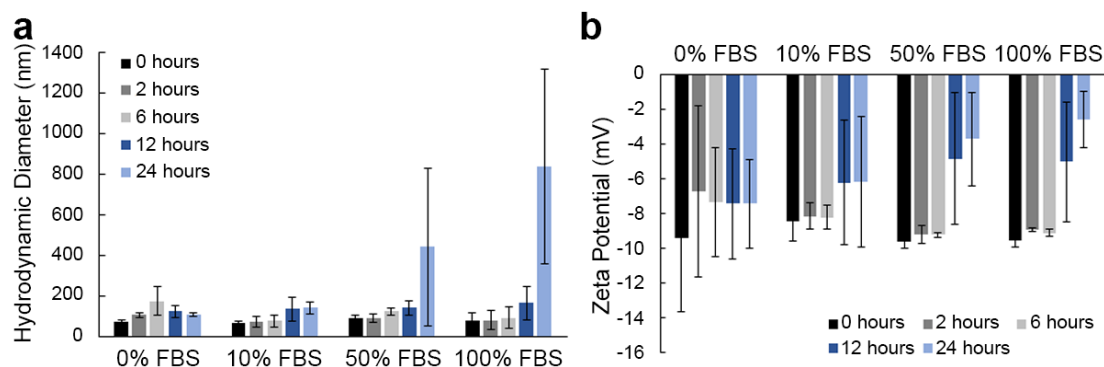


Figure 4.4: Serum stability of N1-ABT-NPs. (a) Hydrodynamic diameter and (b) zeta potential of N1-ABT-NPs in 0%, 10%, 50%, and 100% fetal bovine serum (FBS) over 24 hours. Valcourt, *et al. ACS Nano* (2020); 14(3): 3378-3388. [230]

#### 4.3.2 Notch-1 Antibody Functionalization Enables Preferential Nanoparticle Interaction with TNBC Cells

Next, we evaluated how Notch-1 and IgG antibody-functionalized NPs interacted with MDA-MB-231 TNBC cells that overexpress the Notch-1 receptor (**Figure 4.5**), and with healthy MCF-10A mammary epithelial cells that have low Notch-1 receptor expression (**Figure 4.5**).

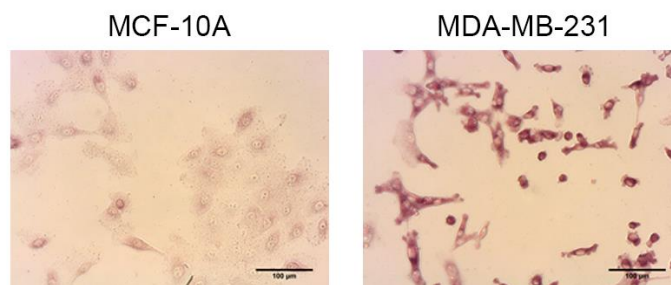


Figure 4.5: Immunocytochemistry staining for the Notch-1 receptor (dark red signal) in MCF-10A healthy mammary cells and MDA-MB-231 TNBC cells. Scale bars = 100  $\mu$ m. Modified from Valcourt, *et al. ACS Nano* (2020); 14(3): 3378-3388. [230]

For these studies, the NPs were loaded with DiD fluorophores to enable their detection by fluorescence microscopy and flow cytometry. We treated cells with IgG-DiD-NPs or N1-DiD-NPs at 80 nM DiD for 4 hours, after which DiD was only detected in MDA-MB-231 TNBC cells by fluorescence microscopy when delivered via Notch-1 functionalized NPs (**Figure 4.6a**). IgG-DiD-NPs showed minimal interaction with either MDA-MB-231 cells (**Figure 4.6a**) or MCF-10A cells, and N1-DiD-NPs demonstrated low levels of interaction with MCF-10A cells that lack Notch-1 receptor overexpression (**Figure 4.5**). We further analyzed NP interaction with both cell types using flow cytometry after treating cells for 1, 4, 8, 12, 16, or 24 hours. At each time point, N1-DiD-NPs showed enhanced interaction with MDA-MB-231 TNBC cells relative to IgG-DiD-NPs and this interaction was time-dependent (**Figure 4.6b and 4.6c**). After 24 hours, MDA-MB-231 cells treated with N1-DiD-NPs exhibited 3-fold higher median fluorescence intensity than cells treated with IgG-DiD-NPs. The fluorescence intensity of MCF-10A cells treated with N1-DiD-NPs was similar to the background levels observed for MDA-MB-231 cells treated with IgG-DiD-NPs, indicating minimal interaction between N1-DiD-NPs and MCF-10A cells (**Figure 4.6c**). Overall, these data indicate that Notch-1 antibody functionalization provides enhanced and specific NP interaction with MDA-MB-231 TNBC cells.

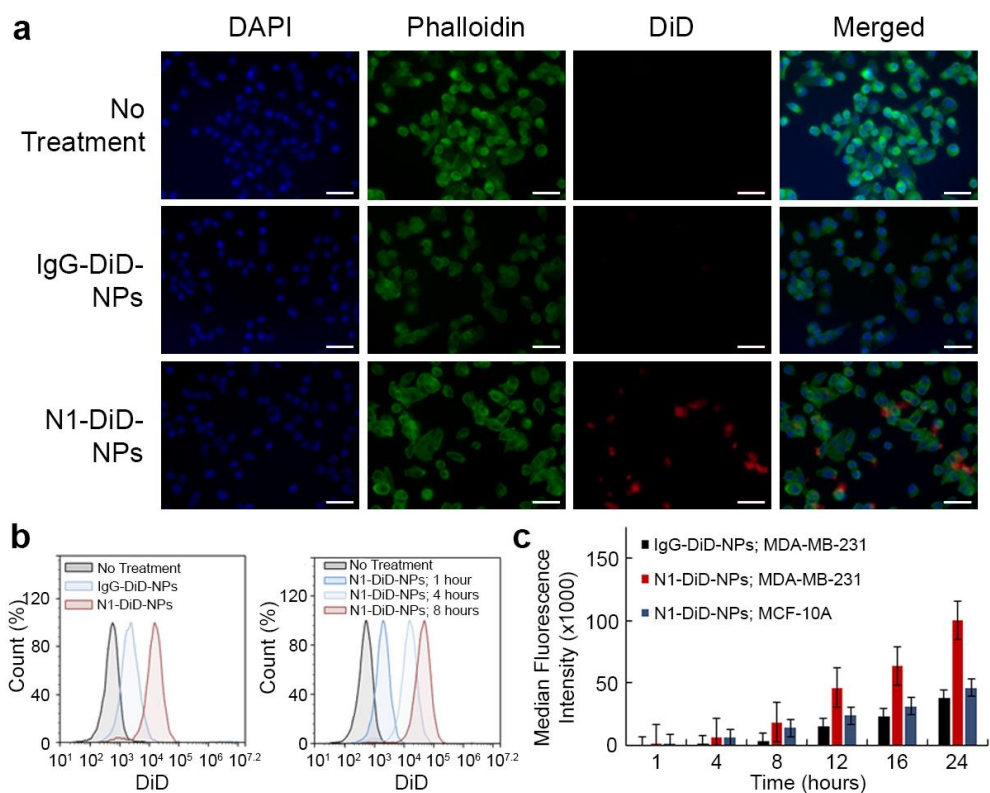


Figure 4.6: Analysis of N1-DiD-NPs' interaction with TNBC cells versus healthy breast epithelial cells. (a) Fluorescence microscopy images showing MDA-MB-231 TNBC cells treated with no nanoparticles, IgG-DiD-NPs, or N1-DiD-NPs. Cell nuclei are blue (DAPI), actin is green (Phalloidin), and nanoparticles are red (DiD). Scale bars = 50  $\mu\text{m}$ . (b) Representative flow cytometry histograms of MDA-MB-231 TNBC cells exposed to IgG-DiD-NPs or N1-DiD-NPs. (c) Median DiD fluorescence intensity of MDA-MB-231 TNBC cells and healthy MCF-10A mammary cells treated with N1-DiD-NPs or IgG-DiD-NPs as measured by flow cytometry. Reproduced from Valcourt, *et al. ACS Nano* (2020); 14(3): 3378-3388. [230]

### 4.3.3 N1-ABT-NPs Induce TNBC Cell Death and Reduce Proliferation *In Vitro*

To determine if Notch-1 antibody-functionalized NPs can potentiate the effect of ABT-737 against TNBC cells, we examined the relative metabolic activity of MDA-MB-231 cells treated with free ABT-737 and IgG or Notch-1 antibodies or with

nanocarriers of the drug and antibodies. After a 72-hour treatment period, MTT assays showed that, when freely delivered in combination with either IgG antibodies or Notch-1 antibodies, the  $IC_{50}$  of ABT-737 is approximately 2.6  $\mu\text{M}$  (**Figure 4.7**). When encapsulated in IgG-functionalized NPs, the  $IC_{50}$  remains in the same range as the freely delivered components, at a value of 3.2  $\mu\text{M}$ . By comparison, when delivered via N1-ABT-NPs, the  $IC_{50}$  drops notably to 1.6  $\mu\text{M}$  (**Figure 4.7**). This demonstrates that using a nanocarrier to co-deliver Notch-1 antibodies and ABT-737 to TNBC cells is advantageous versus delivering the molecules freely in solution. Further, it supports the conclusions of prior studies that show Notch inhibitors can potentiate the effects of ABT-737.

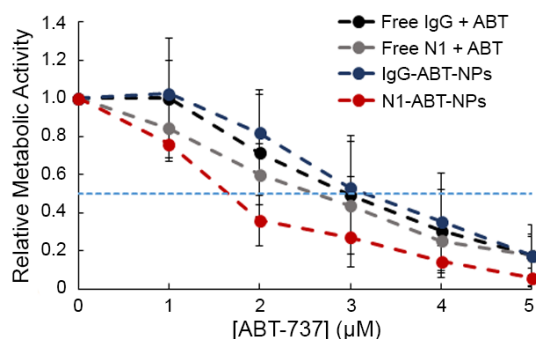


Figure 4.7: Relative metabolic activity of MDA-MB-231 cells treated with different doses of freely delivered IgG or Notch-1 (N1) antibodies and ABT-737 or with nanocarriers (IgG-ABT-NPs or N1-ABT-NPs) as measured by an MTT assay. Horizontal dotted line indicates 50% reduction in metabolic activity. Modified from Valcourt, *et al. ACS Nano* (2020); 14(3): 3378-3388. [230]

We further evaluated the impact of N1-ABT-NPs on TNBC cell function using an EdU proliferation assay. We treated cells with NPs at a dose corresponding to 3  $\mu\text{M}$

ABT-737 and 0.9  $\mu\text{g/mL}$  antibodies for 72 hours. The EdU assay results demonstrate that IgG-ABT-NPs cause a mild reduction in cell proliferation, but N1-ABT-NPs significantly reduce the percentage of proliferative cells by 46% (**Figure 4.8a**, representative histograms in **Figure 4.8b**). This corroborates the MTT data that indicate that Notch-1 functionalized, ABT-737-loaded NPs can potently suppress TNBC cell viability and proliferation.

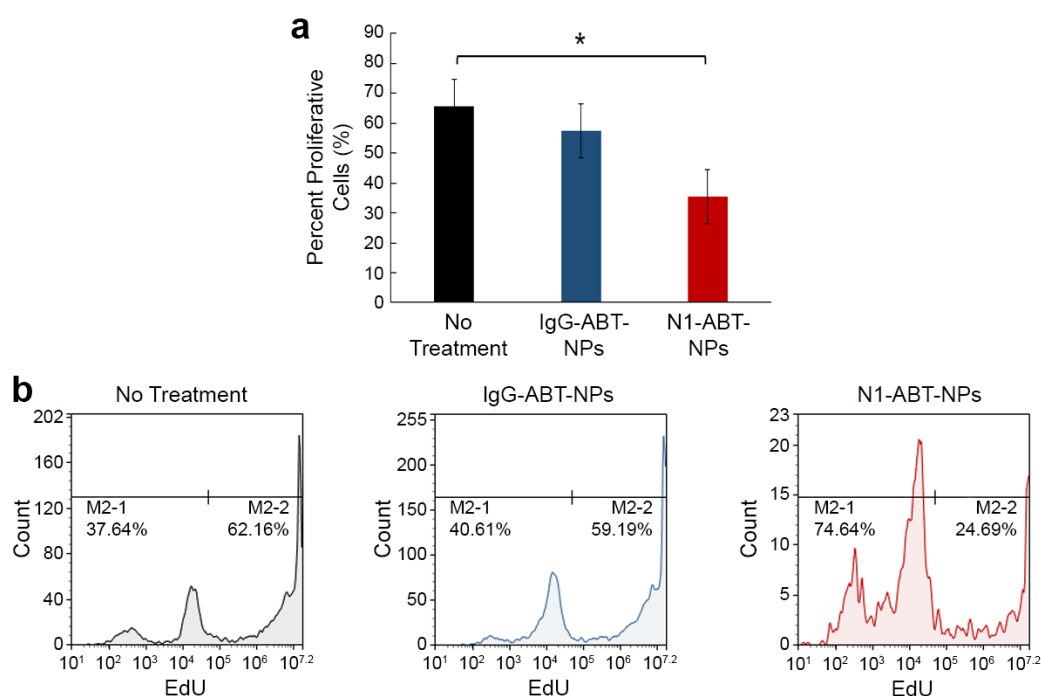


Figure 4.8: Analysis of the impact of N1-ABT-NPs on TNBC cell proliferation. (a) Percent proliferation of MDA-MB-231 TNBC cells that were untreated or exposed to IgG-ABT-NPs or N1-ABT-NPs. \* $p < 0.05$  (b) Representative flow cytometry histograms for EdU proliferation assay. Modified from Valcourt, *et al. ACS Nano* (2020); 14(3): 3378-3388. [230]

#### 4.3.4 N1-ABT-NPs Regulate Bcl-2 and Notch Signaling in TNBC Cells

To determine whether the enhanced therapeutic effect seen with N1-ABT-NPs is simply due to increased drug delivery or also a result of Notch signaling interference mediated by the antibodies (**Figure 4.9**), we evaluated the expression of Bcl-2 and Notch signaling targets in TNBC cells treated with N1-ABT-NPs or IgG-ABT-NPs using qRT-PCR and Western blotting.

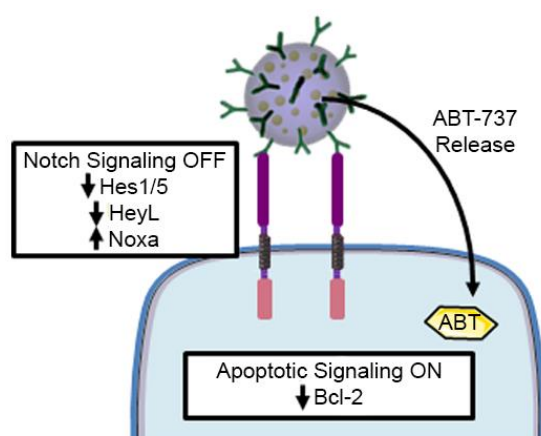


Figure 4.9: Scheme of proposed NP interaction with MDA-MB-231 TNBC cells. Upon cellular binding, N1-ABT-NPs suppress Notch signaling through antibody-mediated signal cascade interference and also release ABT-737 to inhibit Bcl-2 and activate apoptosis. Modified from Valcourt, *et al. ACS Nano* (2020); 14(3): 3378-3388. [230]

qRT-PCR shows that IgG-ABT-NPs reduce Bcl-2 mRNA expression by 59%, but have no significant effect on the expression of Noxa, Hes5, or HeyL, which are regulated by Notch signaling. This indicates that ABT-737 is successfully released from IgG-ABT-NPs to reduce Bcl-2 mRNA expression. N1-ABT-NPs expectedly knocked down Bcl-2 expression by 61%, but also reduced Hes5 expression by 42% and HeyL expression by 38%, and increased Noxa expression 2.4-fold (**Figure 4.10**).

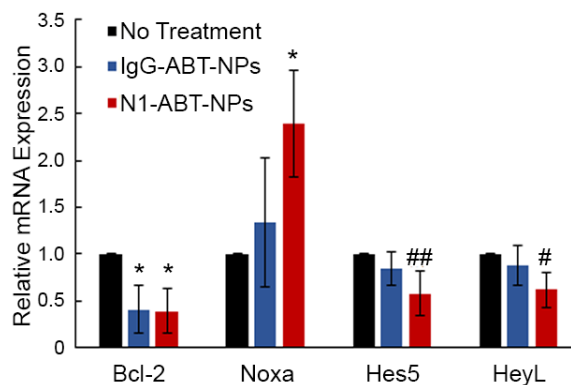


Figure 4.10: qPCR analysis of relative Bcl-2, Noxa, Hes5, and HeyL mRNA expression after treatment with IgG- or N1-ABT-NPs compared to control (untreated) cells. RPLPO was used as a control and relative mRNA expression in nanoparticle-treated groups is normalized to that of untreated cells. \* $p < 0.05$ , ## $p = 0.06$ , # $p = 0.07$  Modified from Valcourt, *et al. ACS Nano* (2020); 14(3): 3378-3388. [230]

Western blot analysis revealed similar results, as N1-ABT-NPs suppressed Bcl-2 (17%) and Hes1 (72%) protein expression, while IgG-ABT-NPs did not suppress these proteins (**Figure 4.11a**, representative bands in **Figure 4.11b**). We also probed for cleaved Notch-1 but did not observe a significant change in the expression of this protein. Altogether, the qRT-PCR and Western blot data confirm that N1-ABT-NPs can both inhibit Bcl-2 and effectively regulate the Notch signaling pathway.

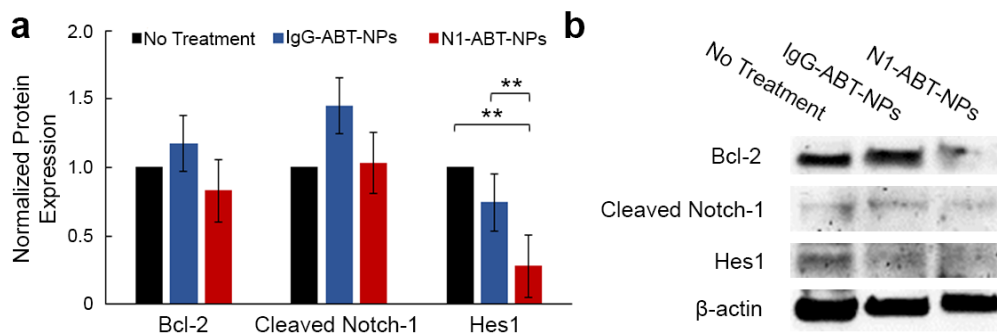


Figure 4.11: Examination of the effects of N1-ABT-NPs on Notch signaling and Bcl-2 expression in TNBC cells. (a) Quazi-quantitative analysis of Western blotting for normalized Bcl-2, cleaved Notch-1, and Hes1 protein expression.  $\beta$ -actin was used as a control and expression in nanoparticle-treated samples was normalized to expression in untreated cells.  $**p < 0.01$  (b) Representative Western blot bands for Bcl-2, cleaved Notch-1, Hes1, and  $\beta$ -actin protein levels. Modified from Valcourt, *et al. ACS Nano* (2020); 14(3): 3378-3388. [230]

#### 4.3.5 Notch-1 Functionalization Enhances Nanoparticle Tumor Accumulation and Retention *In Vivo*

After validating N1-ABT-NPs could inhibit TNBC cell viability through the expected molecular mechanisms *in vitro*, we next evaluated their ability to reduce tumor burden *in vivo* using a subcutaneous murine xenograft model. First, we investigated the tumor accumulation and retention of DiD-loaded NPs after intravenous injection into female nude mice bearing subcutaneous MDA-MB-231 tumors. This preliminary study, which monitored DiD signal in the tumors with an IVIS system over a period of 24 hours following tail vein injection of the treatments, demonstrates that N1-DiD-NPs show a greater overall fluorescence intensity within tumors than IgG-DiD-NPs at all time points (**Figure 4.12a**). In addition, the peak intensity in the tumor occurred at 6 hours for IgG-DiD-NPs, but at 12 hours for N1-DiD-NPs (**Figure 4.12a**, representative IVIS images in **Figure 4.12b**). These data

indicate that Notch-1 antibody functionalization increases both tumor accumulation and retention of NPs following intravenous administration.

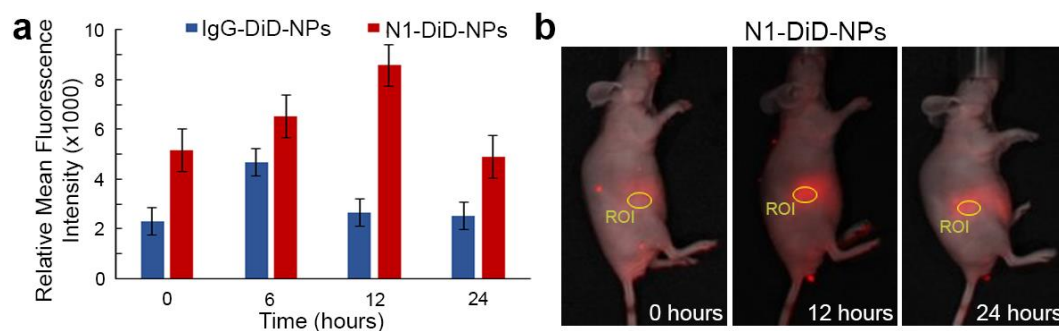


Figure 4.12: *In vivo* evaluation of tumor accumulation of N1-ABT-NPs. (a) Relative mean fluorescence intensity of DiD in subcutaneous MDA-MB-231 tumors in mice 0, 6, 12, and 24 hours post-intravenous injection of IgG-DiD-NPs or N1-DiD-NPs (n=6). (b) Representative fluorescence images of a mouse treated with N1-DiD-NPs at 0, 12, and 24 hours after injection. Circles indicate the region of interest (ROI) where fluorescence intensity was measured. Modified from Valcourt, *et al. ACS Nano* (2020); 14(3): 3378-3388. [230]

#### 4.3.6 N1-ABT-NPs Reduce Tumor Burden and Extend Survival *In Vivo*

We then evaluated whether N1-ABT-NPs could reduce tumor growth in a subcutaneous xenograft model. In a preliminary study to investigate the dosing regimen, eighteen mice were divided into three groups of six that were treated with saline, IgG-ABT-NPs, or N1-ABT-NPs. The mice were injected with saline or an equivalent volume of NPs at a dose of 10 mg ABT-737/kg once per week for three weeks, beginning when tumors were 5 mm in diameter. Tumor volume was measured three times per week, and the average percent change in tumor volume within each treatment group over one and three weeks is shown in **Figure 4.13**. Tumors in mice treated with N1-ABT-NPs shrank by 37% within one week, and after three weeks this

reduction in tumor volume was maintained at 44%. By comparison, mice treated with IgG-ABT-NPs and saline experienced tumor growth of 16% and 36%, respectively, within one week. By three weeks, the mean tumor volumes in the IgG-ABT-NP and saline treatment groups had grown by 65% and 58%, respectively (**Figure 4.13**). These data prompted us to perform a larger follow-up study in which treatments were administered twice per week.

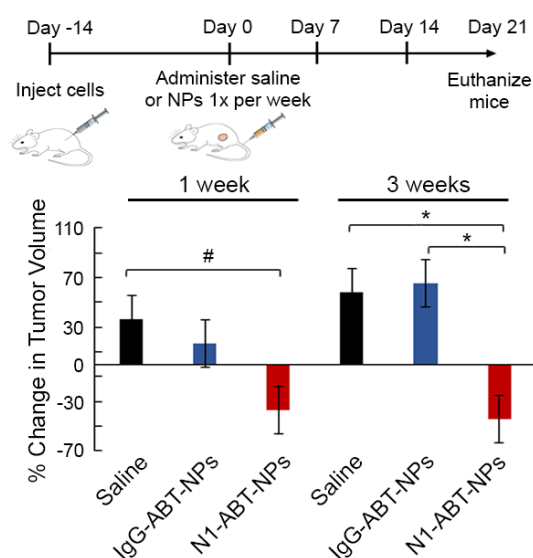


Figure 4.13: Average percent change in tumor volume (n=6 mice/group) after one and three weeks of treatment with saline, IgG-ABT-NPs, or N1-ABT-NPs at 10 mg ABT-737/kg once per week. #p<0.1, \*p<0.05 Modified from Valcourt, *et al. ACS Nano* (2020); 14(3): 3378-3388. [230]

In the subsequent therapeutic study, twenty-four tumor-bearing mice were divided into three groups of eight that were treated with saline, IgG-ABT-NPs, or N1-ABT-NPs. Over a 55-day treatment period, the mice received intravenous injections of the treatments at a dose of 10 mg ABT-737/kg twice per week (days indicated by

black arrows in **Figure 4.14**), and tumor volume was measured three times per week. Mice were euthanized when tumor volume reached 10 mm in diameter, when body weight decreased by more than 20%, or when the study ended at day 55 (whichever came first). The Kaplan-Meier survival curves for each group are shown in **Figure 4.14**. At the end of the study, N1-ABT-NP treated mice exhibited an 88.9% survival rate, which was substantially improved over the 46.9% and 44.4% survival in the IgG-ABT-NP and saline treated groups, respectively (**Figure 4.14**).

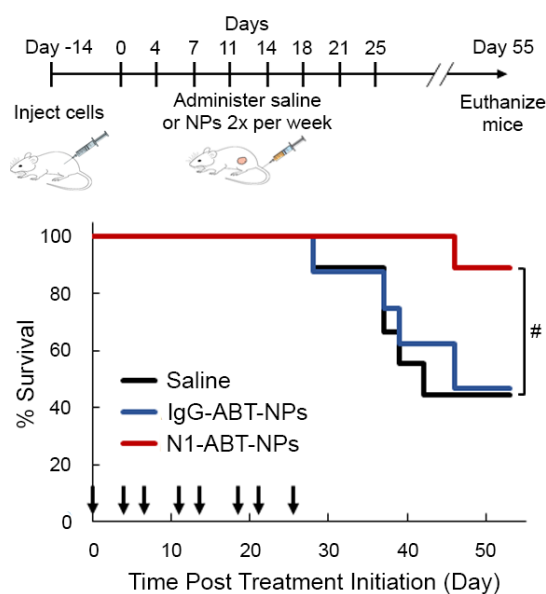


Figure 4.14: Kaplan-Meier survival curves for mice bearing subcutaneous MDA-MB-231 TNBC tumors that were treated intravenously with saline, IgG-ABT-NPs, or N1-ABT-NPs at 10 mg ABT-737/kg twice per week for four weeks (n=8 mice/group). Black arrows on the x-axis indicate days of treatment. #p=0.10 Modified from Valcourt, *et al. ACS Nano* (2020); 14(3): 3378-3388. [230]

We also evaluated the impact of each treatment on mouse weight throughout the therapeutic study (**Figure 4.15a**), and on the morphology of major organs at the conclusion of the study using H&E staining (**Figure 4.15b**). Mice treated with N1-ABT-NPs did not experience any significant change in body weight or any notable changes in tissue morphology compared to saline treated mice. In contrast, two mice treated with IgG-ABT-NPs demonstrated adverse effects and were euthanized due to severe weight loss or a distended abdomen caused by an enlarged liver and spleen. These data demonstrate that providing targeted delivery of ABT-737 to TNBC tumors, such as via Notch-1 functionalized antibodies, is important to minimize its adverse effects. Overall, our *in vivo* studies indicate that N1-ABT-NPs are exciting tools for targeted inhibition of Bcl-2 and Notch signaling in TNBC cells that can effectively reduce tumor burden in mice with minimal side effects.

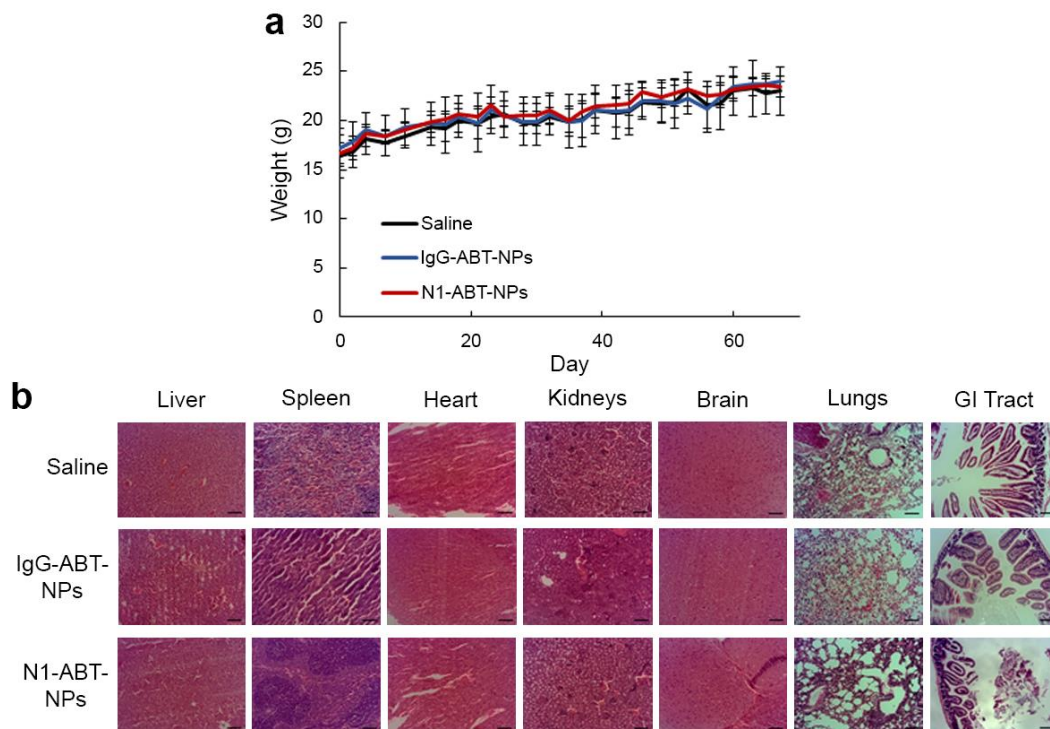


Figure 4.15: Mouse weight and major organ histopathology following treatment with N1-ABT-NPs. (a) Average weight of mice bearing subcutaneous MDA-MB-231 tumors that were treated with saline, IgG-ABT-NPs, or N1-ABT-NPs twice weekly for 8 total injections (n=8 mice/group). (b) Hematoxylin and eosin staining of representative major organs excised from tumor-bearing mice treated with saline, IgG-ABT-NPs, or N1-ABT-NPs twice weekly for four weeks as described in part (a). Scale bars = 100  $\mu$ m. Reproduced from Valcourt, *et al. ACS Nano* (2020); 14(3): 3378-3388. [230]

#### 4.3.7 Discussion

In this chapter, we present ABT-737-loaded, Notch-1 antibody functionalized PLGA NPs as potent regulators of Bcl-2 and Notch signaling that can effectively treat TNBC. These N1-ABT-NPs preferentially interact with TNBC cells that overexpress Notch-1 receptors *in vitro*, reducing cell viability and proliferation by molecular mechanisms including inhibition of Bcl-2, suppression of Hes5, HeyL, and Hes1, and

amplification of Noxa. *In vivo*, N1-ABT-NPs exhibit enhanced accumulation in subcutaneous TNBC tumors versus non-targeted NPs and yield improved tumor growth inhibition and extended animal survival while minimizing adverse effects. With additional development, these N1-ABT-NPs may be a promising new arsenal in the fight against TNBC.

Future studies that build on this work should more extensively examine these NPs' biocompatibility and efficacy, particularly in mice with an intact immune system. In this study, we used human MDA-MB-231 cells to induce subcutaneous tumors in nude mice, but other TNBC models may more accurately reflect the potential impact of these NPs in humans. It will be important to consider, however, that alternate TNBC models, like murine 4T1 cells, may have varying expression levels of Notch-1 receptors and ligands that will impact the NP-cell interactions and effects. [248] Besides examining different TNBC cell lines, researchers should also study the effectiveness of N1-ABT-NPs when tumors are positioned orthotopically rather than subcutaneously, as tumor location in the body may impact NP accumulation and retention.

While there is evidence showing that Notch-1 is widely overexpressed across human TNBC [56] and correlates with poor prognosis [249], it is classically considered to play the largest role in early stages of tumor development and in cancer stem cells. [250, 251] Sethi and Kang have expanded upon this role and demonstrated that Notch signaling facilitates bone metastasis in later stages of tumor progression [251], but its role in the primary tumor at these later stages has not been extensively explored. In this work, we evaluated the impact of N1-ABT-NPs on tumors in a relatively early stage, about 5 mm in diameter. Future studies should examine the

expression of the Notch-1 receptor in tumors of various sizes and determine the therapeutic efficacy of these NPs when treatment is initiated at later stages.

In addition to demonstrating the value of N1-ABT-NPs in targeting and regulating the Notch signaling pathway in TNBC, we have also shown that this platform can effectively regulate Bcl-2 through the delivery of ABT-737. Bcl-2 is a promising therapeutic target for many cancers, [61, 252] thus extending the potential applicability of this NP formulation. The platform we have developed can be easily adapted to target other cancer types by exchanging the targeting antibody on the surface of the NPs. It is important to consider, however, that not all antibodies are antagonistic. Thus, targeting alternate receptors by exchanging the antibody will not automatically confer the same increase in therapeutic efficacy as was shown here.

#### **4.4 Conclusions**

Overall, we have demonstrated that ABT-737-loaded, Notch-1 antibody functionalized PLGA NPs can target TNBC cells and effectively regulate Bcl-2 and Notch signaling to induce cell death *in vitro*. In addition, we have shown that these NPs can accumulate in tumors and reduce tumor burden to extend survival in a murine model. These dual antibody/drug nanocarriers are thus a promising alternative treatment strategy for aggressive cancers like TNBC that are driven by overactive Bcl-2 and Notch signaling. With additional development and implementation, these NPs may substantially improve patient outcomes.

## Chapter 5

### CO-DELIVERY OF NOTCH-1 ANTIBODIES AND MIR-34A FOR GENE REGULATION

The work presented in this chapter is adapted from a manuscript by Valcourt DM, and Day ES, which is in revision.

#### 5.1 Introduction

Triple-negative breast cancer (TNBC) is an aggressive subtype of breast cancer that accounts for 15-25% of all breast cancer cases. [8, 193] Its characteristic lack of expression of common receptors present on other subtypes of breast cancer (the estrogen, progesterone, and human epidermal growth factor 2 receptors) leaves TNBC unsusceptible to current targeted or hormonal therapies, leading to high mortality and recurrence rates. [8, 9, 193] In this chapter we introduce a promising alternative treatment strategy for TNBC that exploits its overexpression of Notch-1 receptors [54, 58, 232] to enable combination antibody-mediated signal cascade interference and microRNA (miRNA) replacement therapy [253].

miRNA replacement therapy involves the delivery of exogenous miRNA mimics to target cells to regulate gene expression. Upon cell entry, miRNA mimics bind specific messenger RNA (mRNA) molecules with either perfect or imperfect complementarity to induce mRNA degradation or translational repression, respectively. [5] In TNBC, the tumor suppressor miRNA miR-34a is frequently downregulated or deleted, leading to enhanced cell survival, proliferation, and migration. [84, 89] Delivering miR-34a mimics to these cells can effectively regulate

downstream expression of a broad network of genes, resulting in phenotypic changes such as reduced proliferation and migration and onset of apoptosis or senescence. [89, 90, 254] Unfortunately, naked miRNA mimics cannot be used clinically as they experience significant barriers to delivery. [5] For effective miRNA replacement therapy, miRNA mimics must: avoid early clearance and degradation in the bloodstream, cross blood vessel walls, travel through the extracellular matrix of the tumor microenvironment, enter the target cell, escape endosomes, and load into the RNA-induced silencing complex (RISC) to enable gene regulation. [5] In this work, we encapsulate miR-34a mimics in poly(lactic co-glycolic acid) (PLGA) nanoparticles (NPs) to overcome these delivery challenges.

Several NP formulations have been developed to deliver miR-34a mimics to TNBC. [234, 255–257] Our group has previously created two layer-by-layer (LbL) NP systems that utilize either gold nanoshell [255] or PLGA [256] cores for TNBC therapy. Gold nanoshell-based LbL NPs effectively regulated the downstream miR-34a targets SIRT1 and Bcl-2 in MDA-MB-231 TNBC cells *in vitro* to reduce cell viability and proliferation. [255] Similarly, PLGA-based LbL NPs were able to deliver miR-34a to the cytosol of MDA-MB-231 cells and suppress the expression of cyclin D1 (CCND1), Notch-1, Bcl-2, survivin, and MDR1 to inhibit cell proliferation and induce cell cycle arrest. [256] Xia *et al* have also developed a LbL NP formulation for miR-34a delivery to TNBC cells using nanodiamond, protamine, and folic acid constructs. [257] This system provides targeted delivery to MDA-MB-231 TNBC cells due to the cells' overexpression of folate receptors, and was shown to inhibit cell proliferation and migration and induce cell death *in vitro*. Additionally, these NPs reduced Fra-1 expression *in vivo*, inhibiting tumor growth in a subcutaneous murine

model. [257] Finally, Zeng and colleagues created hyaluronic acid-chitosan NPs co-encapsulating miR-34a and doxorubicin (DOX) and showed these NPs could suppress the expression of Bcl-2 to enhance the therapeutic efficacy of DOX. [234] They also demonstrated that these NPs could reduce TNBC cell migration by regulating Notch-1 signaling. [234] Together, these studies demonstrate the potential for enabling targeted delivery of miR-34a mimics in combination with other therapeutic modalities as an alternative treatment strategy for TNBC. Intriguingly, several of these studies<sup>14,16</sup> and others [92, 258, 259] have shown that miR-34a delivery can regulate Notch signaling, showing there is crosstalk between the pathways and suggesting that combining miR-34a delivery with Notch inhibition may be a potent therapeutic approach. Here, we present PLGA NPs loaded with miR-34a mimics and functionalized with Notch-1 antibodies as a system that can simultaneously regulate Notch-1 signaling and enable tumor suppressive gene regulation via miR-34a delivery.

In this work, we coated miR-34a-loaded NPs with Notch-1 antibodies to produce N1-34a-NPs that not only target miR-34a delivery to TNBC cells, but also inhibit the Notch signaling pathway, which is aberrantly expressed in TNBC. [54, 58] The overexpression of Notch-1 receptors on the surface of TNBC cells serves as a resource for NP attachment, thus facilitating NP retention in the tumor microenvironment. [245] In this chapter, we show that after binding TNBC cells, N1-34a-NPs can prevent Notch signaling activation by locking Notch-1 receptors in a non-responsive state and blocking receptor-ligand interactions. Critically, our group and others have previously demonstrated that antibody-NP conjugates are much more effective than freely delivered antibodies because antibody-NP conjugates exhibit multivalent binding that yields enhanced signal cascade interference. [155, 156] Thus,

by functionalizing our NP formulation with Notch-1 antibodies, we can enhance the NPs' interaction with TNBC cells while simultaneously inhibiting Notch signaling and facilitating miR-34a delivery to the desired cells. We present the results of *in vitro* studies that confirm N1-34a-NPs can effectively regulate both Notch signaling targets and miR-34a downstream targets in TNBC cells to induce senescence and reduce cell proliferation and migration. These exciting observations provide evidence warranting further investigation of this system as an effective treatment for TNBC.

## 5.2 Materials and Methods

### 5.2.1 Synthesis of N1-34a-NPs

miRNA loaded PLGA NPs were synthesized using a double emulsion method. [260] Briefly, PLGA (Lactel, 50:50 carboxylic acid terminated, 0.55-0.75 dL/g) was dissolved in acetone (VWR) at 2 mg/mL. miR-Co and miR-34a (Dharmacon, stored in duplex buffer at 20  $\mu$ M; miRNA sequences listed in **Table 5.1**) were mixed separately with a 1% poly(vinyl) alcohol (PVA) solution and then added dropwise to the PLGA in acetone at a concentration of 0.2 nmol/mg PLGA and stirred for 5 minutes to allow for homogenization. This mixture was subsequently added dropwise to a 0.1% PVA solution in a 1:3 volume ratio while stirring. This secondary emulsion continued to stir for 2 hours, letting the acetone evaporate. The NPs were then purified using centrifugal filtration (Millipore, 50k MWCO, 4200 g, 15 min) to remove unencapsulated miRNA and excess solvent. Rabbit anti-human IgG or Notch-1 antibodies were conjugated to the surface of the bare NPs using 1-ethyl-3-(3-dimethylaminopropyl)carbodiimide (EDC) chemistry. [220, 247] Briefly, after centrifugal filtration, miRNA-loaded NPs were suspended in 4 mM EDC and 4 mM n-

hydroxysulfosuccinimide sodium salt (sulfo-NHS) and incubated on a rocker at 4°C. IgG or Notch-1 antibodies were then added to the solution for further incubation at 4°C. To remove free antibodies from solution after conjugation, the NPs were purified using trans-flow filtration (Spectrum, 300 kDa MWCO). NPs were freshly prepared and used immediately for experiments.

Table 5.1: Sequences of miR-Co and miR-34a. Reproduced from Valcourt DM, Day ES, Manuscript in revision.

miRNA	Sense Strand	Antisense Strand
miR-34a	ACAACCAGCUAAGACACUGCCA	UGGCAGUGUCUUAGCUGGUUGU
miR-Co	AAGUGAUCAAGCACCGAAGAG	CUCUUCGGUGCUUGAUCACUU

### 5.2.2 Characterization of N1-34a-NPs

Purified NPs were characterized by DLS and zeta potential measurements on a Litesizer500 instrument (AntonPaar) before and after antibody conjugation, and the reported intensity-based hydrodynamic diameter is the average of three measurements. miRNA encapsulation was quantified using an OliGreen assay. During NP synthesis, all filtrate containing unencapsulated miRNA was concentrated and analyzed alongside a standard curve of known miRNA concentration.

Antibody loading on the NPs was quantified using a solution-based ELISA modified from a previously published protocol. [191] IgG-Co-NPs, IgG-34a-NPs, N1-Co-NPs, N1-34a-NPs, bare miR-Co-NPs, or bare miR-34a-NPs were incubated with 10 µg/mL horseradish peroxidase (HRP)-conjugated anti-rabbit IgG antibodies for 1 hour at room temperature. Unbound secondary antibodies were removed through centrifugation and the samples were suspended in 3% bovine serum albumin in phosphate buffered saline (PBS). The samples were then developed in 3,3',5,5'-

tetramethylbenzidine solution (TMB core; Bio-Rad) for 15 seconds before the reaction was stopped with 2 mM sulfuric acid. The absorbance was then measured at 450 nm on a Synergy H1 plate reader and compared to a standard curve of known HRP-IgG concentration to calculate the quantity of IgG or Notch-1 antibodies conjugated per mg of PLGA.

### **5.2.3 Cell Culture**

MDA-MB-231 TNBC cells (ATCC) were cultured in Dulbecco's Modified Eagle's Medium (DMEM, VWR) supplemented with 10% fetal bovine serum (FBS; Gemini Bio Products) and 1% penicillin-streptomycin (pen-strep; VWR). The cultures were maintained at 37°C in a 5% CO<sub>2</sub> humidified environment. When cells reached 80-90% confluency in T75 cell culture flasks, they were passaged or plated by detaching the cells from the flask using Trypsin-EDTA (ThermoFisher) and then counting cells with a hemocytometer.

### **5.2.4 Cellular Binding and Uptake**

To analyze cellular binding and uptake of antibody-functionalized particles, PLGA NPs were loaded with miR-Co tagged with Cy5 (Dharmacon; excitation 647 nm/emission 665 nm) and functionalized as described above to create IgG-Cy5-NPs and N1-Cy5-NPs. For flow cytometric analysis of cellular binding and uptake, cells were plated at  $3 \times 10^4$  cells per well (MDA-MB-231 cells) in a 24-well plate and incubated overnight. Cells were then treated with IgG-Cy5-NPs and N1-Cy5-NPs at 50 nM miRNA or were left untreated and incubated for 0, 1, 4, 8, 12, 16, or 24 hours prior to rinsing with PBS. The cells were then lifted off the plate with Trypsin-EDTA and resuspended in PBS. All cell suspensions were analyzed using an Acea Novocyte

2060 flow cytometer with the APC (excitation, 640 nm; emission, 675/30 nm) channel. Density plots showing forward and side scatter data were used to create a primary gate for cells, excluding debris, prior to analyzing Cy5 content. Flow cytometric analysis was performed in triplicate.

### 5.2.5 Quantitative Real-Time Polymerase Chain Reaction

To analyze the effects of IgG-Co-NPs, IgG-34a-NPs, N1-Co-NPs, and N1-34a-NPs on gene expression in TNBC cells by qRT-PCR, cells were seeded at  $1.5 \times 10^5$  cells per well in a 6-well plate and incubated overnight. Cells were then treated with NPs at 200 nM miRNA for 48 hours. At the conclusion of the treatment period, cells were rinsed with PBS and mRNA was extracted using a Bioline Isolate II RNA Mini Kit. qRT-PCR was then performed using SensiFAST SYBR One-Step Master Mix on a LightCycler 96 (Roche) and gene expression was normalized to that of GUSB. These experiments were performed in triplicate and analyzed using a one-way ANOVA with post-hoc Tukey. Primer sequences are listed in **Table 5.2**.

Table 5.2: Primer sequences used for qPCR. Reproduced from Valcourt DM, Day ES, Manuscript in revision.

Gene	Forward Sequence	Reverse Sequence
GUSB	CTTTTCTTAGCGCCGCAG	GGCCTGACTCCCACA
Bcl-2	GACTTCTCCCGCCGCTACC	CCCAGTTCACCCCGTCCCT
Survivin	CTCAAGGACCACCGCATCTC	TTACAGGCGTAAGCCACCGT
CCND1	CCTGTCCTACTACCGCCTCA	CAGTCCGGGTCACACTTGA
Notch-1	CACTGTGGGCGGGTCC	GTTGTATTGGTTCGGCACCAT
MDR1	GCTCAAGTTAAAGGGGCTAT	GCCAACCATAGATGAAGGAT
Hes5	CCGGTGGTGGAGAAGATGCG	GCGACGAAGGCTTTGCTGTG

### 5.2.6 Western Blotting

To further evaluate the effects of N1-34a-NPs on Bcl-2, CCND1, Notch-1, and Hes1 by Western blotting, MDA-MB-231 cells were plated at  $1.5 \times 10^5$  cells per well in a 6-well plate and incubated overnight. Cells were then treated as described for qRT-PCR. After 48 hours of treatment with NPs, the cells were rinsed with PBS and lysed in RIPA buffer supplemented with Halt Protease Inhibitor in a 1:50 volume ratio. After removing membrane debris through centrifugation, the extracted protein was quantified using a DC Protein Assay (BioRad), and 10  $\mu$ g of protein was separated on 4-12% Bis-tris gels at 135V for 60 minutes. Then, the protein was transferred to a 0.2 micron nitrocellulose membrane for 10 minutes using a Power Blotter System (Invitrogen). The membrane was subsequently blocked for 60 minutes in 5% milk in tris buffered saline with 0.1% Tween-20 (TBS-T) and then incubated with rabbit anti-human Bcl-2 (ProteinTech; 1:1000), CCND1 (Cell Signaling Technology; 1:250), Notch-1 (Cell Signaling Technology; 1:500), and Hes1 (Cell Signaling Technology; 1:500) antibodies in 5% milk in TBS-T overnight at 4°C. Mouse anti-human  $\alpha$ -tubulin antibody (Cell Signaling Technology; 1:20,000) was used as the normalization control. After incubation in primary antibodies, membranes were washed 3x in TBS-T and incubated with HRP-anti-rabbit or mouse IgG antibody (VWR; 1:25,000) in 5% milk in TBS-T for 1 hour at room temperature. Membranes were then washed 2x in TBS-T and 2x in TBS (without Tween-20) and protein bands were visualized using a Pierce enhanced chemiluminescence detection solution (ECL, Thermo Scientific). Band densities were quantified in ImageJ and Bcl-2, CCND1, Notch-1, and Hes1 densities were normalized to that of  $\alpha$ -tubulin prior to further normalizing treatment groups to the control untreated group. The data shown represent the average band

density across three trials and were analyzed using a one-way ANOVA with post-hoc Tukey.

### **5.2.7 Cellular Senescence**

To determine the effect of IgG-Co-NPs, IgG-34a-NPs, N1-Co-NPs, and N1-34a-NPs on cellular viability through a SA $\beta$ Gal senescence assay, cells were seeded at  $3 \times 10^5$  cells per well in a 6-well plate and incubated overnight. Cells were then treated with NPs for 24 hours and senescence was evaluated using a Senescence-Associated  $\beta$ -Galactosidase (SA $\beta$ Gal) Kit (Cell Signaling Technology) per the manufacturer's instructions. Stained cells were imaged on a Zeiss Axioobserver Z1 microscope equipped with a color camera.

### **5.2.8 Cell Proliferation**

To analyze the effect of IgG-Co-NPs, IgG-34a-NPs, N1-Co-NPs, and N1-34a-NPs on cellular proliferation via an EdU assay, cells were seeded at  $1.0 \times 10^5$  cells per well in a 12-well plate and incubated overnight. Cells were then treated with NPs at 200 nM miRNA for 48 hours. At 16 hours prior to the end of the treatment period, the cells were spiked with EdU at 10  $\mu$ M. Cells were then prepared per the manufacturer's instructions modified for a single cell suspension. Briefly, cells were fixed in 4% formaldehyde and permeabilized with 0.5% Triton X-100. They were subsequently incubated in the Click-iT reaction cocktail, washed in PBS, and examined on an Acea Novocyte 2060 flow cytometer with the FITC (excitation, 488 nm; emission, 530/30 nm) channel. Density plots showing forward and side scatter data were used to create a primary gate for cells, excluding debris, prior to analyzing EdU-labeling azide content.

Flow cytometric analysis was performed in quadruplicate and statistical analysis was performed using a one-way ANOVA with post-hoc Tukey.

### **5.2.9 Cell Migration**

To evaluate the impact of IgG-Co-NPs, IgG-34a-NPs, N1-Co-NPs, and N1-34a-NPs on cellular migration using a transwell invasion assay, MDA-MB-231 GFP-expressing cells were plated at  $1.5 \times 10^4$  cells per well in a 96-well plate and incubated overnight. Cells were then treated with NPs at 200 nM for 48 hours, at which time the cells were washed with PBS and lifted off the plate using 0.25% trypsin-EDTA. The cells were pelleted (0.3 rcf, 5 minutes) and resuspended in DMEM (without supplements) at 25,000 cells per mL. Cells were then seeded in transwell inserts (Corning) at 5,000 cells per 200  $\mu$ L and 700  $\mu$ L of DMEM (with FBS and PS supplements) was added beneath the insert in a 24-well black walled, glass bottom plate (Cellvis). The transwell samples were imaged on a Zeiss Axioobserver Z1 microscope after 48 hours. ImageJ software was subsequently used to analyze the number of cells migrated within the entire transwell and the data presented represent the average of three trials normalized to the IgG-Co-NP group. Statistical analysis was performed using a one-way ANOVA with post-hoc Tukey.

## **5.3 Results and Discussion**

### **5.3.1 Characterization of Antibody and miRNA Loading in N1-34a-NPs and Interaction with TNBC Cells**

N1-34a-NPs and control NPs carrying either non-silencing miRNA (miR-Co), nonspecific IgG antibodies, or both were synthesized as described in the Methods and characterized using dynamic light scattering (DLS), zeta potential, OliGreen, and

enzyme-linked immunosorbent assay (ELISA) measurements, which demonstrated that IgG or Notch-1 antibodies were successfully conjugated to the surface of miR-Co- or miR-34a-loaded NPs. Prior to antibody conjugation, miRNA-loaded NPs had a hydrodynamic diameter and zeta potential of approximately 140 nm and  $-40$  mV, respectively, with 0.37 nmol miR-Co and 0.36 nmol miR-34a encapsulated per 2 mg of PLGA (**Figure 5.1**). After IgG or Notch-1 antibody conjugation, the NPs' hydrodynamic diameter increased by approximately 20 nm and the zeta potential increased to around  $-8$  mV, which indicates successful antibody attachment (**Figure 5.1a**). Antibody attachment was confirmed by ELISA measurements, which showed the NPs contained approximately 4.6  $\mu$ g of antibodies per mg of PLGA. OliGreen assays indicated that approximately 0.01 nmol miRNA was lost from the NPs during the antibody functionalization procedure, leaving around 0.35 nmol miRNA encapsulated per 2 mg PLGA (**Figure 5.1b**). Altogether, these data demonstrate that miRNA can be successfully loaded in antibody-functionalized PLGA NPs.

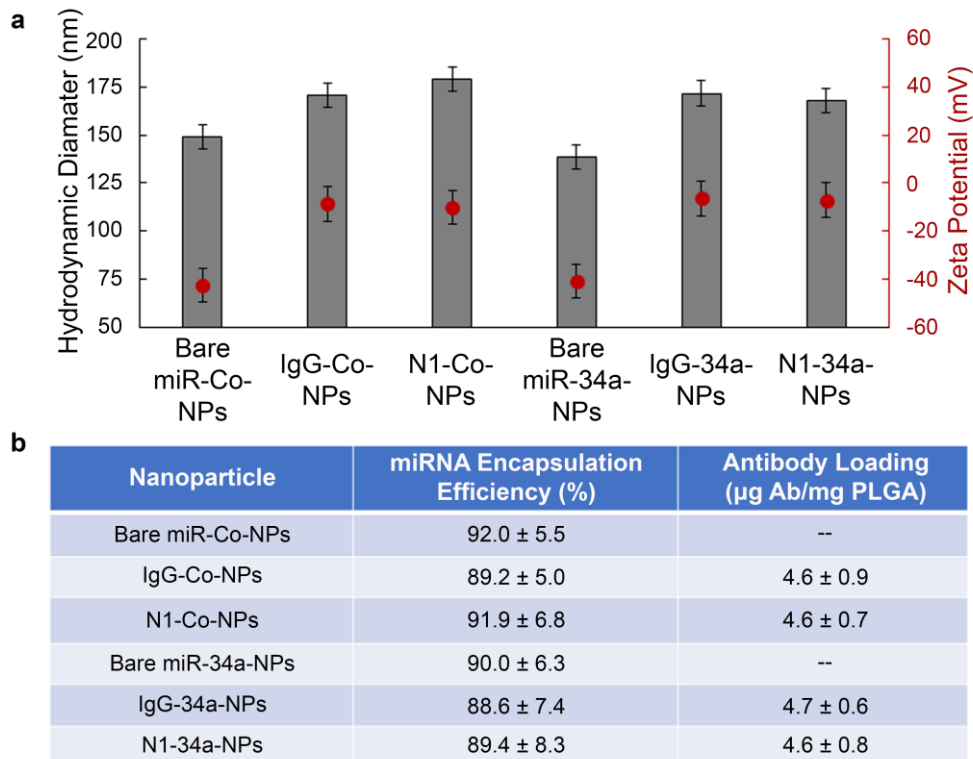


Figure 5.1: Characterization of N1-34a-NPs. (a) Hydrodynamic diameter and zeta potential of bare miR-Co-NPs, bare miR-34a-NPs, IgG-Co-NPs, IgG-34a-NPs, N1-Co-NPs, and N1-34a-NPs. Error bars indicate standard error. (b) Encapsulation efficiency of miRNA and loading of antibodies on the different nanoparticle formulations used in this study. Modified from Valcourt DM, Day ES, Manuscript in revision.

Following NP synthesis and characterization, we evaluated the interaction of Notch-1 and IgG antibody-conjugated NPs with MDA-MB-231 TNBC cells using flow cytometry. For these studies, the NPs were loaded with Cy5-tagged miR-Co in order to facilitate fluorescence analysis of NP delivery to cells. The cells were treated with IgG-Cy5-NPs or N1-Cy5-NPs at doses of 50 nM miRNA for 1, 4, 8, 12, 16, or 24 hours, then the Cy5 signal in the cells was analyzed by flow cytometry. These data

demonstrate that N1-34a-NPs exhibit a time-dependent interaction with MDA-MB-231 TNBC cells (**Figure 5.2**).

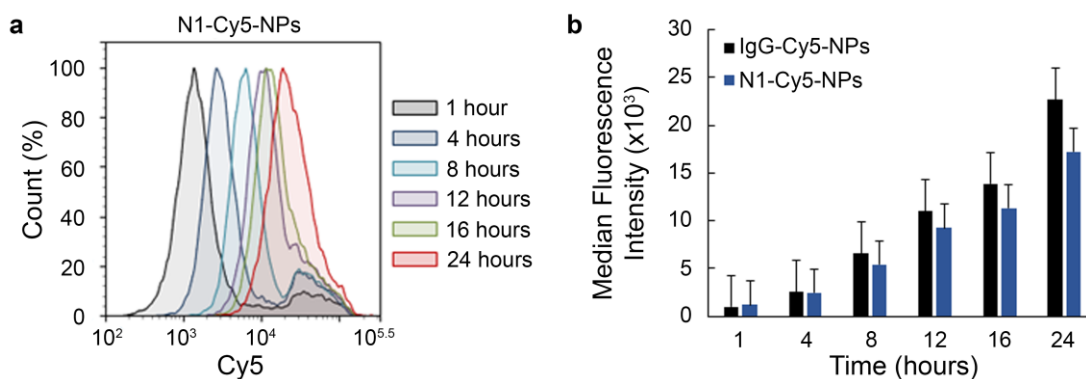


Figure 5.2: Evaluation of nanoparticle binding to MDA-MB-231 cells. (a) Representative flow cytometry histogram of MDA-MB-231 TNBC cells exposed to N1-Cy5-NPs for increasing amounts of time. (b) Median Cy5 fluorescence intensity of MDA-MB-231 TNBC cells treated with IgG-Cy5-NPs or N1-Cy5-NPs for different amounts of time as measured by flow cytometry. Error bars indicate standard error. Modified from Valcourt DM, Day ES, Manuscript in revision.

### 5.3.2 N1-34a-NPs Regulate Notch Signaling and Downstream miR-34a Targets

To determine the influence of N1-34a-NPs on downstream Notch and miR-34a signaling (**Figure 5.3**), we evaluated the expression of miR-34a targets (Bcl-2, survivin, CCND1, Notch-1, MDR1) and Notch signaling targets (Hes1, Hes5) in TNBC cells treated with IgG-Co-NPs, IgG-34a-NPs, N1-Co-NPs, and N1-34a-NPs at 200 nM miRNA using quantitative real time polymerase chain reaction (RT-PCR) and Western blotting.

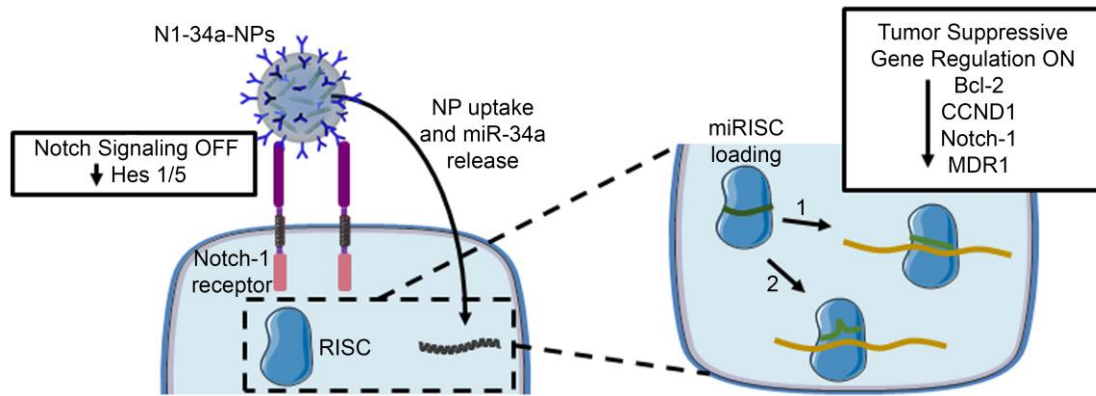


Figure 5.3: Scheme of posited nanoparticle interaction with MDA-MB-231 TNBC cells. Upon cellular binding and uptake, N1-34a-NPs inhibit downstream Notch signaling through antibody-mediated signal cascade interference and also deliver miR-34a, which reduces the expression of several genes by guiding the RNA induced silencing complex (miRISC) to targeted mRNA sequences with perfect (1) or imperfect (2) complementarity, resulting in mRNA degradation or translational repression. Modified from Valcourt DM, Day ES, Manuscript in revision.

The qRT-PCR data demonstrate that control IgG-Co-NPs, IgG-34a-NPs, and N1-Co-NPs have minimal impact on downstream mRNA expression. In contrast, N1-34a-NPs substantially suppressed Bcl-2 by 32%, survivin by 41%, CCND1 by 45%, Notch-1 by 46%, MDR1 by 31%, and Hes5 by 73% (**Figure 5.4a**). Western blot analysis revealed similar results, as N1-34a-NPs reduced Bcl-2 expression by 29%, CCND1 by 30%, Notch-1 by 41%, and Hes1 by 40% (**Figure 5.4b and 5.4c**). Together, these qRT-PCR and Western blot data indicate that N1-34a-NPs can regulate both miR-34a downstream targets and the Notch signaling pathway.

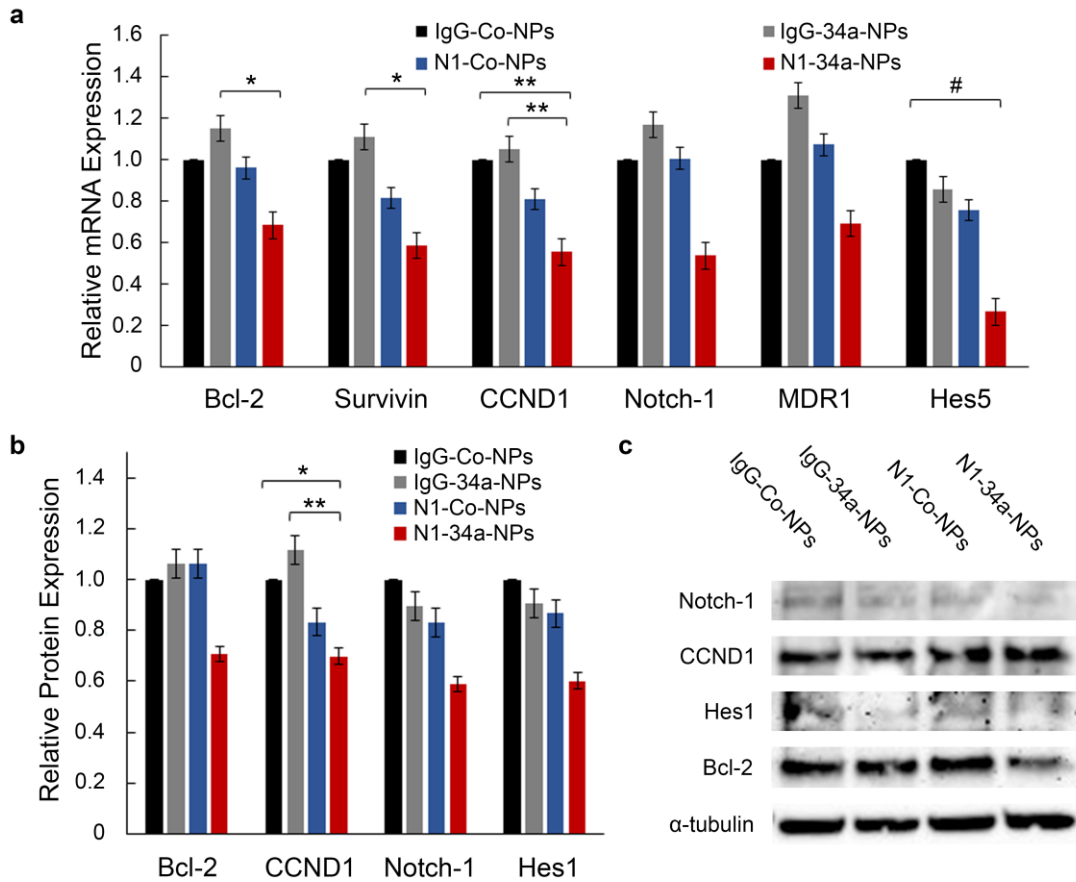


Figure 5.4: Evaluation of nanoparticle-mediated gene regulation. (a) qPCR analysis of relative Bcl-2, survivin, CCND1, Notch-1, MDR1, and Hes5 mRNA expression after treatment with IgG-Co-NPs, IgG-34a-NPs, N1-Co-NPs, or N1-34a-NPs. GUSB was used as a control and relative mRNA expression is normalized to that of cells treated with IgG-Co-NPs. Error bars indicate standard error. # $p < 0.1$ , \* $p < 0.05$ , \*\* $p < 0.01$  (b) Quasi-quantitative analysis of Western blotting for normalized Bcl-2, CCND1, Notch-1, and Hes1 protein expression. A-tubulin was used as a control and expression was normalized to expression in cells treated with IgG-Co-NPs. Error bars indicate standard error. \* $p < 0.05$ , \*\* $p < 0.01$  (c) Representative Western blot bands for Bcl-2, CCND1, Notch-1, Hes1, and  $\alpha$ -tubulin protein levels. Bands are from a single blot that was stripped and probed for multiple targets. Modified from Valcourt DM, Day ES, Manuscript in revision.

### 5.3.3 N1-34a-NPs Induce Senescence and Reduce TNBC Cell Proliferation and Migration *In Vitro*

We further investigated the impact of IgG-Co-NPs, IgG-34a-NPs, N1-Co-NPs, and N1-34a-NPs on TNBC cell viability and function using a senescence-associated  $\beta$ -galactosidase (SA $\beta$ Gal) assay, an EdU proliferation assay, and a transwell invasion assay. We selected these assays because miR-34a and Notch signaling have been highly implicated in the regulation of cell senescence [84, 261–263], proliferation [261, 263–265], and migration [84, 261, 264, 265]. The SA $\beta$ Gal assay showed that N1-34a-NPs induce  $\beta$ -galactosidase activity in MDA-MB-231 TNBC cells after a 24-hour treatment period, indicating an onset of senescence (**Figure 5.5**).

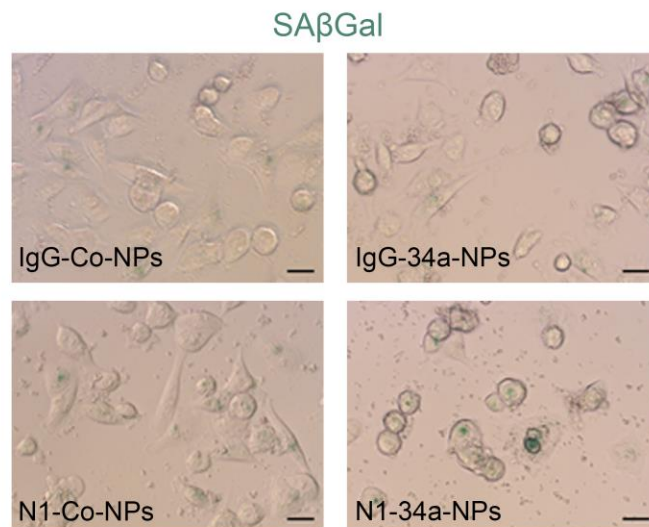


Figure 5.5: Representative images of SA $\beta$ Gal assay of MDA-MB-231 cells treated with IgG-Co-NPs, IgG-34a-NPs, N1-Co-NPs, or N1-34a-NPs. Green color indicates  $\beta$ -galactosidase activity. Scale bars = 50  $\mu$ m. Modified from Valcourt DM, Day ES, Manuscript in revision.

We also evaluated the effect of these NPs on cell proliferation after a 48-hour treatment period using an EdU assay. The results demonstrate that N1-Co-NPs can reduce cell proliferation by 13%, which we attribute to the Notch inhibition mediated through the Notch-1 antibodies on the NPs. Excitingly, N1-34a-NPs have an enhanced effect on cell proliferation, as they reduce EdU-positive cells by 26%, which is double the inhibition observed for NPs carrying only Notch-1 antibodies (**Figure 5.6**).

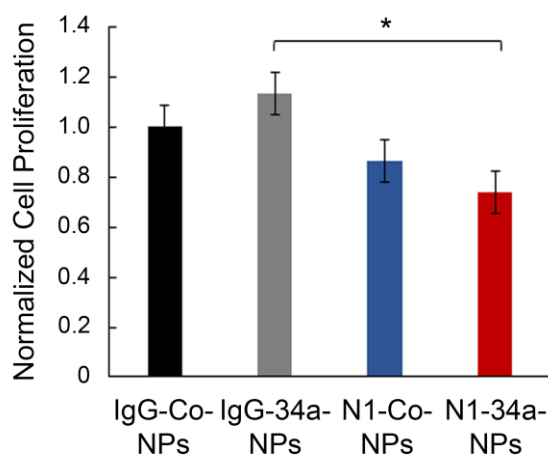


Figure 5.6: Percent proliferation of MDA-MB-231 cells treated with IgG-Co-NPs, IgG-34a-NPs, N1-Co-NPs, or N1-34a-NPs normalized to that of cells treated with IgG-Co-NPs. Error bars indicate standard error. \* $p < 0.05$  Modified from Valcourt DM, Day ES, Manuscript in revision.

Finally, we investigated the effect of N1-34a-NPs on cell migration after 48 hours through a transwell invasion assay. This study showed that N1-34a-NPs could reduce TNBC cell migration by 34% relative to controls (**Figure 5.7a and 5.7b**).

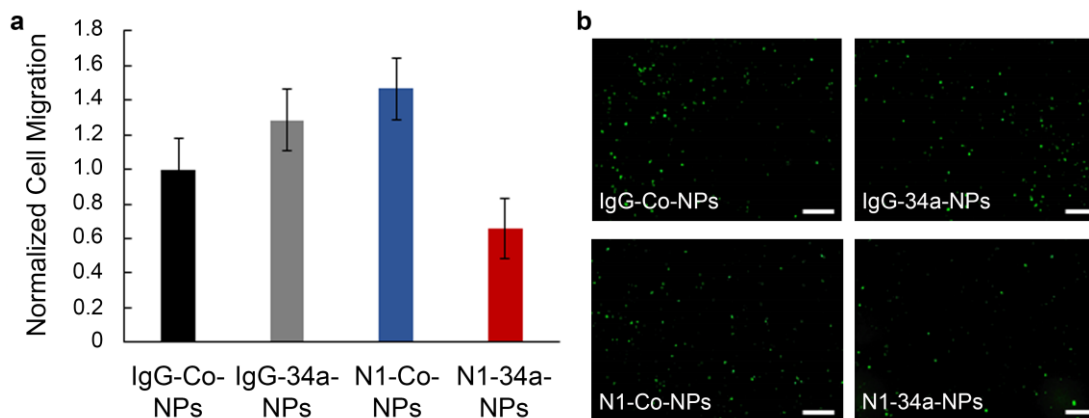


Figure 5.7: Effect of N1-34a-NPs on TNBC cell migration. (a) Normalized number of GFP-expressing MDA-MB-231 cells migrated through transwell insert after treatment with IgG-Co-NPs, IgG-34a-NPs, N1-Co-NPs, or N1-34a-NPs. Error bars indicate standard error. (b) Representative fluorescence images of GFP-expressing MDA-MB-231 cells migrated through transwell insert after treatment with IgG-Co-NPs, IgG-34a-NPs, N1-Co-NPs, or N1-34a-NPs. Scale bars = 500  $\mu$ m. Modified from Valcourt DM, Day ES, Manuscript in revision.

Altogether, these data indicate that N1-34a-NPs can functionally impair TNBC cells by activating senescence and inhibiting cell proliferation and migration.

### 5.3.4 Discussion

In this chapter, we used PLGA nanoparticles as carriers of both miR-34a mimics and Notch-1 antibodies to effectively treat TNBC by a combination of miRNA replacement therapy and antibody-mediated signal cascade interference. We showed by qRT-PCR and Western blotting that these N1-34a-NPs could inhibit the expression of several targets of miR-34a and Notch signaling, including Bcl-2, survivin, CCND1, Notch-1, and MDR1 *in vitro*. This gene regulation induced senescence and reduced cell proliferation and migration, which is in agreement with the known roles of miR-34a and Notch signaling in cancer cell biology. [84, 261–265] With further

optimization and *in vivo* evaluation, these N1-34a-NPs may offer a promising new strategy to treat TNBC.

Future studies that continue this work should investigate the optimal loading of miRNA and antibody components within the NP formulation. As synthesized here, N1-34a-NPs have a diameter of approximately 170 nm and an antibody loading of 4.6  $\mu\text{g}$  per mg PLGA. These NPs show a mild advantage in binding MDA-MB-231 cells compared to non-specific IgG functionalized NPs at early time points (Figure S1). However, this preferential binding is not maintained over the course of 24 hours, which may be due to interactions between the NPs and proteins in cell culture media. Notably, in previous work presented in Chapter 4, we have created Notch-1 antibody functionalized NPs that are approximately 70 nm in diameter and contain 9.1  $\mu\text{g}$  antibodies per mg PLGA; these NPs exhibit sustained preferential and specific binding of TNBC cells, which translates to enhanced tumor accumulation and retention compared to IgG functionalized NPs *in vivo* (Valcourt DM, Dang MN, Scully MA, and Day ES, manuscript in revision). We posit that the difference in particle size and antibody loading density between N1-34a-NPs and our previous NP formulation is responsible for the disparity in obtaining preferential and specific binding to MDA-MB-231 TNBC cells. This would be in agreement with prior studies that show cellular binding of NPs is significantly impacted by the size and shape of the NP [266–269] and by the density of the targeting moiety presented on the surface of the NP. [268, 269] Future studies are needed to define the optimal density of Notch-1 antibodies on these NPs to maximize TNBC cell-specific binding and potentially increase downstream Notch signaling inhibition.

While N1-34a-NPs did not display enhanced binding to TNBC cells in this work relative to IgG functionalized NPs, we did find that Notch-1 antibody functionalization was critical for eliciting significant therapeutic effect. The Notch signaling targets Hes5 and Hes1 were suppressed only with Notch-1 antibody-coated NPs, which confirms that the amount of NP binding was sufficient to elicit signal cascade interference. Likewise, even though N1-34a-NPs and IgG-34a-NPs had similar levels of interaction with TNBC cells, only the Notch-1 functionalized NPs had a notable effect on downstream miR-34a targets, indicating the inclusion of Notch-1 antibodies improves the efficacy of this formulation. It is known that coating NPs with specific targeting moieties like Notch-1 antibodies can alter the mechanism of endocytosis and subsequently influence the intracellular fate of the NP and any cargo it is carrying. [4, 270, 271] This altered trafficking can affect the potency of the cargo, which is particularly important for the delivery of RNA molecules like miR-34a that require cytosolic delivery to engage the RNA interference machinery and elicit gene regulation. [183] NPs typically enter cells through clathrin- or caveolae-dependent uptake mechanisms that lead to lysosomal accumulation, although in some cases caveolae have been shown to fuse with caveosomes to avoid lysosomal trafficking. [272–274] Future studies should elucidate the intracellular fate of N1-34a-NPs in order to provide insight to their mechanism of action and therapeutic potential.

Finally, future studies should also evaluate N1-34a-NPs in the *in vivo* setting. Notch signaling is primarily implicated in early stages of tumor development and in cancer stem cells. [250, 251] Additionally, Sethi and Kang have demonstrated that Notch signaling facilitates bone metastasis in later stages of tumor progression. [251] However, its role in the primary tumor at these later stages has not been extensively

explored. Reduced miR-34a expression has been associated with approximately 50% of TNBC cases and is correlated with poor prognosis. [275, 276] Future studies should examine the expression of the Notch-1 receptor in tumors of various sizes and miR-34a expression in tumors of various origins and determine the therapeutic efficacy of N1-34a-NPs when these expression levels are different than those explored in this work.

#### **5.4 Conclusions**

Overall, this work demonstrates that miR-34a-loaded, Notch-1 antibody functionalized PLGA NPs can effectively regulate Notch signaling and downstream miR-34a targets in TNBC cells *in vitro* to induce senescence and reduce cell proliferation and migration. These N1-34a-NPs are a promising alternative treatment for aggressive cancers like TNBC that display lower levels of miR-34a and are driven by overexpression of Notch signaling. With additional optimization, development, and implementation, these NPs may substantially improve patient outcomes.

## Chapter 6

### CONCLUSIONS AND FUTURE WORK

Some of the text in this chapter has been adapted from my following publications:

- (1) Valcourt, *et al. JBMRA*. 2019; 107(8): 1702-1712. [192]
- (2) Valcourt, *et al. ACS Nano*. 2020; 14(3): 3378-3388. [230]
- (3) Valcourt, *et al. Advanced Healthcare Materials*. 2020. *Accepted*.

#### 6.1 Introduction

This thesis has developed and evaluated novel nanoparticle formulations that can treat TNBC through three distinct mechanisms: photothermal therapy (Chapter 3), targeted drug delivery (Chapter 4), and targeted miRNA delivery (Chapter 5). This chapter will discuss the significance of this work to the field of cancer nanomedicine and propose future directions for the development of each of these nanoparticles. With continued optimization and implementation, these new therapeutic strategies may someday improve the prognosis for patients with TNBC.

#### 6.2 IR820-NPs as Potent Mediators of Photothermal Therapy

In Chapter 3, IR820-loaded PLGA nanoparticles were investigated as a biodegradable platform that enables pro-apoptotic PTT of TNBC *in vitro* and *in vivo*. **(Figure 6.1)**

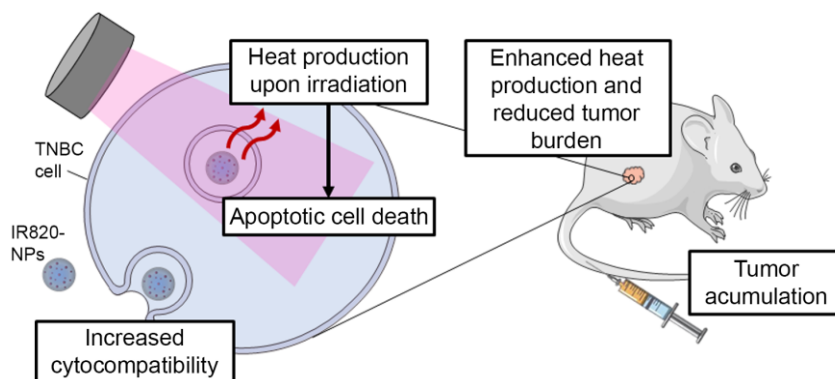


Figure 6.1: Scheme depicting the therapeutic potential of IR820-NPs as potent mediators of photothermal therapy both *in vitro* and *in vivo*.

These stable, monodisperse PLGA nanoparticles were efficiently loaded with IR820 dye, which maintained its optical properties upon encapsulation. [192] Further, IR820-NPs were found to interact with MDA-MB-231 TNBC cells in a dose- and time-dependent manner. [192] Encapsulation of the dye also increased its cytocompatibility, which allowed for a higher dose to be administered safely to cells prior to irradiation. [192] Upon irradiation with NIR light, this formulation provided potent mediation of PTT *in vitro*. After evaluation of the mechanism of cell death, IR820-NPs were found to primarily induce apoptosis, which is considered the preferred mechanism of cell death for inducing a beneficial immune response [106, 205].

Chapter 3 further investigated the potential of IR820-NPs in a subcutaneous murine TNBC xenograft model. After intravenous injection, IR820-NPs effectively accumulate in tumors within 24 hours. [192] When irradiated at this time point, tumors of mice treated with free IR820 dye experienced mild heating, while tumors that received IR820-NPs exhibited sustained heating above the threshold considered

necessary for irreversible cell damage using these irradiation conditions [222]. When this treatment was administered once per week over a period of 28 days, IR820-NP mediated PTT significantly reduced the tumor burden in these mice [192], demonstrating their potential as an alternative treatment strategy for TNBC while overcoming the limitations of other established PTT mediators that have unknown long-term health effects. Overall, this work advanced the field of photothermal therapy by demonstrating that polymer nanoparticles loaded with NIR-sensitive dyes can successfully mediate pro-apoptotic PTT, providing a biodegradable alternative to conventional gold-based photothermal conversion agents that will remain in the body indefinitely.

### **6.3 N1-ABT-NPs as an Effective Strategy for Targeted Drug Delivery**

Chapter 4 evaluated the ability of ABT-737-loaded, Notch-1 antibody functionalized nanoparticles to regulate Bcl-2 and Notch signaling as an alternative treatment strategy for TNBC *in vitro* and *in vivo*. (**Figure 6.2**) This approach is advantageous over conventional approaches because it provides targeted drug delivery to a disease that is currently unsusceptible to available targeted therapeutic strategies.

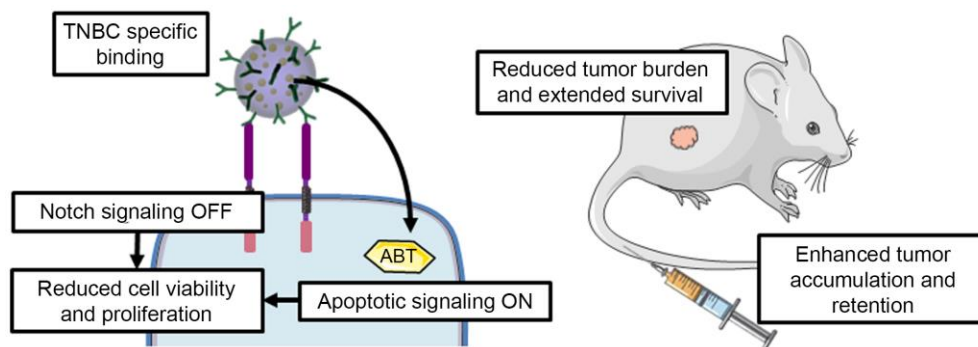


Figure 6.2: Scheme depicting the therapeutic potential of N1-ABT-NPs as targeted drug delivery vehicles both *in vitro* and *in vivo*. Modified from Valcourt DM, Dang MN, Scully MA, Day ES, Manuscript in revision.

N1-ABT-NPs were successfully synthesized to enable preferential and specific binding to MDA-MB-231 TNBC cells compared to MCF-10A healthy mammary epithelial cells. Upon evaluation of their therapeutic potential *in vitro*, N1-ABT-NPs reduced cell viability of MDA-MB-231 cells to a greater extent than the free components or non-specific IgG-ABT-NPs. In addition, N1-ABT-NPs significantly inhibited cellular function, as indicated by reduced cellular proliferation. The impact of N1-ABT-NPs on MDA-MB-231 TNBC cells was further investigated at the mRNA and protein level. This nanoparticle formulation regulated both Bcl-2 and Notch-1 signaling pathway targets at each level, indicating successful release of ABT-737 to influence Bcl-2 expression and multivalent binding of the Notch-1 receptor to enable signal cascade interference.

Following *in vitro* validation of therapeutic potential, N1-ABT-NPs were evaluated *in vivo*. In a subcutaneous murine TNBC xenograft model, DiD-loaded nanoparticles were used to examine the biodistribution of the antibody-nanoparticle conjugates. The results in Chapter 4 demonstrate that Notch-1 functionalization

increases both tumor accumulation and retention of nanoparticles compared to functionalization with non-specific IgG antibodies. N1-ABT-NPs were then evaluated for their ability to reduce tumor burden. In a dose optimization study that administered nanoparticles once per week, N1-ABT-NPs reduced tumor volume by 44% after three weeks of treatment. Further, in an extended therapeutic study, N1-ABT-NPs notably increased mouse survival time compared to IgG-ABT-NPs and a saline control. These dual antibody/drug nanocarriers are thus a promising therapeutic modality for aggressive cancers like TNBC that are driven by overactive Bcl-2 and Notch signaling. Given that TNBC is notorious for its lack of targeted therapies, the targeted antibody/drug carriers developed in this Chapter represent an exciting advance.

#### **6.4 N1-34a-NPs for Gene Regulation**

In Chapter 5, miR-34a-loaded, Notch-1 antibody functionalized PLGA nanoparticles were developed to treat TNBC *in vitro* through targeted miRNA delivery and antibody-mediated signal cascade interference. (**Figure 6.3**) This approach builds upon that described in Chapter 4, but confers on the formulation the ability to suppress a multitude of genes that drive tumor progression through the inclusion of miR-34a, whereas ABT-737 suppresses only Bcl-2, Bcl-X<sub>L</sub>, and Bcl-w. Accordingly, these miR-34a/Notch-1 antibody nanocarriers have the potential to dramatically impede tumor progression.

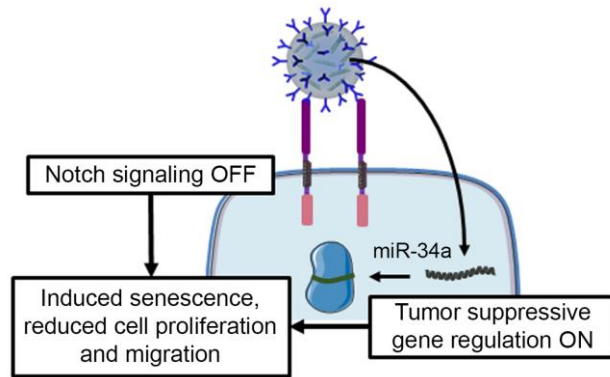


Figure 6.3: Scheme depicting the therapeutic potential of N1-34a-NPs for gene regulation *in vitro*.

The studies presented in Chapter 5 showed that PLGA nanoparticles were successfully loaded with miR-34a and functionalized with Notch-1 antibodies, enabling time-dependent interaction with MDA-MB-231 TNBC cells. Upon cellular binding and uptake, N1-34a-NPs effectively regulated miR-34a and Notch signaling pathway targets at the mRNA and protein level. This regulation further impaired cellular function, as this formulation was found to significantly reduce cell proliferation and migration and to induce senescence *in vitro*. With additional optimization, development, and implementation, these nanoparticles have the potential to be a potent treatment for aggressive cancers like TNBC that display lower levels of miR-34a and are driven by overexpression of Notch signaling. Some of the studies that may be performed to build on the results presented in this chapter are described in the following section.

## 6.5 Future Directions

This thesis introduces three novel alternative treatment strategies for TNBC that incorporate nanoparticles to mediate PTT, drug delivery, or gene regulation.

While these methods show promise at both the *in vitro* and *in vivo* level, further studies are needed to realize the full potential of these nanotherapeutics.

### **6.5.1 Formulation Optimization**

Each of the nanoparticles developed in this thesis have shown utility in treating TNBC, but they have not yet been optimized to elicit the maximum therapeutic effect, which would be desirable for clinical translation. A critical step in the future development of these particles is therefore revising the synthetic strategy to yield the greatest efficacy while using translational production methods. Chapter 3 details the development of IR820 dye-loaded PLGA nanoparticles for mediation of PTT. Future work with these IR820-NPs should examine nanoparticles whose surface has been modified with poly(ethylene glycol) or with antibodies, as this may extend circulation time and increase tumor delivery, thereby enhancing the overall therapeutic effect.

The results presented in Chapter 4 demonstrate successful synthesis of ABT-737-loaded, Notch-1 antibody functionalized PLGA nanoparticles. While the initial encapsulation efficiency of ABT-737 in unfunctionalized nanoparticles is high (over 95%), there is significant loss of the drug during antibody conjugation. This may be due to drug that is adsorbed onto the surface of the particles rather than physically encapsulated within them. In the future, this loss should be minimized to maximize drug loading and thereby efficacy of the nanoparticles. Additionally, the density of antibodies on the surface of the nanoparticles should be adjusted to yield the loading that provides the greatest specificity and preferential uptake in TNBC cells as well as the greatest inhibition of Notch signaling targets. Finally, for better translation of these nanoparticles into preclinical and clinical tests, the synthesis procedure should be altered to facilitate nanoparticle lyophilization and sterilization in powder form prior

to administration. Overall, by increasing drug and antibody loading within the nanoparticles, it is expected that tumor inhibition will be enhanced.

Chapter 5 demonstrates that N1-34a-NPs provide effective miRNA delivery to TNBC *in vitro*. While these nanoparticles effectively regulate Notch signaling and miR-34a targets as synthesized, the loading of each therapeutic modality should be optimized in future work. First, by increasing the quantity of miRNA in each nanoparticle, this treatment strategy may achieve similar therapeutic effects with fewer nanoparticles administered. This alteration would mitigate the risk of experiencing adverse effects from the PLGA content and may improve the formulation's performance *in vivo* with reduced release of TNF- $\alpha$ . [277] Further, by determining the optimal density of the antibodies on the surface of the particles, these N1-34a-NPs may exhibit the same preferential and specific TNBC cellular uptake that was demonstrated by the Notch-1 functionalized nanoparticles presented in Chapter 4, potentially increasing downstream Notch signaling inhibition. After further *in vitro* optimization, N1-34a-NPs should be evaluated *in vivo* to validate their efficacy and examine their impact on Notch-1 signaling and miR-34a target gene expression in various tumor sizes and types.

### **6.5.2 Tumor Models**

Mice have long been the model of choice in preclinical drug development due to their similarities with humans at the genetic level and their ease of handling, which simplifies study execution. However, cancer is a complex, multifactorial disease and one mouse model cannot recapitulate the entirety of human cancer progression from primary tumor development to metastasis. Moreover, a single mouse model cannot capture the genetic, epigenetic, immunological, histopathological, and structural

heterogeneity of cancer. [25–27] Therefore, nanomedicines should be evaluated in multiple murine models before moving to higher order species.

Chapters 3 and 4 employed a simple subcutaneous tumor model to evaluate the biodistribution and therapeutic efficacy of the respective nanoparticles. In this model, MDA-MB-231 TNBC cells are inoculated in the flank of immune deficient mice. It is important to note that the location of the tumor (subcutaneous versus orthotopic) may have impacted the distribution of the nanoparticles, and therefore future studies should examine treatment in orthotopic tumor models. The results presented in Chapter 4, in particular, demonstrate that N1-ABT-NPs have increased accumulation and retention in subcutaneous tumors compared to non-targeted IgG-ABT-NPs. In the future, the accumulation of these nanoparticles in both tumors and other major organs should be examined in greater detail. In Chapter 4, live animal imaging revealed fluorescence in an area that was larger than the tumor region of interest (ROI), likely due to nanoparticles located in the liver. While there is still a distinct signal in the ROI that preliminarily indicates there is enhanced tumor accumulation and retention with Notch-1 functionalized particles versus IgG functionalized particles, this should be corroborated in future studies by examining tissues *ex vivo* to remove interference from other organs.

Chapter 4 further demonstrates that N1-ABT-NPs are effective at reducing tumor burden using a subcutaneous tumor model in immune deficient mice. However, this work does not investigate the impact of these nanoparticles on the immune system. Between 1969 and 2005, 10-20% of all drugs that were withdrawn from use in the clinic were removed because of immunotoxicity. [278] Thus, it is critical to carefully evaluate nanoparticle-immune system interactions to improve upon the

current clinical translation rates seen with cancer nanomedicines. [279] To that end, a 4T1 or other murine-derived TNBC tumor model that can be established in immune competent animals should be utilized in future studies to evaluate this formulation's biocompatibility and overall efficacy.

Similarly, the tumor model used in Chapter 3 requires immune deficiency and thus cannot fully recapitulate how IR820-NP mediated PTT will affect tumor regression and the long-term health of the mice. While *ex vivo* analysis of the current tumor model can provide a preliminary indication of the mechanism of cell death induced by this treatment, a murine 4T1 tumor model may provide a more complete representation of the mechanism of cell death and how this impacts the immune system and overall efficacy of the therapy.

### **6.5.3 Evaluation of Notch-1 Expression**

While there is evidence that Notch-1 is widely overexpressed across human TNBC and correlates with poor prognosis [56, 249], it is classically considered to play the largest role in early stages of tumor development and in cancer stem cells [250, 251]. Sethi and Kang have expanded upon this role and demonstrated that Notch signaling facilitates bone metastasis in later stages of tumor progression [251], but its role in the primary tumor at these later stages has not been extensively explored. In Chapter 4, we evaluated the impact of N1-ABT-NPs on tumors in a relatively early stage, about 5 mm in diameter. While it is clear from both the *in vitro* and *in vivo* studies presented in Chapter 4 that N1-ABT-NPs have an enhanced effect on MDA-MB-231 TNBC cells that have constitutively overexpressed Notch-1 receptors, this level of expression may change depending upon not only the stage of the tumor (early versus late), but also the source of the tumor (murine versus human). Future work may

begin to evaluate this by delivering these nanoparticles to mice bearing tumors of different initial sizes and evaluating their efficacy in tumors that express varying levels of the Notch-1 receptor.

#### **6.5.4 Dosing/Treatment Regimen Optimization and Further *In Vivo* Analysis**

The *in vivo* evaluations performed in Chapters 3 and 4 demonstrate that IR820-NP mediated PTT and the targeted drug delivery conferred by N1-ABT-NPs are effective alternative strategies for treatment of TNBC. However, the dosing and treatment regimens used in these studies should be optimized for maximum therapeutic effect. The dose utilized in Chapter 3 was chosen based on literature for a preliminary evaluation of efficacy but delivering a higher concentration of IR820 may enable a greater therapeutic effect or even achieve reduced tumor burden with a single treatment. This optimization should also include dosing schedule changes to determine the dose and frequency of treatment that yields the maximum, pro-apoptotic therapeutic effect.

Induction of apoptotic or necrotic cell death is highly dependent upon the dose of the photothermal agent administered and subsequent irradiation parameters. [106] The results presented in Chapter 3 showed that heat production mediated by IR820-NPs is both concentration and laser intensity dependent, which agrees with previous studies. [210–212, 280] Thus, future studies that optimize *in vivo* dosing and irradiation regimens to maximize therapeutic efficacy should consider the effect these parameters have on the mechanism of cell death. It is important that further optimization of these parameters be performed *in vivo*, as *in vitro* evaluations may be influenced by the induction of secondary necrosis [106] and are likely to lack relevance in clinical translation [278, 281]. Future *in vivo* studies should also examine

nanoparticle tumor accumulation at more frequent time points to elucidate the optimal irradiation time following intravenous injection of the nanoparticles.

In addition to optimizing the dosing regimen of N1-ABT-NPs, future studies should directly compare these particles to freely delivered components *in vivo*. The work presented in Chapter 4 did not administer free ABT-737 due to its poor bioavailability and subsequent lack of efficacy. [131, 242, 282] However, this comparison should be made in future work to confirm that encapsulation of the drug in this delivery system is advantageous. It should be noted that, due to ABT-737's lack of solubility, it would need to be delivered orally or intraperitoneally, whereas Notch-1 antibodies would need to be delivered intravenously. As the nanoparticles deliver both agents intravenously, the biodistribution of each agent is likely to be different for free delivery versus nanoparticle delivery. Nevertheless, it will be important to compare the efficacy of N1-ABT-NPs versus the free agents to confirm the advantages of the nanocarrier system.

Future work investigating N1-ABT-NPs should also evaluate the therapeutic contribution of each modality and the impact of Notch-1 receptor expression on nanoparticle efficacy. The results in Chapter 4 demonstrate that N1-ABT-NPs effectively regulate Bcl-2 and Notch signaling *in vitro* through Western blotting and qPCR, but the impact of the antibodies alone on cell viability and the *in vivo* mechanism of action was not evaluated. To establish the therapeutic contribution of each component of the nanoparticles, unloaded Notch-1 functionalized nanoparticles should be investigated. These nanoparticles would provide insight into the extent of signal cascade interference afforded by the multivalent binding and how that translates into attenuated cellular function. Evaluating the various contributions of the

therapeutic components is also important considering the heterogenous nature of cancer.

### **6.5.5 Improving Nanoparticle Penetration with Photothermal Therapy**

Traditionally, nanoparticle accumulation in tumors is attributed to leaky vasculature and poor lymphatic drainage [103, 198, 283], a passive process known as the enhanced permeability and retention effect [284]. While the contribution of such passive mechanisms to overall nanoparticle accumulation in tumors is debated [285], researchers have used the concept of leaky vasculature and disrupting physical barriers within the tumor microenvironment to improve penetration of therapies. One promising method through which this is accomplished is PTT. By improving tumor vessel leakiness and denaturing collagen to enhance extracellular matrix permeability, local heating from PTT can increase the penetration of nanoparticles or subsequently delivered therapies. [286, 287] Additionally, PTT can induce expression of stress-related proteins that allow for targeting of therapies that follow. [288] Thus, future work with IR820-NP mediated PTT should evaluate the effect of the therapy on the tumor microenvironment and vascular permeability.

### **6.5.6 Versatility of a Platform Enabling Bcl-2 Inhibition**

In addition to demonstrating the value of N1-ABT-NPs in targeting and regulating the Notch signaling pathway in TNBC, the results in Chapter 4 also show that this platform can effectively regulate Bcl-2 through the delivery of ABT-737. Bcl-2 is a promising therapeutic target for many cancers [61, 252], thus extending the potential applicability of this nanoparticle formulation. The platform we have developed can be easily adapted to target other cancer types by exchanging the

targeting antibody on the surface of the nanoparticles. It is important to consider, however, that not all antibodies are antagonistic. Thus, targeting alternate receptors by exchanging the antibody will not automatically confer the same increase in therapeutic efficacy as was shown here.

While ABT-737 is potent and shows promise in the work presented in Chapter 4, it also inhibits Bcl-X<sub>L</sub> and Bcl-w in addition to Bcl-2. [289] However, there is evidence suggesting that the inhibition of Bcl-X<sub>L</sub> is responsible for the thrombocytopenia associated with clinical use of ABT-737 and its derivative ABT-263. [290] The results in Chapter 4 preliminarily indicate that encapsulating ABT-737 in these targeted nanoparticles eliminates this off-target effect, but the versatility of this platform would also allow for replacing ABT-737 with its re-engineered form, ABT-199, while maintaining its efficacy against cancers driven by dysregulation of Bcl-2. [289, 290] Thus, future work should evaluate ABT-199-loaded PLGA nanoparticles both with Notch-1 antibodies and other potential targeting agents.

### **6.5.7 Conclusions**

In summary, this thesis presents three new nanoparticle platforms that enable potent treatment of TNBC by diverse mechanisms: IR820-NPs for PTT, N1-ABT-NPs for targeted drug delivery, and N1-34a-NPs for gene regulation. More work is needed to optimize the synthesis of these systems and determine the treatment conditions that will maximize their efficacy. Future studies will need to be performed in advanced tumor models that account for the complexity of human tumors and their interaction with the immune system. However, the results presented in this thesis suggest that, with additional development and implementation, these nanoparticles have potential to dramatically improve patient outcomes.

## REFERENCES

- [1] Cancer Statistics <https://www.cancer.gov/about-cancer/understanding/statistics>.
- [2] Cancer Mortality Milestone: 25 years of Continuous Decline  
<http://pressroom.cancer.org/Statistics2019>.
- [3] Siegel, R. L.; Miller, K. D.; Jemal, A. Cancer Statistics, 2019. *CA. Cancer J. Clin.* **2019**, *69* (1), 7–34.
- [4] Valcourt, D. M.; Dang, M. N.; Wang, J.; Day, E. S. Nanoparticles for Manipulation of the Developmental Wnt, Hedgehog, and Notch Signaling Pathways in Cancer. *Ann. Biomed. Eng.* **2019**, 1–21.
- [5] Kapadia, C. H.; Luo, B.; Dang, M. N.; Irvin-Choy, N.; Valcourt, D. M.; Day, E. S. Polymer Nanocarriers for MicroRNA Delivery. *J. Appl. Polym. Sci.* **2019**.
- [6] Valcourt, D. M.; Harris, J.; Riley, R. S.; Dang, M.; Wang, J.; Day, E. S. Advances in Targeted Nanotherapeutics: From Bioconjugation to Biomimicry. *Nano Res.* **2018**, *11* (10), 4999–5016.
- [7] Onitilo, A. A.; Engel, J. M.; Greenlee, R. T.; Mukesh, B. N. Breast Cancer Subtypes Based on ER/PR and Her2 Expression: Comparison of Clinicopathologic Features and Survival. *Clin. Med. Res.* **2009**, *7* (1/2), 4–13.
- [8] Bianchini, G.; Balko, J. M.; Mayer, I. A.; Sanders, M. E.; Gianni, L. Triple-Negative Breast Cancer: Challenges and Opportunities of a Heterogeneous Disease. *Nature* **2016**, *13*, 674–690.
- [9] Griffiths, C. L.; Olin, J. L. Triple Negative Breast Cancer: A Brief Review of Its Characteristics and Treatment Options. *J. Pharm. Pract.* **2012**, *25* (3), 319–323.
- [10] Kassam, F.; Enright, K.; Dent, R.; Dranitsaris, G.; Myers, J.; Flynn, C.; Fralick, M.; Kumar, R.; Clemons, M. Survival Outcomes for Patients with Metastatic Triple-Negative Breast Cancer: Implications for Clinical Practice and Trial Design. *Clin. Breast Cancer* **2009**, *9* (1), 29–33.
- [11] Liedtke, C.; Mazouni, C.; Hess, K. R.; André, F.; Tordai, A.; Mejia, J. A.;

- Symmans, W. F.; Gonzalez-Angulo, A. M.; Hennessy, B.; Green, M.; et al. Response to Neoadjuvant Therapy and Long-Term Survival in Patients with Triple-Negative Breast Cancer. *J. Clin. Oncol.* **2008**, *26* (8), 1275–1281.
- [12] Tseng, L.; Hsu, N.; Chen, S.; Lu, Y.; Lin, C.; Chang, D.; Li, H.; Lin, Y.; Chang, H.; Chao, T.; et al. Distant Metastasis in Triple-Negative Breast Cancer. *Neoplasma* **2013**, *60* (3), 290–294.
- [13] Lakhtakia, R. A Brief History of Breast Cancer - Part 1: Surgical Domination Reinvented. *Sultan Qaboos Univ. Med. J.* **2014**, *14* (2), 166–169.
- [14] History of Breast Cancer <https://www.healthline.com/health/history-of-breast-cancer>.
- [15] Christakis, P. The Birth of Chemotherapy at Yale. *Yale J. Biol. Med.* **2011**, *84*, 169–172.
- [16] Tringale, K.; Pang, J.; Nguyen, Q. Image-Guided Surgery in Cancer: A Strategy to Reduce Incidence of Positive Surgical Margins. *Wiley Interdiscip. Rev. Syst. Biol. Med.* **2018**, *10* (3), e1412.
- [17] Rashid, O. M.; Takabe, K. Does Removal of the Primary Tumor in Metastatic Breast Cancer Improve Survival? *J. Women's Heal.* **2014**, *23* (2), 184–188.
- [18] Cady, B.; Nathan, N.; Michaelson, J.; Golshan, M.; Smith, B. Matched Pair Analyses of Stage IV Breast Cancer with or without Resection of Primary Breast Site. *Ann. Surg. Oncol.* **2008**, *15* (12), 3384–3395.
- [19] Blyth, B.; Cole, A.; MacManus, M.; Martin, O. Radiation Therapy-Induced Metastasis: Radiobiology and Clinical Implications. *Clin. Exp. Metastasis* **2018**, *35* (4), 223–236.
- [20] Lameire, N. Nephrotoxicity of Recent Anti-Cancer Agents. *Clin. Kidney J.* **2014**, *7* (1), 11–22.
- [21] Suter, T.; Ewer, M. Cancer Drugs and the Heart: Importance and Management. *Eur. Heart J.* **2013**, *34* (15), 1102–1111.
- [22] Jensen, E.; DeSomber, E.; Jungblut, P. Estrogen Receptors in Hormone Responsive Tissues and Tumors. In *International Symposium on Endogenous Factors Influencing Host-Tumor Balance*; Wissler, R., Dao, T., Wood, S. J., Eds.; University of Chicago Press: Chicago and London, 1967.
- [23] Scott, A. M.; Allison, J. P.; Wolchok, J. D. Monoclonal Antibodies in Cancer

- Therapy. *Cancer Immun.* **2012**, *12* (14), 1–8.
- [24] Targeted Therapy for Breast Cancer <https://www.cancer.org/cancer/breast-cancer/treatment/targeted-therapy-for-breast-cancer.html>.
- [25] Sarkar, S.; Horn, G.; Moulton, K.; Oza, A.; Byler, S.; Kokolus, S.; Longacre, M. Cancer Development, Progression, and Therapy: An Epigenetic Overview. *Int J Mol Sci* **2013**, *14* (10), 21087–21113.
- [26] Hanahan, D.; Weinberg, R. A. Hallmarks of Cancer: The Next Generation. *Cell* **2011**, *144*, 646–674.
- [27] Kim, R.; Emi, M.; Tanabe, K. Cancer Immunoediting from Immune Surveillance to Immune Escape. *Immunology* **2007**, *121* (1), 1–14.
- [28] Hanahan, D.; Weinberg, R. A. The Hallmarks of Cancer. *Cell* **2000**, *100*, 57–70.
- [29] Basson, M. A. Signaling in Cell Differentiation and Morphogenesis. *Cold Spring Harb. Perspect. Biol.* **2012**, *4*, a008151.
- [30] Kim, M.; Jho, E. Cross-Talk between Wnt/ $\beta$ -Catenin and Hippo Signaling Pathways: A Brief Review. *BMB Rep.* **2014**, *47* (10), 540–545.
- [31] Sancho, R.; Cremona, C. A.; Behrens, A. Stem Cell and Progenitor Fate in the Mammalian Intestine: Notch and Lateral Inhibition in Homeostasis and Disease. *EMBO Rep.* **2015**, *16* (5), 571–581.
- [32] Briscoe, J.; Therond, P. P. The Mechanisms of Hedgehog Signalling and Its Roles in Development and Disease. *Nature* **2013**, *14*, 416–429.
- [33] Ring, A.; Kim, Y.-M.; Kahn, M. Wnt/Catenin Signaling in Adult Stem Cell Physiology and Disease. *Stem Cell Rev. Reports* **2014**, *10* (4), 512–525.
- [34] Takebe, N.; Harris, P. J.; Warren, R. Q.; Ivy, S. P. Targeting Cancer Stem Cells by Inhibiting Wnt, Notch, and Hedgehog Pathways. *Nature* **2011**, *8*, 97–106.
- [35] Takebe, N.; Miele, L.; Harris, P. J.; Jeong, W.; Bando, H.; Kahn, M.; Yang, S. X.; Ivy, S. P. Targeting Notch, Hedgehog, and Wnt Pathways in Cancer Stem Cells: Clinical Update. *Nat. Rev. Clin. Oncol.* **2015**, *12* (8), 445–464.
- [36] Karamboulas, C.; Ailles, L. Developmental Signaling Pathways in Cancer Stem Cells of Solid Tumors. *Biochim. Biophys. Acta* **2013**, *1830*, 2481–2495.
- [37] Burke, A. R.; Singh, R. N.; Carroll, D. L.; Torti, F. M.; Torti, S. V. Targeting

Cancer Stem Cells with Nanoparticle-Enabled Therapies. *J. Mol. Biomarkers Diagnosis* **2013**, 1–8.

- [38] Hong, I.-S.; Jang, G.-B.; Lee, H.-Y.; Nam, J.-S. Targeting Cancer Stem Cells by Using the Nanoparticles. *Int. J. Nanomedicine* **2015**, *10*, 251–260.
- [39] McDermott, S. P.; Wicha, M. S. Targeting Breast Cancer Stem Cells. *Mol. Oncol.* **2010**, *4*, 404–419.
- [40] Pannuti, A.; Foreman, K.; Rizzo, P.; Osipo, C.; Golde, T.; Osborne, B.; Miele, L. Targeting Notch to Target Cancer Stem Cells. *Clin. Cancer Res.* **2010**, *16* (12), 3141–3153.
- [41] Wu, X.; Chen, H.; Wang, X. Can Lung Cancer Stem Cells Be Targeted for Therapies? *Cancer Treat. Rev.* **2012**, *38*, 580–588.
- [42] McGowan, P. M.; Simeone, C.; Ribot, E. J.; Foster, P. J.; Palmieri, D.; Steeg, P. S.; Allan, A. L.; Chambers, A. F. Notch1 Inhibition Alters the CD44<sup>hi</sup>/CD24<sup>lo</sup> Population and Reduces the Formation of Brain Metastases from Breast Cancer. *Mol. Cancer Res.* **2011**, *9* (7), 834–845.
- [43] Zhou, B.-B. S.; Zhang, H.; Damelin, M.; Geles, K. G.; Grindley, J. C.; Dirks, P. B. Tumour-Initiating Cells: Challenges and Opportunities for Anticancer Drug Discovery. *Nature* **2009**, *8*, 806–823.
- [44] Speiser, J. J.; Ersahin, C.; Osipo, C. The Functional Role of Notch Signaling in Triple-Negative Breast Cancer. In *Vitamins and Hormones*; 2013; Vol. 93, pp 277–306.
- [45] Pohl, S.-G.; Brook, N.; Agostino, M.; Arfuso, F.; Kumar, A. P.; Dharmarajan, A. Wnt Signaling in Triple-Negative Breast Cancer. *Oncogenesis* **2017**, *6*, e310.
- [46] Habib, J. G.; O’Shaughnessy, J. A. The Hedgehog Pathway in Triple-Negative Breast Cancer. *Cancer Med.* **2016**, *5* (10), 2989–3006.
- [47] Yuan, X.; Wu, H.; Xu, H.; Xiong, H.; Chu, Q.; Yu, S.; Wu, G. S.; Wu, K. Notch Signaling: An Emerging Therapeutic Target for Cancer Treatment. *Cancer Lett.* **2015**, *369*, 20–27.
- [48] Espinoza, I.; Miele, L. Notch Inhibitors for Cancer Treatment. *Pharmacol. Ther.* **2013**, *139*, 95–110.
- [49] Ichimura, N.; Yamamoto, N.; Nishikawa, M.; Furue, H.; Kondo, Y.; Hibi, H. Notch3 Is Frequently Downregulated in Oral Cancer. *J. Oral Maxillofac.*

*Surgery, Med. Pathol.* **2017**, *29*, 504–510.

- [50] Wen, X.-F.; Chen, M.; Wu, Y.; Chen, M.-N.; Glogowska, A.; Klonisch, T.; Zhang, G.-J. Inhibitor of DNA Binding 2 Inhibits Epithelial-Mesenchymal Transition via Up-Regulation of Notch3 in Breast Cancer. *Transl. Oncol.* **2018**, *11* (5), 1259–1270.
- [51] Huang, Y.; Lin, L.; Shanker, A.; Malhotra, A.; Yang, L.; Dikov, M. M.; Carbone, D. P. Resuscitating Cancer Immunosurveillance: Selective Stimulation of DLL1-Notch Signaling in T Cells Rescues T-Cell Function and Inhibits Tumor Growth. *Cancer Res.* **2011**, *71* (19), 6122–6132.
- [52] Aburjania, Z.; Jang, S.; Whitt, J.; Jaskula-Stzul, R.; Chen, H.; Rose, J. B. The Role of Notch3 in Cancer. *Oncologist* **2018**, *23*, 1–12.
- [53] Harrison, H.; Farnie, G.; Howell, S. J.; Rock, R. E.; Stylianou, S.; Brennan, K. R.; Bundred, N. J.; Clarke, R. B. Regulation of Breast Cancer Stem Cell Activity by Signaling through the Notch4 Receptor. *Cancer Res.* **2010**, *70* (2), 709–719.
- [54] Speiser, J.; Foreman, K.; Drinka, E.; Godellas, C.; Perez, C.; Salhadar, A.; Ersahin, C.; Rajan, P. Notch-1 and Notch-4 Biomarker Expression in Triple-Negative Breast Cancer. *Int. J. Surg. Pathol.* **2012**, *20* (2), 139–145.
- [55] Hayashi, T.; Gust, K. M.; Wyatt, A. W.; Goriki, A.; Jager, W.; Awrey, S.; Li, N.; Oo, H. Z.; Altamirano-Dimas, M.; Buttyan, R.; et al. Not All NOTCH Is Created Equal: The Oncogenic Role of NOTCH2 in Bladder Cancer and Its Implications for Targeted Therapy. *Clin. Cancer Res.* **2016**, *22* (12), 2981–2993.
- [56] Stylianou, S.; Clarke, R. B.; Brennan, K. Aberrant Activation of Notch Signaling in Human Breast Cancer. *Cancer Res.* **2006**, *66* (3), 1517–1526.
- [57] Ristorcelli, E.; Beraud, E.; Mathieu, S.; Lombardo, D.; Verine, A. Essential Role of Notch Signaling in Apoptosis of Human Pancreatic Tumoral Cells Mediated by Exosomal Nanoparticles. *Int. J. Cancer* **2009**, *125*, 1016–1026.
- [58] Speiser, J. J.; Ersahin, C.; Osipo, C. The Functional Role of Notch Signaling in Triple-Negative Breast Cancer. In *Vitamins and Hormones*; 2013; Vol. 93, pp 277–306.
- [59] Giuli, M. V.; Giuliani, E.; Screpanti, I.; Bellavia, D.; Checquolo, S. Notch Signaling Activation as a Hallmark for Triple-Negative Breast Cancer Subtype. *J. Oncol.* **2019**.

- [60] Haupt, S.; Berger, M.; Goldberg, Z.; Haupt, Y. Apoptosis - The p53 Network. *J. Cell Sci.* **2003**, *116* (20), 4077–4085.
- [61] Campbell, K. J.; Tait, S. W. G. Targeting BCL-2 Regulated Apoptosis in Cancer. *Open Biol.* **2018**, *8*, 1–11.
- [62] Jiang, X.; Wang, X. Cytochrome c Promotes Caspase-9 Activation by Inducing Nucleotide Binding to Apaf-1. *J. Biol. Chem.* **2000**, *275* (40), 31199–31203.
- [63] Zou, H.; Li, Y.; Liu, X.; Wang, X. An APAF-1·Cytochrome c Multimeric Complex Is a Functional Apoptosome That Activates Procaspase-9. *J. Biol. Chem.* **1999**, *274* (17), 11549–11556.
- [64] Zou, H.; Henzel, W. J.; Liu, X.; Lutschg, A.; Wang, X. Apaf-1, a Human Protein Homologous to *C. Elegans* CED-4, Participates in Cytochrome c-Dependent Activation of Caspase-3. *Cell* **1997**, *90* (3), 405–413.
- [65] Li, P.; Nijhawan, D.; Budihardjo, I.; Srinivasula, S. M.; Ahmad, M.; Alnemri, E. S.; Wang, X. Cytochrome c and dATP-Dependent Formation of Apaf-1/Caspase-9 Complex Initiates an Apoptotic Protease Cascade. *Cell* **1997**, *91* (4), 479–489.
- [66] Srinivasula, S. M.; Ahmad, M.; Fernandes-Alnemri, T.; Alnemri, E. S. Autoactivation of Procaspase-9 by Apaf-1-Mediated Oligomerization. *Mol. Cell* **1998**, *1* (7), 949–957.
- [67] Saleh, A.; Srinivasula, S. M.; Acharya, S.; Fishel, R.; Alnemri, E. S. Cytochrome c and dATP-Mediated Oligomerization of Apaf-1 Is a Prerequisite for Procaspase-9 Activation. *J. Biol. Chem.* **1999**, *274* (25), 17941–17945.
- [68] Shamas-Din, A.; Kale, J.; Leber, B.; Andrews, D. W. Mechanisms of Action of Bcl-2 Family Proteins. *Cold Spring Harb. Perspect. Biol.* **2013**, *5* (4), a008714.
- [69] Kale, J.; Osterlund, E. J.; Andrews, D. W. BCL-2 Family Proteins: Changing Partners in the Dance towards Death. *Cell Death Differ.* **2018**, *25*, 65–80.
- [70] van Delft, M. F.; Huang, D. C. S. How the Bcl-2 Family of Proteins Interact to Regulate Apoptosis. *Cell Res.* **2006**, *16*, 203–213.
- [71] Ozretic, P.; Alvir, I.; Sarcevic, B.; Vujaskovic, Z.; Rendic-Miocevic, Z.; Roguljic, A.; Beketic-Oreskovic, L. Apoptosis Regulator Bcl-2 Is an Independent Prognostic Marker for Worse Overall Survival in Triple-Negative Breast Cancer Patients. *Int. J. Biol. Markers* **2018**, *33* (1), 109–115.

- [72] Deng, X.; Cao, M.; Zhang, J.; Hu, K.; Yin, Z.; Zhou, Z.; Xiao, X.; Yang, Y.; Sheng, W.; Wu, Y.; et al. Hyaluronic Acid-Chitosan Nanoparticles for Co-Delivery of MiR-34a and Doxorubicin in Therapy against Triple Negative Breast Cancer. *Biomaterials* **2014**, *35*, 4333–4344.
- [73] Inao, T.; Iida, Y.; Moritani, T.; Okimoto, T.; Tanino, R.; Kotani, H.; Harada, M. Bcl-2 Inhibition Sensitizes Triple-Negative Human Breast Cancer Cells to Doxorubicin. *Oncotarget* **2018**, *9* (39), 25545–25556.
- [74] He, L.; Hannon, G. J. MicroRNAs: Small RNAs with a Big Role in Gene Regulation. *Nat. Rev. Genet.* **2004**, *5*, 522–531.
- [75] Rupaimoole, R.; Slack, F. MicroRNA Therapeutics: Towards a New Era for the Management of Cancer and Other Diseases. *Nat. Rev. Drug Discov.* **2017**, *16* (3), 203–222.
- [76] Jovanovic, M.; Hengartner, M. O. miRNAs and Apoptosis: RNAs to Die for. *Oncogene* **2006**, *25*, 6176–6187.
- [77] MacFarlane, L.-A.; Murphy, P. R. MicroRNA: Biogenesis, Function and Role in Cancer. *Curr. Genomics* **2010**, *11*, 537–561.
- [78] Kim, V. MicroRNA Biogenesis: Coordinated Cropping and Dicing. *Nat. Rev. Cell Biol.* **2005**, *6* (5), 376–385.
- [79] Nakielny, S.; Dreyfuss, G. Transport of Proteins and RNAs in and out of the Nucleus. *Cell* **1999**, *99*, 677–690.
- [80] Murchison, E.; Hannon, G. miRNAs on the Move: miRNA Biogenesis and the RNAi Machinery. *Curr. Opin. Cell Biol.* **2004**, *16* (3), 223–229.
- [81] Guo, L.; Lu, Z. The Fate of miRNA\* Strand through Evolutionary Analysis: Implication for Degradation as Merely Carrier Strand or Potential Regulatory Molecule? *PLoS One* **2010**, *5* (6), e11387.
- [82] Suzuki, H. I.; Yamagata, K.; Sugimoto, K.; Iwamoto, T.; Kato, S.; Miyazono, K. Modulation of microRNA Processing by p53. *Nature* **2009**, *460*, 529–533.
- [83] Hermeking, H. p53 Enters the MicroRNA World. *Cancer Cell* **2007**, *12*, 414–418.
- [84] Hermeking, H. The miR-34 Family in Cancer and Apoptosis. *Cell Death Differ.* **2010**, *17*, 193–199.
- [85] Misso, G.; Di Martino, M. T.; De Rosa, G.; Farooqi, A. A.; Lombardi, A.;

- Campani, V.; Zarone, M. R.; Gullà, A.; Tagliaferri, P.; Tassone, P.; et al. Mir-34: A New Weapon Against Cancer? *Mol. Ther. - Nucleic Acids* **2014**, *3*, e194.
- [86] Saito, Y.; Nakaoka, T.; Saito, H. microRNA-34a as a Therapeutic Agent against Human Cancer. *J. Clin. Med.* **2015**, *4*, 1951–1959.
- [87] Gallardo, E.; Navarro, A.; Vinolas, N.; Marrades, R.; Diaz, T.; Gel, B.; Quera, A.; Bandres, E.; Garcia-Foncillas, J.; Ramirez, J.; et al. miR-34a as a Prognostic Marker of Relapse in Surgically Resected Non-Small-Cell Lung Cancer. *Carcinogenesis* **2009**, *30* (11), 1903–1909.
- [88] Welch, C.; Chen, Y.; Stallings, R. L. MicroRNA-34a Functions as a Potential Tumor Suppressor by Inducing Apoptosis in Neuroblastoma Cells. *Oncogene* **2007**, *26*, 5017–5022.
- [89] Li, L.; Yuan, L.; Luo, J.; Gao, J.; Guo, J.; Xie, X. MiR-34a Inhibits Proliferation and Migration of Breast Cancer through down-Regulation of Bcl-2 and SIRT1. *Clin. Exp. Med.* **2013**, *13*, 109–117.
- [90] Adams, B. D.; Wali, V. B.; Cheng, C. J.; Inukai, S.; Booth, C. J.; Agarwal, S.; Rimm, D. L.; Györffy, B.; Santarpia, L.; Pusztai, L.; et al. miR-34a Silences c-SRC to Attenuate Tumor Growth in Triple-Negative Breast Cancer. *Cancer Res.* **2016**, *76* (4), 927–939.
- [91] Li, X.; Ji, M.; Zhong, S.; Zha, Q.; Xu, J.; Zhao, J.; Tang, J. MicroRNA-34a Modulates Chemosensitivity of Breast Cancer Cells to Adriamycin by Targeting Notch1. *Arch. Med. Res.* **2012**, *43* (7), 514–521.
- [92] Park, E. Y.; Chang, E.; Lee, E. J.; Lee, H.-W.; Kang, H.-G.; Chun, K.-H.; Woo, Y. M.; Kong, H. K.; Ko, J. Y.; Suzuki, H.; et al. Targeting of miR34a-NOTCH1 Axis Reduced Breast Cancer Stemness and Chemoresistance. *Cancer Res.* **2014**, *74* (24), 7573–7582.
- [93] Yang, S.; Li, Y.; Gao, J.; Zhang, T.; Li, S.; Luo, A.; Chen, H.; Ding, F.; Wang, X.; Liu, Z. MicroRNA-34 Suppresses Breast Cancer Invasion and Metastasis by Directly Targeting Fra-1. *Oncogene* **2013**, *32*, 4294–4303.
- [94] Kreuter, J. Nanoparticles - a Historical Perspective. *Int. J. Pharm.* **2007**, *331*, 1–10.
- [95] Sugibayashi, K.; Akimoto, M.; Morimoto, Y.; Nadai, T.; Kato, Y. Drug-Carrier Property of Albumin Microspheres in Chemotherapy. III. Effect of Microsphere-Entrapped 5-Fluorouracil on Ehrlich Ascites Carcinoma in Mice. *J. Pharmacobiodyn.* **1979**, *2* (6), 350–355.

- [96] Widder, K. J.; Marino, P. A.; Morris, R. M.; Howard, D. P.; Poore, G. A.; Senyei, A. E. Selective Targeting of Magnetic Albumin Microspheres to the Yoshida Sarcoma: Ultrastructural Evaluation of Microsphere Disposition. *Eur. J. Cancer Clin. Oncol.* **1983**, *19* (1), 141–147.
- [97] Widder, K. J.; Morris, R. M.; Poore, G. A.; Howard, D. P.; Senyei, A. E. Selective Targeting of Magnetic Albumin Microspheres Containing Low-Dose Doxorubicin: Total Remission in Yoshida Sarcoma-Bearing Rats. *Eur. J. Cancer* **1983**, *19* (1), 135–139.
- [98] Brasseur, F.; Couvreur, P.; Kante, B.; Deckers-Passau, L.; Roland, M.; Deckers, C.; Speisers, P. Actinomycin D Adsorbed on Polymethylcyanoacrylate Nanoparticles: Increased Efficiency against an Experimental Tumor. *Eur. J. Cancer* **1980**, *16* (11), 1441–1445.
- [99] Couvreur, P.; Kante, B.; Grislain, L.; Roland, M.; Speiser, P. Toxicity of Polyalkylcyanoacrylate Nanoparticles II: Doxorubicin-Loaded Nanoparticles. *J. Pharm. Sci.* **1982**, *71* (7), 790–792.
- [100] Couvreur, P.; Grislain, L.; Lenaerts, V.; Brasseur, F.; Guiot, P.; Biernacki, A. Biodegradable Polymeric Nanoparticles as Drug Carrier for Antitumor Agents. In *Polymeric Nanoparticles and Microspheres*; Guiot, P., Couvreur, P., Eds.; CRC Press: Boca Raton, 1986; pp 27–93.
- [101] Chiannikulchai, N.; Driouich, Z.; Benoit, J.; Parodi, A.; Couvreur, P. Doxorubicin-Loaded Nanoparticles: Increased Efficiency in Murine Hepatic Metastases. *Sel. Cancer Ther.* **1989**, *5* (1).
- [102] Grislain, L.; Couvreur, P.; Lenaerts, V.; Roland, M.; Deprez-Decampeneere, D.; Speiser, P. Pharmacokinetics and Distribution of a Biodegradable Drug-Carrier. *Int. J. Pharm.* **1983**, *15* (3), 335–345.
- [103] Matsumura, Y.; Maeda, H. A New Concept for Macromolecular Therapeutics in Cancer Chemotherapy: Mechanism of Tumoritropic Accumulation of Proteins and the Antitumor Agent Smancs. *Cancer Res.* **1986**, *46* (8), 6387–6392.
- [104] Dong, X.; Mumper, R. J. Nanomedicinal Strategies to Treat Multidrug-Resistant Tumors: Current Progress. *Nanomedicine* **2010**, *5* (4), 597–615.
- [105] Rwei, A. Y.; Wang, W.; Kohane, D. S. Photoresponsive Nanoparticles for Drug Delivery. *Nanotoday* **2015**, *10* (4), 451–467.
- [106] Melamed, J. R.; Edelstein, R. S.; Day, E. S. Elucidating the Fundamental

Mechanisms of Cell Death Triggered by Photothermal Therapy. *ACS Nano* **2015**, *9* (1), 6–11.

- [107] Fay, B. L.; Melamed, J. R.; Day, E. S. Nanoshell-Mediated Photothermal Therapy Can Enhance Chemotherapy in Inflammatory Breast Cancer Cells. *Int. J. Med.* **2015**, *10*, 6931–6941.
- [108] Riley, R. S.; Day, E. S. Gold Nanoparticle-Mediated Photothermal Therapy: Applications and Opportunities for Multimodal Cancer Treatment. *WIREs Nanomedicine and Nanobiotechnology* **2017**.
- [109] Rastinehad, A. R.; Anastos, H.; Wajswol, E.; Winoker, J. S.; Sfakianos, J. P.; Doppalapudi, S. K.; Carrick, M. R.; Knauer, C. J.; Taouli, B.; Lewis, S. C.; et al. Gold Nanoshell-Localized Photothermal Ablation of Prostate Tumors in a Clinical Pilot Device Study. *Proc. Natl. Acad. Sci.* **2019**, *116* (37), 18590–18596.
- [110] Stern, J. M.; Kibanov Solomonov, V. V.; Sazykina, E.; Schwartz, J. A.; Gad, S. C.; Goodrich, G. P. Initial Evaluation of the Safety of Nanoshell-Directed Photothermal Therapy in the Treatment of Prostate Disease. *Int. J. Toxicol.* **2016**, *35* (1), 38–46.
- [111] Weissleder, R. A Clearer Vision for in Vivo Imaging. *Nat. Biotechnol.* **2001**, *19* (April).
- [112] Bear, A. S.; Kennedy, L. C.; Young, J. K.; Perna, S. K.; Almeida, J. P. M.; Lin, A. Y.; Eckels, P. C.; Drezek, R. A.; Foster, A. E. Elimination of Metastatic Melanoma Using Gold Nanoshell-Enabled Photothermal Therapy and Adoptive T Cell Transfer. *PLoS One* **2013**, *8* (7).
- [113] Stone, J.; Jackson, S.; Wright, D. Biological Applications of Gold Nanorods. *Wiley Interdiscip. Rev. Nanomedicine Nanobiotechnology* **2011**, *3* (1), 100–109.
- [114] Skrabalak, S. E.; Chen, J.; Au, L.; Lu, X.; Li, X.; Xia, Y. Gold Nanocages for Biomedical Applications. *Adv. Mater.* **2007**, *19* (20), 3177–3184.
- [115] Dam, D.; Culver, K.; Kandela, I.; Lee, R.; Chandra, K.; Lee, H.; Mantis, C.; Ugolkov, A.; Mazar, A.; Odom, T. Biodistribution and in Vivo Toxicity of Aptamer-Loaded Gold Nanostars. *Nanomedicine* **2015**, *11* (3), 671–679.
- [116] Cole, J. R.; Mirin, N. A.; Knight, M. W.; Goodrich, G. P.; Halas, N. J. Photothermal Efficiencies of Nanoshells and Nanorods for Clinical Therapeutic Applications. *J. Phys. Chem. C* **2009**, *113* (28), 12090–12094.

- [117] Nanospectra Biosciences Inc. Efficacy Study of AuroLase Therapy in Subjects With Primary and/or Metastatic Lung Tumors  
<https://clinicaltrials.gov/ct2/show/NCT01679470?term=auroshell&rank=3>.
- [118] Nanospectra Biosciences Inc. Pilot Study of AuroLase(tm) Therapy in Refractory and/or Recurrent Tumors of the Head and Neck  
<https://clinicaltrials.gov/ct2/show/NCT00848042>.
- [119] Song, X.; Chen, Q.; Liu, Z. Recent Advances in the Development of Organic Photothermal Nano-Agents. *Nano Res.* **2015**, *8* (2), 340–354.
- [120] Yue, C.; Liu, P.; Zheng, M.; Zhao, P.; Wang, Y.; Ma, Y.; Cai, L. IR-780 Dye Loaded Tumor Targeting Theranostic Nanoparticles for NIR Imaging and Photothermal Therapy. *Biomaterials* **2013**, *34* (28), 6853–6861.
- [121] Chen, Y.; Li, Z.; Wang, H.; Wang, Y.; Han, H.; Jin, Q.; Ji, J. IR-780 Loaded Phospholipid Mimicking Homopolymeric Micelles for Near-IR Imaging and Photothermal Therapy of Pancreatic Cancer. *ACS Appl. Mater. Interfaces* **2016**, *8* (11), 6852–6858.
- [122] Wang, K.; Zhang, Y.; Wang, J.; Yuan, A.; Sun, M.; Wu, J.; Hu, Y. Self-Assembled IR780-Loaded Transferrin Nanoparticles as an Imaging, Targeting and PDT/PTT Agent for Cancer Therapy. *Sci. Rep.* **2016**, *6* (June), 1–11.
- [123] Kuang, Y.; Zhang, K.; Cao, Y.; Chen, X.; Wang, K.; Liu, M.; Pei, R. Hydrophobic IR-780 Dye Encapsulated in cRGD-Conjugated Solid Lipid Nanoparticles for NIR Imaging-Guided Photothermal Therapy. *ACS Appl. Mater. Interfaces* **2017**, *9* (14), 12217–12226.
- [124] Yuan, A.; Qiu, X.; Tang, X.; Liu, W.; Wu, J.; Hu, Y. Self-Assembled PEG-IR-780-C13 Micelle as a Targeting, Safe and Highly-Effective Photothermal Agent for In vivo Imaging and Cancer Therapy. *Biomaterials* **2015**, *51*, 184–193.
- [125] Chen, Q.; Wang, C.; Zhan, Z.; He, W.; Cheng, Z.; Li, Y.; Liu, Z. Near-Infrared Dye Bound Albumin with Separated Imaging and Therapy Wavelength Channels for Imaging-Guided Photothermal Therapy. *Biomaterials* **2014**, *35* (28), 8206–8214.
- [126] Zheng, M.; Zhao, P.; Luo, Z.; Gong, P.; Zheng, C.; Zhang, P.; Yue, C.; Gao, D.; Ma, Y.; Cai, L. Robust ICG Theranostic Nanoparticles for Folate Targeted Cancer Imaging and Highly Effective Photothermal Therapy. *ACS Appl. Mater. Interfaces* **2014**, *6* (9), 6709–6716.
- [127] Zheng, X.; Xing, D.; Zhou, F.; Wu, B.; Chen, W. R. Indocyanine Green-

Containing Nanostructure as near Infrared Dual-Functional Targeting Probes for Optical Imaging and Photothermal Therapy. *Mol. Pharm.* **2011**, *8* (2), 447–456.

- [128] Liu, P.; Yue, C.; Shi, B.; Gao, G.; Li, M.; Wang, B.; Ma, Y.; Cai, L. Dextran Based Sensitive Theranostic Nanoparticles for near-Infrared Imaging and Photothermal Therapy in Vitro. *Chem. Commun.* **2013**, *49* (55), 6143–6145.
- [129] Mittal, P.; Singh, S.; Singh, A.; Singh, I. K. Current Advances in Drug Delivery Systems for Treatment of Triple Negative Breast Cancer (TNBC). *Chem. Biol. Lett.* **2020**, *7* (1), 1–12.
- [130] Bhattacharyya, J.; Ren, X.-R.; Mook, R. A.; Wang, J.; Spasojevic, I.; Premont, R. T.; Li, X.; Chilkoti, A.; Chen, W. Niclosamide-Conjugated Polypeptide Nanoparticles Inhibit Wnt Signaling and Colon Cancer Growth. *Nanoscale* **2017**, *9* (34), 12709–12717.
- [131] Wu, X.; Wang, L.; Qiu, Y.; Zhang, B.; Hu, Z.; Jin, R. Cooperation of IRAK1/4 Inhibitor and ABT-737 in Nanoparticles for Synergistic Therapy of T Cell Acute Lymphoblastic Leukemia. *Int. J. Nanomedicine* **2017**, *12*, 8025–8034.
- [132] Schmid, D.; Jarvis, G. E.; Fay, F.; Small, D. M.; Greene, M. K.; Majkut, J.; Spence, S.; Mclaughlin, K. M.; Mccloskey, K. D.; Johnston, P. G.; et al. Nanoencapsulation of ABT-737 and Camptothecin Enhances Their Clinical Potential through Synergistic Antitumor Effects and Reduction of Systemic Toxicity. *Cell Death Dis.* **2014**, *5*, 1–11.
- [133] Blanco, E.; Shen, H.; Ferrari, M. Principles of Nanoparticles Design for Overcoming Biological Barriers for Drug Delivery. *Nat. Biotechnol. Biotechnol* **2016**, *33* (9), 941–951.
- [134] Ahmadzada, T.; Reid, G.; McKenzie, D. R. Fundamentals of siRNA and miRNA Therapeutics and a Review of Targeted Nanoparticle Delivery Systems in Breast Cancer. *Biophys. Rev.* **2018**, *10*, 69–86.
- [135] Albanese, A.; Tang, P. S.; Chan, W. C. The Effect of Nanoparticle Size, Shape, and Surface Chemistry on Biological Systems. *Annu. Rev. Biomed. Eng.* **2012**, *14*, 1–16.
- [136] Lazarovits, J.; Chen, Y. Y.; Sykes, E. A.; Chan, W. C. Nanoparticle-Blood Interactions: The Implications on Solid Tumour Targeting. *Chem. Commun.* **2015**, *51*, 2756.
- [137] Hamilton, A.; Biganzoli, L.; Coleman, R.; Mauriac, L.; Hennebert, P.; Awada,

- A.; Nooij, M.; Beex, L.; Piccart, M.; van Hoorebeeck, I.; et al. EORTC 10968: A Phase I Clinical and Pharmacokinetic Study of Polyethylene Glycol Liposomal Doxorubicin (Caelyx, Doxil) at a 6-Week Interval in Patients with Metastatic Breast Cancer. *Ann. Oncol.* **2002**, *13* (6), 910–918.
- [138] Verhoef, J. J.; Anchordoquy, T. J. Questioning the Use of PEGylation for Drug Delivery. *Drug Deliv. Transl. Res.* **2013**, *3* (6), 499–503.
- [139] Hsieh, Y.-C.; Wang, H.-E.; Lin, W.-W.; Roffler, S. R.; Cheng, T.-C.; Su, Y.-C.; Li, J.-J.; Chen, C.-C.; Huang, C.-H.; Chen, B.-M.; et al. Pre-Existing Anti-Polyethylene Glycol Antibody Reduces the Therapeutic Efficacy and Pharmacokinetics of PEGylated Liposomes. *Theranostics* **2018**, *8* (11), 3164–3175.
- [140] Yang, Q.; Lai, S. K. Anti-PEG Immunity: Emergence, Characteristics, and Unaddressed Questions. *Wiley Interdiscip. Rev. Nanomedicine Nanobiotechnology* **2015**, *7*, 655–677.
- [141] Brannon-Peppas, L.; Blanchette, J. O. Nanoparticle and Targeted Systems for Cancer Therapy. *Adv. Drug Deliv. Rev.* **2012**, *64*, 206–212.
- [142] Wang, M.; Thanou, M. Targeting Nanoparticles to Cancer. *Pharmacol. Res.* **2010**, *62* (2), 90–99.
- [143] Wilhelm, S.; Tavares, A. J.; Dai, Q.; Ohta, S.; Audet, J.; Dvorak, H. F.; Chan, W. C. W. Analysis of Nanoparticle Delivery to Tumours. *Nat. Rev. Mater.* **2016**, *1* (May).
- [144] Dai, Q.; Wilhelm, S.; Ding, D.; Syed, A. M.; Sindhvani, S.; Zhang, Y.; Chen, Y. Y.; MacMillan, P.; Chan, W. C. W. Quantifying the Ligand-Coated Nanoparticle Delivery to Cancer Cells in Solid Tumors. *ACS Nano* **2018**, *12*, 8423–8435.
- [145] Rodriguez, P. L.; Harada, T.; Christian, D. A.; Pantano, D. A.; Tsai, R. K.; Discher, D. E. Minimal “Self” Peptides That Inhibit Phagocytic Clearance and Enhance Delivery of Nanoparticles. *Science* (80-. ). **2013**, *339* (6122), 971–975.
- [146] Fang, R. H.; Hu, C. M. J.; Luk, B. T.; Gao, W.; Copp, J. A.; Tai, Y.; O’Connor, D. E.; Zhang, L. Cancer Cell Membrane-Coated Nanoparticles for Anticancer Vaccination and Drug Delivery. *Nano Lett.* **2014**, *14* (4), 2181–2188.
- [147] Gao, W.; Zhang, L. Coating Nanoparticles with Cell Membranes for Targeted Drug Delivery. *J. Drug Target.* **2015**, *23* (7–8).

- [148] Lowery, A. R.; Gobin, A. M.; Day, E. S.; Halas, N. J.; West, J. L. Immunonanoshells for Targeted Photothermal Ablation of Tumor Cells. *Int. J. Nanomedicine* **2006**, *1* (2), 149–154.
- [149] Loo, C.; Lowery, A.; Halas, N.; West, J.; Drezek, R. Immunotargeted Nanoshells for Integrated Cancer Imaging and Therapy. *Nano Lett.* **2005**, *5* (4), 709–711.
- [150] Carbodiimide Crosslinker Chemistry  
<https://www.thermofisher.com/us/en/home/life-science/protein-biology/protein-biology-learning-center/protein-biology-resource-library/pierce-protein-methods/carbodiimide-crosslinker-chemistry.html>.
- [151] Jeong, S.; Park, J. Y.; Cha, M. G.; Chang, H.; Kim, Y.; Kim, H.-M.; Jun, B.-H.; Lee, D. S.; Lee, Y.-S.; Jeong, J. M.; et al. Highly Robust and Optimized Conjugation of Antibodies to Nanoparticles Using Quantitatively Validated Protocols. *Nanoscale* **2017**, *9* (7), 2548–2555.
- [152] Kumar, S.; Aaron, J.; Sokolov, K. Directional Conjugation of Antibodies to Nanoparticles for Synthesis of Multiplexed Optical Contrast Agents with Both Delivery and Targeting Moieties. *Nat. Protoc.* **2008**, *3* (2), 314–320.
- [153] Joshi, P. P.; Yoon, S. J.; Hardin, W. G.; Emelianov, S.; Sokolov, K. V. Conjugation of Antibodies to Gold Nanorods through Fc Portion: Synthesis and Molecular Specific Imaging. *Bioconjug. Chem.* **2013**, *24* (6), 878–888.
- [154] Parolo, C.; Escosura-mun, A. De; Polo, E.; Grazu, V.; Fuente, M. De. Design, Preparation, and Evaluation of a Fixed-Orientation Antibody/Gold-Nanoparticle Conjugate as an Immunosensing Label. *ACS Appl. Mater. Interfaces* **2013**, *5*, 10753–10759.
- [155] Riley, R. S.; Day, E. S. Frizzled7 Antibody-Functionalized Nanoshells Enable Multivalent Binding for Wnt Signaling Inhibition in Triple Negative Breast Cancer Cells. *Small* **2017**, *13*.
- [156] Scott, A. M.; Wolchok, J. D.; Old, L. J. Antibody Therapy of Cancer. *Nat. Rev. Cancer* **2012**, *12* (4), 278–287.
- [157] Jiang, W.; Kim, B. Y. S.; Rutka, J. T.; Chan, W. C. W. Nanoparticle-Mediated Cellular Response Is Size-Dependent. *Nat. Nanotechnol.* **2008**, *3* (3), 145–150.
- [158] Schardt, J. S.; Oubaid, J. M.; Williams, S. C.; Howard, J. L.; Aloimonos, C. M.; Bookstaver, M. L.; Lamichhane, T. N.; Sokic, S.; Liyasova, M. S.; O’Neill, M.; et al. Engineered Multivalency Enhances Affibody-Based HER3 Inhibition and

- Downregulation in Cancer Cells. *Mol. Pharmacol.* **2017**, *14* (4), 1047–1056.
- [159] Fabbri, M.; Paone, A.; Calore, F.; Galli, R.; Croce, C. M. A New Role for microRNAs, as Ligands of Toll-like Receptors. *RNA Biol.* **2013**, *10* (2), 169–174.
- [160] Goyal, R.; Kapadia, C. H.; Melamed, J. R.; Riley, R. S.; Day, E. S. Layer-by-Layer Assembled Gold Nanoshells for the Intracellular Delivery of miR-34a. *Cell. Mol. Bioeng.* **2018**, *11* (5), 383–396.
- [161] Kwok, G. T.; Zhao, J. T.; Weiss, J.; Mugridge, N.; Brahmabhatt, H.; MacDiarmid, J. A.; Robinson, B. G.; Sidhu, S. B. Translational Applications of microRNAs in Cancer, and Therapeutic Implications. *Non-coding RNA Res.* **2017**, *2*, 143–150.
- [162] Shah, M. Y.; Ferrajoli, A.; Sood, A. K.; Lopez-Berestein, G.; Calin, G. A. microRNA Therapeutics in Cancer — An Emerging Concept. *EBioMedicine* **2016**, *12*, 34–42.
- [163] Lennox, K. A.; Behlke, M. A. Chemical Modification and Design of Anti-miRNA Oligonucleotides. *Gene Ther.* **2011**, *18*, 1111–1120.
- [164] Faraoni, I.; Antonetti, F. R.; Cardone, J.; Bonmassar, E. miR-155 Gene: A Typical Multifunctional microRNA. *Biochim. Biophys. Acta* **2009**, 497–505.
- [165] Watts, J. K.; Deleavey, G. F.; Damha, M. J. Chemically Modified siRNA: Tools and Applications. *Drug Discov. Today* **2008**, *13* (19–20), 842–855.
- [166] Layzer, J. M.; McCeffrey, A. P.; Tanner, A. K.; Huang, Z.; Kay, M. A.; Sullenger, B. A. In Vivo Activity of Nuclease-Resistant siRNAs. *RNA* **2004**, *10*, 766–771.
- [167] Petros, R. A.; DeSimone, J. M. Strategies in the Design of Nanoparticles for Therapeutic Applications. *Nat. Rev. Drug Discov.* **2010**, *9* (8), 615–627.
- [168] Knipe, J. M.; Strong, L. E.; Peppas, N. A. Enzyme- and pH-Responsive Microencapsulated Nanogels for Oral Delivery of siRNA to Induce TNF-Alpha Knockdown in the Intestine. *Biomacromolecules* **2016**, *17* (3), 788–797.
- [169] Yin, H.; Kanasty, R. L.; Eltoukhy, A. A.; Vegas, A. J.; Dorkin, J. R.; Anderson, D. G. Non-Viral Vectors for Gene-Based Therapy. *Nat. Rev.* **2014**, *15* (August), 541–555.
- [170] Gao, K.; Huang, L. Nonviral Methods for siRNA Delivery. *Mol. Pharm.* **2009**,

6 (3), 651–658.

- [171] Kanasty, R.; Dorkin, J.; Vegas, A.; Anderson, D. Delivery Materials for siRNA Therapeutics. *Nat. Mater.* **2013**, *12* (11), 967–977.
- [172] Amalvy, J.; Wanless, E.; Michailidou, V.; Armes, S.; Duccini, Y. Synthesis and Characterization of Novel pH-Responsive Microgels Based on Tertiary Amine Methacrylates. *Langmuir* **2004**, *20* (21), 8992–8999.
- [173] Leichty, W.; Scheuerle, R.; Vela Ramirez, J.; Peppas, N. Cytoplasmic Delivery of Functional siRNA Using pH-Responsive Nanoscale Hydrogels. *Int. J. Pharm.* **2019**, *562*, 249–257.
- [174] Forbes, D. C.; Peppas, N. A. Polymeric Nanocarriers for siRNA Delivery to Murine Macrophages. *Macromol. Biosci.* **2014**, *14*, 1096–1105.
- [175] Forbes, D. C.; Peppas, N. A. Polycationic Nanoparticles for siRNA Delivery: Comparing ARGET ATRP and UV-Initiated Formulations. *ACS Nano* **2014**.
- [176] Creixell, M.; Peppas, N. A. Co-Delivery of siRNA and Therapeutic Agents Using Nanocarriers to Overcome Cancer Resistance. *Nanotoday* **2012**, *7* (4), 367–379.
- [177] Riley, R. S.; Dang, M. N.; Billingsley, M. M.; Abraham, B.; Gundlach, L.; Day, E. S. Evaluating the Mechanisms of Light-Triggered siRNA Release from Nanoshells for Temporal Control Over Gene Regulation. *Nano Lett.* **2018**, *18* (6), 3565–3570.
- [178] Kouri, F. M.; Hurley, L. a; Day, E. S.; Hua, Y.; Merkel, T. J.; Queisser, A.; Peng, C.; Ritner, C.; Hao, L.; Daniel, W. L.; et al. miR-182 Integrates Apoptosis , Growth and Differentiation Programs in Glioblastoma. *Genes Dev.* **2015**, *29*, 732–745.
- [179] Jensen, S. A.; Day, E. S.; Ko, C. H.; Hurley, L. A.; Luciano, J. P.; Kouri, F. M.; Merkel, T. J.; Luthi, A. J.; Patel, P. C.; Cutler, J. I.; et al. Spherical Nucleic Acid Nanoparticle Conjugates as an RNAi-Based Therapy for Glioblastoma. *Sci. Transl. Med.* **2013**, *5* (209), 209ra152.
- [180] Melamed, J. R.; Ioele, S. A.; Hannum, A. J.; Ullman, V. M.; Day, E. S. Polyethylenimine-Spherical Nucleic Acid Nanoparticles against Gli1 Reduce the Chemoresistance and Stemness of Glioblastoma Cells. *Mol. Pharmacol.* **2018**, *15* (11), 5135–5145.
- [181] Melamed, J. R.; Kreuzberger, N. L.; Goyal, R.; Day, E. S. Spherical Nucleic

Acid Architecture Can Improve the Efficacy of Polycation-Mediated siRNA Delivery. *Mol. Ther. - Nucleic Acids* **2018**, *12*, 207–219.

- [182] El-Sayed, A.; Harashima, H. Endocytosis of Gene Delivery Vectors: From Clathrin-Dependent to Lipid Raft-Mediated Endocytosis. *Mol. Ther.* **2013**, *21* (6), 1118–1130.
- [183] Dominska, M.; Dykxhoorn, D. M. Breaking down the Barriers: siRNA Delivery and Endosome Escape. *J. Cell Sci.* **2010**, *123*, 1183–1189.
- [184] Lönn, P.; Kacsinta, A. D.; Cui, X. S.; Hamil, A. S.; Kaulich, M.; Gogoi, K.; Dowdy, S. F. Enhancing Endosomal Escape for Intracellular Delivery of Macromolecular Biologic Therapeutics. *Sci. Rep.* **2016**, *6*, 32301.
- [185] Ma, D. Enhancing Endosomal Escape for Nanoparticle Mediated siRNA Delivery. *Nanoscale* **2014**, *6* (12), 6415–6424.
- [186] Cho, Y. W.; Kim, J.-D.; Park, K. Polycation Gene Delivery Systems: Escape from Endosomes to Cytosol. *J. Pharm. Pharmacol.* **2010**, *55* (6), 721–734.
- [187] Benjaminsen, R. V.; Matthebjerg, M. A.; Henriksen, J. R.; Moghimi, S. M.; Andresen, T. L. The Possible “proton Sponge” effect of Polyethylenimine (PEI) Does Not Include Change in Lysosomal pH. *Mol. Ther.* **2013**, *21* (1), 149–157.
- [188] Varkouhi, A.; Scholte, M.; Storm, G.; Haisma, H. Endosomal Escape Pathways for Delivery of Biologicals. *J. Control. Release* **2011**, *151* (3), 220–228.
- [189] Medina-Kauwe, L. K.; Xie, J.; Hamm-Alvarez, S. Intracellular Trafficking of Nonviral Vectors. *Gene Ther.* **2005**, *12*, 1734–1751.
- [190] Rezvantalab, S.; Drude, N. I.; Moraveji, M. K.; Güvener, N.; Koons, E. K.; Shi, Y.; Lammers, T.; Kiessling, F. PLGA-Based Nanoparticles in Cancer Treatment. *Front. Pharmacol.* **2018**, *9*, 1260.
- [191] Riley, R. S.; Melamed, J. R.; Day, E. S. Enzyme-Linked Immunosorbent Assay to Quantify Targeting Molecules on Nanoparticles. In *Targeted Drug Delivery*; 2018; pp 145–157.
- [192] Valcourt, D. M.; Dang, M. N.; Day, E. S. IR820-Loaded PLGA Nanoparticles for Photothermal Therapy of Triple-Negative Breast Cancer. *J. Biomed. Mater. Res. - Part A* **2019**, *107* (8), 1702–1712.
- [193] Turner, N.; Moretti, E.; Siclari, O.; Migliaccio, I.; Santarpia, L.; D’Incalci, M.; Piccolo, S.; Veronesi, A.; Zambelli, A.; Del Sal, G.; et al. Targeting Triple

Negative Breast Cancer: Is p53 the Answer? *Cancer Treat. Rev.* **2013**, *39*, 541–550.

- [194] Su, S.; Ding, Y.; Li, Y.; Wu, Y.; Nie, G. Integration of Photothermal Therapy and Synergistic Chemotherapy by a Porphyrin Self-Assembled Micelle Confers Chemosensitivity in Triple-Negative Breast Cancer. *Biomaterials* **2016**, *80*, 169–178.
- [195] Ayala-Orozco, C.; Urban, C.; Bishnoi, S.; Urban, A.; Charron, H.; Mitchell, T.; Shea, M.; Nanda, S.; Schiff, R.; Halas, N.; et al. Sub-100 Nm Gold Nanomatryoshkas Improve Photo-Thermal Therapy Efficacy in Large and Highly Aggressive Triple Negative Breast Tumors. *J. Control. Release* **2014**, *191*, 90–97.
- [196] Su, S.; Tian, Y.; Li, Y.; Ding, Y.; Ji, T.; Wu, M.; Wu, Y.; Nie, G. “Triple-Punch” Strategy for Triple Negative Breast Cancer Therapy with Minimized Drug Dosage and Improved Antitumor Efficacy. *ACS Nano* **2015**, *9* (2), 1367–1378.
- [197] Yang, Z.; Liu, T.; Xie, Y.; Sun, Z.; Liu, H.; Lin, J.; Liu, C.; Mao, Z.; Nie, S. Chitosan Layered Gold Nanorods as Synergistic Therapeutics for Photothermal Ablation and Gene Silencing in Triple-Negative Breast Cancer. *Acta Biomater.* **2015**, *25*, 194–204.
- [198] Maeda, H. The Enhanced Permeability and Retention (EPR) Effect in Tumor Vasculature: The Key Role of Tumor-Selective Macromolecular Drug Targeting. *Adv. Enzyme Regul.* **2001**, *41* (1), 189–207.
- [199] Hussein, E. A.; Zagho, M. M.; Nasrallah, G. K.; Elzatahry, A. A. Recent Advances in Functional Nanostructures as Cancer Photothermal Therapy. *Int. J. Nanomedicine* **2018**, *13*, 2897–2906.
- [200] Day, E. S.; Thompson, P. A.; Zhang, L.; Lewinski, N. A.; Ahmed, N.; Drezek, R. A.; Blaney, S. M.; West, J. L. Nanoshell-Mediated Photothermal Therapy Improves Survival in a Murine Glioma Model. *J. Neurooncology* **2011**, *104* (1), 55–63.
- [201] Day, E. S.; Zhang, L.; Thompson, P. A.; Zawaski, J. A.; Kaffes, C. C.; Gaber, M. W.; Blaney, S. M.; West, J. L. Vascular-Targeted Photothermal Therapy of an Orthotopic Murine Glioma Model. *Nanomedicine* **2012**.
- [202] Weissleder, R. A Clearer Vision for in Vivo Imaging. *Nat. Biotechnol.* **2001**, *19*, 316.

- [203] Pérez-Hernández, M.; Del Pino, P.; Mitchell, S. G.; Moros, M.; Stepien, G.; Pelaz, B.; Parak, W. J.; Gálvez, E. M.; Pardo, J.; De La Fuente, J. M. Dissecting the Molecular Mechanism of Apoptosis during Photothermal Therapy Using Gold Nanoprisms. *ACS Nano* **2015**, *9* (1), 52–61.
- [204] Sweeney, E.; Cano-Mejia, J.; Fernandes, R. Photothermal Therapy Generates a Thermal Window of Immunogenic Cell Death in Neuroblastoma. *Small* **2018**, *14* (20), e1800678.
- [205] Martin, S. J.; Henry, C. M.; Cullen, S. P. A Perspective on Mammalian Caspases as Positive and Negative Regulators of Inflammation. *Mol. Cell* **2012**, *46*, 387–397.
- [206] Chen, Q.; Xu, L.; Liang, C.; Wang, C.; Peng, R.; Liu, Z. Photothermal Therapy with Immune-Adjuvant Nanoparticles Together with Checkpoint Blockade for Effective Cancer Immunotherapy. *Nat. Commun.* **2016**, *7*.
- [207] Sauter, B.; Albert, M. L.; Francisco, L.; Larsson, M.; Somersan, S.; Bhardwaj, N. Consequences of Cell Death: Exposure to Necrotic Tumor Cells, but Not Primary Tissue Cells or Apoptotic Cells, Induces the Maturation of Immunostimulatory Dendritic Cells. *J. Exp. Med.* **2000**, *191* (3), 423–433.
- [208] Pattani, V. P.; Shah, J.; Atalis, A.; Sharma, A.; Tunnell, J. W. Role of Apoptosis and Necrosis in Cell Death Induced by Nanoparticle-Mediated Photothermal Therapy. *J. Nanoparticle Res.* **2015**, *17*.
- [209] Sweeney, E. E.; Burga, R. A.; Li, C.; Zhu, Y.; Fernandes, R. Photothermal Therapy Improves the Efficacy of a MEK Inhibitor in Neurofibromatosis Type 1-Associated Malignant Peripheral Nerve Sheath Tumors. *Sci. Rep.* **2016**, *6* (November), 1–9.
- [210] Mocan, T.; Matea, C. T.; Cojocaru, I.; Ilie, I.; Tabaran, F. A.; Zaharie, F.; Iancu, C.; Bartos, D.; Mocan, L. Photothermal Treatment of Human Pancreatic Cancer Using PEGylated Multi-Walled Carbon Nanotubes Induces Apoptosis by Triggering Mitochondrial Membrane Depolarization Mechanism. *J. Cancer* **2014**, *5* (8), 679–688.
- [211] Tong, L.; Cheng, J. Gold Nanorod-Mediated Photothermolysis Induces Apoptosis of Macrophages via Damage of Mitochondria. *Nanomedicine* **2009**, *4* (3), 265–276.
- [212] Li, J.-L.; Gu, M. Surface Plasmonic Gold Nanorods for Enhanced Two-Photon Microscopic Imaging and Apoptosis Induction of Cancer Cells. *Biomaterials* **2010**, *31*, 9492–9498.

- [213] Nanospectra Biosciences Inc. Pilot Study of AuroLase(tm) Therapy in Refractory and/or Recurrent Tumors of the Head and Neck.
- [214] Nanospectra Biosciences Inc. Efficacy Study of AuroLase Therapy in Subjects with Primary and/or Metastatic Lung Tumors.
- [215] Peng, C.-L.; Shih, Y.-H.; Lee, P.-C.; Hsieh, T. M.-H.; Luo, T.-Y.; Shieh, M.-J. Multimodal Image-Guided Photothermal Therapy Mediated by <sup>188</sup>Re-Labeled Micelles Containing a Cyanine-Type Photosensitizer. *ACS Nano* **2011**, *5* (7), 5594–5607.
- [216] Lovell, J. F.; Jin, C. S.; Huynh, E.; Jin, H.; Kim, C.; Rubinstein, J. L.; Chan, W. C. W.; Cao, W.; Wang, L. V.; Zheng, G. Porphysome Nanovesicles Generated by Porphyrin Bilayers for Use as Multimodal Biophotonic Contrast Agents. *Nat. Mater.* **2011**, *10* (4), 324–332.
- [217] Kumar, P.; Srivastava, R. IR 820 Dye Encapsulated in Polycaprolactone Glycol Chitosan: Poloxamer Blend Nanoparticles for Photo Immunotherapy for Breast Cancer. *Mater. Sci. Eng. C* **2015**, *57*, 321–327.
- [218] Li, W.; Peng, J.; Tan, L.; Wu, J.; Shi, K.; Qu, Y.; Wei, X.; Qian, Z. Mild Photothermal Therapy/photodynamic Therapy/chemotherapy of Breast Cancer by Lyp-1 Modified Docetaxel/IR820 Co-Loaded Micelles. *Biomaterials* **2016**, *106*, 119–133.
- [219] Zheng, M.; Yue, C.; Gong, P.; Zhao, P.; Zheng, C.; Sheng, Z.; Zhang, P.; Wang, Z.; Cai, L. Single-Step Assembly of DOX/ICG Loaded Lipid-Polymer Nanoparticles for Highly Effective Chemo-Photothermal Combination Therapy. *ACS Nano* **2013**, *7* (3), 2056–2067.
- [220] Srinivasan, S.; Manchanda, R.; Lei, T.; Nagesetti, A.; Fernandez-Fernandez, A.; Mcgoron, A. J. Targeted Nanoparticles for Simultaneous Delivery of Chemotherapeutic and Hyperthermia Agents – An in Vitro Study. *J. Photochem. Photobiol. B Biol.* **2014**, *136*, 81–90.
- [221] Zhao, P.; Zheng, M.; Yue, C.; Luo, Z.; Gong, P.; Gao, G.; Sheng, Z.; Zheng, C.; Cai, L. Improving Drug Accumulation and Photothermal Efficacy in Tumor Depending on Size of ICG Loaded Lipid-Polymer Nanoparticles. *Biomaterials* **2014**, *35* (23), 6037–6046.
- [222] Wu, F. Biological Effects of Thermal Ablation on Tumor. In *Physics of Thermal Therapy: Fundamentals and Clinical Applications*; Moros, E., Ed.; Taylor & Francis Group: Boca Raton, FL, 2012; pp 257–259.

- [223] Chen, H.; Kim, S.; Li, L.; Wang, S.; Park, K.; Cheng, J. X. Release of Hydrophobic Molecules from Polymer Micelles into Cell Membranes Revealed by Förster Resonance Energy Transfer Imaging. *Proc. Natl. Acad. Sci. U. S. A.* **2008**, *105* (18), 6596–6601.
- [224] Qaddoumi, M. G.; Ueda, H.; Yang, J.; Davda, J.; Labhasetwar, V.; Lee, V. H. L. The Characteristics and Mechanisms of Uptake of PLGA Nanoparticles in Rabbit Conjunctival Epithelial Cell Layers. *Pharm. Res.* **2004**, *21* (4), 641–648.
- [225] Cartiera, M. S.; Johnson, K. M.; Rajendran, V.; Caplan, M. J.; Saltzman, W. M. The Uptake and Intracellular Fate of PLGA Nanoparticles in Epithelial Cells. *Biomaterials* **2009**, *30* (14), 2790–2798.
- [226] Holen, I.; Speirs, V.; Morrissey, B.; Blyth, K. In Vivo Models in Breast Cancer Research: Progress, Challenges and Future Directions. *Dis. Model. Mech.* **2017**, *10* (4), 359–371.
- [227] Ghosh, A.; Sarkar, S.; Banerjee, S.; Behbod, F.; Tawfik, O.; McGregor, D.; Graff, S.; Banerjee, S. K. MIND Model for Triple-Negative Breast Cancer in Syngeneic Mice for Quick and Sequential Progression Analysis of Lung Metastasis. *PLoS One* **2018**, *13* (5), 1–23.
- [228] Kaur, P.; Nagaraja, G. M.; Zheng, H.; Gizachew, D.; Galukande, M.; Krishnan, S.; Asea, A. A Mouse Model for Triple-Negative Breast Cancer Tumor-Initiating Cells (TNBC-TICs) Exhibits Similar Aggressive Phenotype to the Human Disease. *BMC Cancer* **2012**, *12* (120).
- [229] Makadia, H. K.; Siegel, S. J. Poly Lactic-Co-Glycolic Acid (PLGA) as Biodegradable Controlled Drug Delivery Carrier. *Polym.* **2011**, *3* (3), 1377–1397.
- [230] Valcourt, D. M.; Dang, M. N.; Scully, M. A.; Day, E. S. Nanoparticle-Mediated Co-Delivery of Notch-1 Antibodies and ABT-737 as a Potent Treatment Strategy for Triple-Negative Breast Cancer. *ACS Nano* **2020**, *14* (3), 3378–3388.
- [231] Ahmad, A.; Banerjee, S.; Wang, Z.; Kong, D.; Sarkar, F. H. Plumbagin-Induced Apoptosis of Human Breast Cancer Cells Is Mediated by Inactivation of NF- $\kappa$ B and Bcl-2. *J. Cell. Biochem.* **2008**, 1461–1471.
- [232] Mungamuri, S. K.; Yang, X.; Thor, A. D.; Somasundaram, K. Survival Signaling by Notch1: Mammalian Target of Rapamycin (mTOR)-Dependent Inhibition of p53. *Cancer Res.* **2006**, *66* (9), 4715–4725.

- [233] Yuan, Z.; Jiang, H.; Zhu, X.; Liu, X.; Li, J. Ginsenoside Rg3 Promotes Cytotoxicity of Paclitaxel through Inhibiting NF- $\kappa$ B Signaling and Regulating Bax/Bcl-2 Expression on Triple-Negative Breast Cancer. *Biomed. Pharmacother.* **2017**, *89*, 227–232.
- [234] Deng, X.; Cao, M.; Zhang, J.; Hu, K.; Yin, Z.; Zhou, Z.; Xiao, X.; Yang, Y.; Sheng, W.; Wu, Y.; et al. Hyaluronic Acid-Chitosan Nanoparticles for Co-Delivery of MiR-34a and Doxorubicin in Therapy against Triple Negative Breast Cancer. *Biomaterials* **2014**, *35*, 4333–4344.
- [235] Adams, J. M.; Cory, S. The Bcl-2 Apoptotic Switch in Cancer Development and Therapy. *Oncogene* **2007**, *26*, 1324–1337.
- [236] Rooswinkel, R.; van de Kooij, B.; Verheij, M.; Borst, J. Bcl-2 Is a Better ABT-737 Target than Bcl-xL or Bcl-W and Only Noxa Overcomes Resistance Mediated by Mcl-1, Bfl-1, or Bcl-B. *Cell Death Dis.* **2012**, *3*, 1–10.
- [237] Billard, C. BH3 Mimetics: Status of the Field and New Developments. *Mol. Cancer Ther.* **2013**, *12* (9), 1691–1701.
- [238] Sakakibara-Konishi, J.; Ikezawa, Y.; Oizumi, S.; Kikuchi, J.; Kikuchi, E.; Mizugaki, H.; Kinoshita, I.; Dosaka-Akita, H.; Nishimura, M. Combined Antitumor Effect of  $\Gamma$ -secretase Inhibitor and ABT-737 in Notch-expressing Non-small Cell Lung Cancer. *Int. J. Clin. Oncol.* **2017**, *22*, 257–268.
- [239] Séveno, C.; Loussouarn, D.; Bréchet, S.; Campone, M.; Juin, P.; Barillé-Nion, S. Gamma-Secretase Inhibition Promotes Cell Death, Noxa Upregulation, and Sensitization to BH3 Mimetic ABT-737 in Human Breast Cancer Cells. *Breast Cancer Res.* **2012**, *14*, 1–15.
- [240] Park, C.; Bruncko, M.; Adickes, J.; Bauch, J.; Ding, H.; Kunzer, A.; Marsh, K. C.; Nimmer, P.; Shoemaker, A. R.; Song, X.; et al. Discovery of an Orally Bioavailable Small Molecule Inhibitor of Prosurvival B-Cell Lymphoma 2 Proteins. *J. Med. Chem.* **2008**, *51*, 6902–6915.
- [241] Gandhi, L.; Camidge, D. R.; Oliveira, M. R. De; Bonomi, P.; Gandara, D.; Khaira, D.; Hann, C. L.; Mckeegan, E. M.; Litvinovich, E.; Hemken, P. M.; et al. Phase I Study of Navitoclax (ABT-263), a Novel Bcl-2 Family Inhibitor, in Patients With Small-Cell Lung Cancer and Other Solid Tumors. *J. Clin. Oncol.* **2011**, *29* (7), 909–916.
- [242] Wilson, W. H.; O'Connor, O. A.; Czuczman, M. S.; LaCasce, A. S.; Gerecitano, J. F.; Leonard, J. P.; Tulpule, A.; Dunleavy, K.; Xiong, H.; Chiu, Y.-L.; et al. Safety, Pharmacokinetics, Pharmacodynamics, and Activity of

Navitoclax, a Targeted High Affinity Inhibitor of BCL-2, in Lymphoid Malignancies. *Lancet Oncol.* **2010**, *11* (12), 1149–1159.

- [243] Rudin, C. M.; Hann, C. L.; Garon, E. B.; Oliveira, M. R. De; Bonomi, P. D.; Camidge, D. R.; Chu, Q.; Giaccone, G.; Khaira, D.; Ramalingam, S. S.; et al. Phase II Study of Single-Agent Navitoclax (ABT-263) and Biomarker Correlates in Patients with Relapsed Small Cell Lung Cancer. *Clin. Cancer Res.* **2012**, *18* (11), 3163–3169.
- [244] Nickoloff, B. J.; Hendrix, A. M. J. C.; Pollock, P. M.; Trent, J. M.; Miele, L.; Qin, J. Notch and NOXA-Related Pathways in Melanoma Cells. *Soc. Investig. Dermatology* **2005**, 95–104.
- [245] Valcourt, D. M.; Harris, J.; Riley, R. S.; Dang, M.; Wang, J.; Day, E. S. Advances in Targeted Nanotherapeutics: From Bioconjugation to Biomimicry. *Nano Res.* **2018**, *3*, 1–18.
- [246] Riley, R. S.; Day, E. S. Frizzled7 Antibody-Functionalized Nanoshells Enable Multivalent Binding for Wnt Signaling Inhibition in Triple Negative Breast Cancer Cells. *Small* **2017**, *13*, 1–10.
- [247] Kocbek, P.; Obermajer, N.; Cegnar, M.; Kos, J.; Kristl, J. Targeting Cancer Cells Using PLGA Nanoparticles Surface Modified with Monoclonal Antibody. *J. Control. Release* **2007**, *120*, 18–26.
- [248] Kumar, S.; Srivastav, R. K.; Wilkes, D. W.; Ross, T.; Kim, S.; Kowalski, J.; Chatla, S.; Zhang, Q.; Nayak, A.; Guha, M.; et al. Estrogen-Dependent DLL1-Mediated Notch Signaling Promotes Luminal Breast Cancer. *Oncogene* **2019**, *38*, 2092–2107.
- [249] Yuan, X.; Zhang, M.; Wu, H.; Xu, H.; Han, N.; Chu, Q.; Yu, S.; Chen, Y.; Wu, K. Expression of Notch1 Correlates with Breast Cancer Progression and Prognosis. *PLoS One* **2015**, *10* (6), 1–13.
- [250] Mollen, E. W. J.; Ient, J.; Tjan-Heijnen, V. C. G.; Boersma, L. J.; Miele, L.; Smidt, M. L.; Vooijs, M. A. G. G. Moving Breast Cancer Therapy up a Notch. *Front. Oncol.* **2018**, *8* (518), 1–25.
- [251] Sethi, N.; Kang, Y. Notch Signalling in Cancer Progression and Bone Metastasis. *Br. J. Cancer* **2011**, *105*, 1805–1810.
- [252] Yip, K. W.; Reed, J. C. Bcl-2 Family Proteins and Cancer. *Oncogene* **2008**, *27*, 6398–6406.

- [253] Mollaei, H.; Safaralizadeh, R.; Rostami, Z. MicroRNA Replacement Therapy in Cancer. *J. Cell. Physiol.* **2019**, *234* (8), 12369–12384.
- [254] Imani, S.; Wu, R.-C.; Fu, J. MicroRNA-34 Family in Breast Cancer: From Research to Therapeutic Potential. *J. Cancer* **2018**, *9*, 3765–3775.
- [255] Goyal, R.; Kapadia, C. H.; Melamed, J. R.; Riley, R. S.; Day, E. S. Layer-by-Layer Assembled Gold Nanoshells for the Intracellular Delivery of miR-34a. *Cell. Mol. Bioeng.* **2018**, *11* (5), 383–396.
- [256] Kapadia, C. H.; Ioele, S. A.; Day, E. S. Layer-by-Layer Assembled PLGA Nanoparticles Carrying miR-34a Cargo Inhibit the Proliferation and Cell Cycle Progression of Triple-Negative Breast Cancer Cells. *J. Biomed. Mater. Res. Part A* **2019**.
- [257] Xia, Y.; Deng, X.; Cao, M.; Liu, S.; Zhang, X.; Xiao, X.; Shen, S.; Hu, Q.; Sheng, W. Nanodiamond-Based Layer-by-Layer Nanohybrids Mediate Targeted Delivery of miR-34a for Triple Negative Breast Cancer Therapy. *RSC Adv.* **2018**, *8* (25), 13789–13797.
- [258] Bu, P.; Chen, K.-Y.; Chen, J. H.; Wang, L.; Walters, J.; Shin, Y. J.; Goerger, J. P.; Sun, J.; Witherspoon, M.; Rakhilin, N.; et al. A microRNA miR-34a Regulated Bimodal Switch Targets Notch in Colon Cancer Stem Cells. *Cell Stem Cell* **2013**, *12* (5), 602–615.
- [259] Tang, Y.; Tang, Y.; Cheng, Y. miR-34a Inhibits Pancreatic Cancer Progression through Snail1-Mediated Epithelial-Mesenchymal Transition and the Notch Signaling Pathway. *Sci. Rep.* **2017**, *7*.
- [260] Zhou, J.; Patel, T. R.; Fu, M.; Bertram, J. P.; Saltzman, W. M. Octa-Functional PLGA Nanoparticles for Targeted and Efficient siRNA Delivery to Tumors. *Biomaterials* **2012**, *33* (2), 583–591.
- [261] Zhang, L.; Liao, Y.; Tang, L. MicroRNA-34 Family: A Potential Tumor Suppressor and Therapeutic Candidate in Cancer. *J. Exp. Clin. Cancer Res.* **2019**, *38* (53).
- [262] Tazawa, H.; Tsuchiya, N.; Izumiya, M.; Nakagama, H. Tumor-Suppressive miR-34a Induces Senescence-like Growth Arrest through Modulation of the E2F Pathway in Human Colon Cancer Cells. *Proc. Natl. Acad. Sci.* **2007**, *104* (39), 15472–15477.
- [263] Slabáková, E.; Culig, Z.; Remšík, J.; Souček, K. Alternative Mechanisms of miR-34a Regulation in Cancer. *Cell Death Dis.* **2017**, *8* (10).

- [264] Venkatesh, V.; Nataraj, R.; Thangaraj, G. S.; Karthikeyan, M.; Gnanasekaran, A.; Kaginelli, S. B.; Kuppana, G.; Kallappa, C. G.; Basalingappa, K. M. Targeting Notch Signalling Pathway of Cancer Stem Cells. *Stem Cell Investig.* **2018**, *5* (5).
- [265] Guo, H.; Lu, Y.; Wang, J.; Liu, X.; Keller, E. T.; Liu, Q.; Zhou, Q.; Zhang, J. Targeting the Notch Signaling Pathway in Cancer Therapeutics. *Thorac. Cancer* **2014**, *5*, 473–486.
- [266] Barua, S.; Yoo, J.-W.; Kolhar, P.; Wakankar, A.; Gokarn, Y. R.; Mitragotri, S. Particle Shape Enhances Specificity of Antibody-Displaying Nanoparticles. *PNAS* **2013**, *110* (9), 3270–3275.
- [267] Jiang, W.; Kim, B. Y. S.; Rutka, J. T.; Chan, W. C. W. Nanoparticle-Mediated Cellular Response Is Size-Dependent. *Nat. Nanotechnol. Lett.* **2008**, *3* (March), 145–150.
- [268] Lee, H.; Odom, T. W. Controlling Ligand Density on Nanoparticles as a Means to Enhance Biological Activity. *Nanomedicine* **2015**, *10* (2), 177–180.
- [269] Elias, D. R.; Poloukhine, A.; Popik, V.; Tsourkas, A. Effect of Ligand Density, Receptor Density, and Nanoparticle Size on Cell Targeting. *Nanomedicine* **2013**, *9* (2), 194–201.
- [270] Kou, L.; Sun, J.; Zhai, Y.; He, Z. The Endocytosis and Intracellular Fate of Nanomedicines: Implication for Rational Design. *Asian J. Pharm. Sci.* **2013**, *8* (103), 1–10.
- [271] Yameen, B.; Choi, W. Il; Vilos, C.; Swami, A.; Shi, J.; Farokhzad, O. C. Insight into Nanoparticle Cellular Uptake and Intracellular Targeting. *J. Control. Release* **2014**, *190*, 485–499.
- [272] Rejman, J.; Bragonzi, A.; Conese, M. Role of Clathrin- and Caveolae-Mediated Endocytosis in Gene Transfer Mediated by Lipo- and Polyplexes. *Mol. Ther.* **2005**, *12* (3), 468–474.
- [273] Pelkmans, L.; Kartenbeck, J.; Helenius, A. Caveolar Endocytosis of Simian Virus 40 Reveals a New Two-Step Vesicular-Transport Pathway to the ER. *Nat. Cell Biol.* **2001**, *3*, 473–484.
- [274] Munsell, E. V; Ross, N. L.; Sullivan, M. O. Journey to the Center of the Cell: Current Nanocarrier Design Strategies Targeting Biopharmaceuticals to the Cytoplasm and Nucleus. *Curr. Pharm. Des.* **2016**, *22* (9), 1227–1244.

- [275] Zeng, Z.; Chen, X.; Zhu, D.; Luo, Z.; Yang, M. Low Expression of Circulating MicroRNA-34c Is Associated with Poor Prognosis in Triple-Negative Breast Cancer. *Yonsei Med. J.* **2017**, *58* (4), 697–702.
- [276] Lodygin, D.; Tarasov, V.; Epanchintsev, A.; Berking, C.; Knyazeva, T.; Körner, H.; Knyazev, P.; Diebold, J.; Hermeking, H. Inactivation of miR-34a by Aberrant CpG Methylation in Multiple Types of Cancer. *Cell Cycle* **2008**, *7* (16), 2591–2600.
- [277] Xiong, S.; George, S.; Yu, H.; Damoiseaux, R.; France, B.; Woei Ng, K.; Say-Chye Loo, J. Size Influences the Cytotoxicity of Poly (Lactic-Co-Glycolic Acid) (PLGA) and Titanium Dioxide (TiO<sub>2</sub>) Nanoparticles. *Arch. Toxicol.* **2013**, *87* (6), 1075–1086.
- [278] Dobrovolskaia, M. A.; McNeil, S. E. Understanding the Correlation between in Vitro and in Vivo Immunotoxicity Tests for Nanomedicines. *J. Control. Release* **2013**, *172*, 456–466.
- [279] He, H.; Liu, L.; Morin, E. E.; Liu, M.; Schwendeman, A. Survey of Clinical Translation of Cancer Nanomedicines—Lessons Learned from Successes and Failures. *Acc. Chem. Res.* **2019**, *52* (9), 2445–2461.
- [280] Huang, X.; Kang, B.; Qian, W.; Mackey, M. A.; Chen, P. C.; Oyelere, A. K.; El-Sayed, I. H.; El-Sayed, M. A. Comparative Study of Photothermalolysis of Cancer Cells with Nuclear-Targeted or Cytoplasm-Targeted Gold Nanospheres: Continuous Wave or Pulsed Lasers. *J. Biomed. Opt.* **2010**, *15* (5), 58002.
- [281] Dobrovolskaia, M. A.; Aggarwal, P.; Hall, J. B.; McNeil, S. E. Preclinical Studies To Understand Nanoparticle Interaction with the Immune System and Its Potential Effects on Nanoparticle Biodistribution. *Mol. Pharm.* **2008**, *5* (4), 487–495.
- [282] Sivakumar, D.; Aashis, R.; Sivaraman, T. In Silico Rationalization for the Differential Bioavailability of ABT-737 and ABT-263 That Antagonise the Anti-Apoptotic Proteins. *J. Pharm. Sci. Res.* **2011**, *3* (4), 1141–1145.
- [283] Maeda, H.; Matsumura, Y. Tumoritropic and Lymphotropic Principles of Macromolecular Drugs. *Crit. Rev. Ther. Drug Carrier Syst.* **1989**, *6* (3), 193–210.
- [284] Iyer, A.; Khaled, G.; Fang, J.; Maeda, H. Exploiting the Enhanced Permeability and Retention Effect for Tumor Targeting. *Drug Discov. Today* **2006**, *11* (17–18), 812–818.

- [285] Sindhwani, S.; Syed, A. M.; Ngai, J.; Kingston, B. R.; Maiorino, L.; Rothschild, J.; MacMillan, P.; Zhang, Y.; Rajesh, N. U.; Hoang, T.; et al. The Entry of Nanoparticles into Solid Tumours. *Nat. Mater.* **2020**.
- [286] Riley, R. S.; Day, E. S. Gold Nanoparticle-Mediated Photothermal Therapy: Applications and Opportunities for Multimodal Cancer Treatment. *Wiley Interdiscip. Rev. Nanomedicine Nanobiotechnology* **2017**, *9* (4).
- [287] Raeesi, V.; Chan, W. C. W. Improving Nanoparticle Diffusion through Tumor Collagen Matrix by Photo-Thermal Gold Nanorods. *Nanoscale* **2016**, *8* (25), 12524–12530.
- [288] Park, J.-H.; von Maltzahn, G.; Xu, M. J.; Fogal, V.; Kotamraju, V. R.; Ruoslahti, E.; Bhatia, S. N.; Sailor, M. J. Cooperative Nanomaterial System to Sensitize, Target, and Treat Tumors. *Proc. Natl. Acad. Sci.* **2010**, *107* (3), 981–986.
- [289] Cang, S.; Iragavarapu, C.; Savooji, J.; Song, Y.; Liu, D. ABT-199 (Venetoclax) and BCL-2 Inhibitors in Clinical Development. *J. Hematol. Oncol.* **2015**, *8* (129).
- [290] Souers, A. J.; Levenson, J. D.; Boghaert, E. R.; Ackler, S. L.; Catron, N. D.; Chen, J.; Dayton, B. D.; Ding, H.; Enschede, S. H.; Fairbrother, W. J.; et al. ABT-199, a Potent and Selective BCL-2 Inhibitor, Achieves Antitumor Activity While Sparing Platelets. *Nat. Med.* **2013**, *19* (2), 202–208.